Minho University
Portugal

Transilvania University
Romania

Characterization of the electrical and optical properties of the CrN_xO_y and AlN_xO_y thin films

Master Thesis

Eng. Roxana ARVINTE

Supervisors:

Prof. Dr. Filipe VAZ
Prof. Dr. Luis MARQUES

2011

Acknowledgements

Every investigation becomes feasible at the expense of the collaboration of various people, and I can only thank the people for their collaboration, intervention or support that made this study possible. As I was saying the realization of this master thesis would not have been possible without some important people to whom I express my gratefulness.

I will like to start with the supervisors of my thesis, Professors Filipe Vaz and Luis Marques for their contribution experience and knowledge, for their suggestions and most of all for the encouragement, attention, availability, and dedication for my work, my doubts, but mostly for me, my very thanks, it was a pleasure to work, learn and share experiences with you!

Also, I will like to say thank you to my colleague Joel Borges for all his help regarding the all areas of knowledge that the work involved, for his advices and of course for his friendship.

I want to thank to all people from the GFCT group at Physics Department from Universidade do Minho for their dedication, support and friendship.

A special acknowledgement to Professor Luis Cunha for his help and encouragement and of course for his friendship.

Thank you very much too all people that during this thesis helped me in different ways.

TABLE OF CONTENT

Chapter I Introduction……………………………………………………………….…………6

1.1. Introductive notion about Surface engineering…………………...……………7

1.1.1 Surface engineering………………….……………………..……..…………7

1.2. Data regarding the types of materials used…...…………………………………9

1.2.1. Thin films based on chromium…………………………………………10

1.2.2. Thin films based on aluminium…………………………………………11

1.3. Conclusion…………………………………………………………….…………13

References……………………………………………………………….…………14

Chapter II Deposition Technique: Reactive magnetron sputtering……………………...16

2.1. Deposition technique: reactive magnetron sputtering………………………..17

2.1.1. Basic concept……………………………………………………………...17

2.1.2. Sputtering regimes………………………………………………...……19

2.1.3. Magnetron sputtering…………………………………………………..…20

2.1.4. Reactive sputtering…………………………..…………………22

2.2. Deposition system…………………………………………………………..…24

2.2.1. Deposition chamber…………………………………………………….25

2.2.2. Vaccum system………………………………………….…………26

2.2.3. Pre-chamber and electric system……………………………………27

2.3. Samples preparation……………………………………………………………28

2.4. Conclusion…………………………………………………………….…………30

References……………………………………………………………….…………31

Chapter III Prepared Samples…………………………………………………………...33

3.1. Introduction…………………………………………….…………….………34

3.2. Characterization techniques……………………………………………………36

3.3. Results and discussion………………………………………………………….41

3.3.1. Chromium oxynitride……………………………………………………...41

Target potential……………………………………………………….41

Deposition rate………………………………………………………43

Morphology of the films…………………………………………46

3.3.2. Aluminium oxynitride………………………………………………47

Target potential……………………………………………………47

Deposition rate……………………………………………………..49

Morphology of the films………………………………………………50

3.4. Conclusions…………………………………………………………….51

References……………………………………………………………………..53

Chapter IV Composition and Structural characterization……………………………55

4.1. Introduction……………………………………………………………….56

4.2. Characterization techniques …………………………………………………..57

4.2.1. Composition analysis: Rutherford Backscattering (RBS)…...…………57

4.2.2. Characterization Techniques - X-ray diffraction (XRD)……….………60

Bragg`s law……………………………………………………………61

Bragg-Brentano geometry………………………………………………63

Glancing Incidence X-ray Diffraction (GIXD)……………………….64

4.3. Results and discussion……………………………………………………..…64

4.3.1 Chromium oxynitride……………………………………………………64

Composition of the films………………………………………………64

Structure analysis of prepared films………………………………..68

4.3.2. Aluminium oxynitride…………………………...………………71

Composition of the films………………………………………………71

Structure analysis of prepared films………………………………..74

4.4. Conclusions………………………………………………………...………76

References……………………………………………………………………...78

Chapter V Electrical Characterization…………………………………………………80

5.1. Introduction……………………………………………………………….81

5.2. Electrical resistivity……………………………………………………………..82

5.2.1. Conductors…………………………………………………………………..84

5.2.2. Insulators……………………………………………………………………85

5.2.3. Semiconductors………………………………………………………………86

5.3. Characterization techniques……………………………………………………87

5.3.1. Four-point probe………………………………………………….……87

5.3.2. Two point technique I-V curves……………………………………..88

5.4. Results and discussion………………………………………………………..90

5.4.1. Electrical behaviour of the chromium oxynitride

and aluminium oxynitride coating……………………….……….……90

5.5. Conclusions…………………………………………………….………….92

References……………………………………………………………………….……………...94

Chapter VI Optical Characterization……………………………………………………...96

6.1. Introduction…………………………………………………………………….………97

6.1.1. Reststrahlen or lattice absorption…………………………………...…99

6.1.2. Free-carrier absorption……………………………………………….100

6.1.3. Band-to-band or fundamental absorption…………………………….101

6.1.4. Impurity absorption…………………………………………………...102

6.2. Characterization techniques……………………………………………………..102

6.2.1. Spectrophotometry and colour space…………………………………102

6.2.2. Interaction between light and matter…………………………………105

6.2.3. Transmission…………………………………………………………..106

6.2.4. Reflection……………………………………………………………...107

6.3. Results and discussion……………………………………………………….....108

6.3.1. Optical behaviour of chromium and aluminium oxynitride coating….108

6.3.2. Reflectance of the coating………………………………......................111

6.3.3. Optical transmittance of the coatings……………………...…………113

6.4. Conclusions…………………………………………………………….……….....115

References………………………………………………………….……………......117

Chapter I
Introduction

1.1. Introductive notion about Surface engineering

1.1.1 Surface engineering

According to David Melford at the Institute of Metal in the UK which has elaborate a first definition of this term "surface engineering essentially consist in the design of the surface and substrate together as a system to provide performance that are unable separately." Surface engineering is not a simple choice of one of the surface treatment technologies, but she refers specifically to the design of the unified system, surface layer based material so that it will best respond to the functional role of a rational use of materials at acceptable costs.

Surface engineering involves a wide range of technologies, some of them well known and successfully applied for many years, such as diffusion surface treatments with or without reaction, hardening by rolling, so although some advanced technology, have expanded only their commercial purpose in recent years (hard adherent layer deposition stimulated or activated in plasma, ion implantation, laser treatment, sputtered deposition) [1].

Focusing the scientific effort to develop this new area of multidisciplinary research was determined by the fact that removal of a mechanical part from use is caused by three phenomens, i.e. wear, corrosion and fatigue, which occurs mainly in the area, where the demands are more intense and complexes [2]. Progressive deterioration of metal parts and tool surfaces used in industry leads to gradual decrease in the use of their properties or even their premature removal from service. Destruction of the materials due to wear and corrosion both direct and indirect, with a economic cost of hundreds of billions of dollars each year for different countries [3].

In Fig.1.1. is shown schematically the superficial layer – substrate system. The connection between the two elements is achieved by an interface whose thickness and structure depends on the nature of materials and the technology necessary for obtaining the superficial layer [4].

The system presents four distinct areas:

- *contact surface* with the conjugated piece or environment where the roughness, friction coefficient and chemical stability are the most important;
- *interface* between superficial layer and substrate, where adhesion and chemical interaction between coating and substrate are crucial properties;

— *superficial layer* which is particularly interested in depth, composition and the microstructure determinate for their properties such as hardness, tensile strength, corrosion, internal stress, Young modulus and tenacity;

— *substrate*, whose basic properties are tensile strength, toughness, hardness and Young modulus [5];

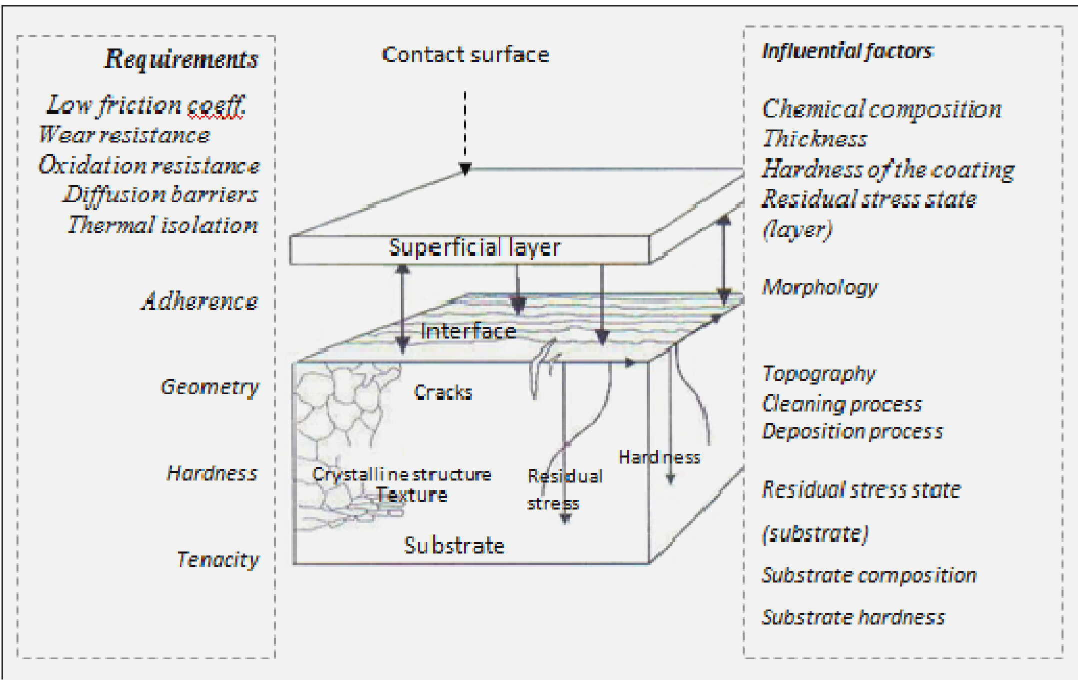

Fig.1.1. *The superficial layer-substrate system*

Deposition particles by their energy and nature have a great influence on the structure, composition and compactness of the deposition. Depending on the intended functional destination of the film, during the deposition process are controlling the: deposition time thickness, electrical resistance, or another parameter. The physical deposition is a technological process of creating thin films, consisting of powder material coating and heat treatment by sintering and homogenization of the layer.

PVD coating process has its beginning from 1857, when Faraday was able to deposit on a glassy surface metal vapors produced by pulverization of a metallic specimen, which was in an inert environment. Approximately 100 years the process has been applied only for decoration, using condensation of pure metals (ex. coatings on watch dials). The method does not ensure growth durability or hardness of the surface layer of tools used.

PVD techniques are physical deposition techniques. The nanostructure layers, through these deposition technologies enable conversion applications of thermal energy into electrical energy. Deposition process includes dry and wet deposition. Chemical vapor deposition and physical vapor deposition are dry depositions. In the deposition process, the deposited atoms are bounded only by molecular bonds due to the van der Waals forces. The PVD is a deposition process of a thin layer in a gas phase, where the source material is transformed by physical means in vacuum, from a substrate without any chemical reaction involved [1].

During PVD deposition, the material which fallows to be deposited is vaporized or sprayed, and is mixed with a gas and then condenses from the vapor form into a thin film on the material. Layers are obtained by condensation, on the surface substrate of atomic or molecular species in vapor.

PVD processes can be divided according to the methods of formation of the primary vapors: thermal evaporation processes and kinetic pulverization processes. Deposition material or at least its basic component is initially in solid or liquid state. Atomic vapor source transition is made by physical mechanisms, meaning pulverization, particle bombardment or by evaporation. For the deposition to produce on the substrate with little loss of material is necessary that between the walls and the substrate to exist temperature differences, i.e. the substrate to be colder and the walls to be at the system temperature. PVD technique is used with good results for metal layers with controlled morphology [6].

1.2. Data regarding the types of materials used

Recently,a new class of materials has become very important for several technological fields, but poorly explored, the oxynitrides: MeNxOy (with Me=metal). The importance of this class of materials is based on the fact that oxygen is much more reactive than nitrogen and, due to this higher reactivity, the addition of a small amount of oxygen to a growing transition metal nitride film induces the production of ionic metal–oxygen bonds in a matrix of roughly covalent metal–nitrogen bond. This fact creates a new structure with a large gradient indifferent properties, where the optical, electrical and mechanical ones may be tailored according to the particular application envisaged. The control of the oxide/nitride ratio allows tuning of the band gap,band width, and crystallographic order between oxide and nitride and, in consequence, the electronic properties of materials and thus, the overall films responses [7].

1.2.1. Thin films based on chromium

Chromium based coatings have been investigated for over a decade and were successfully implemented in many areas such as wood machining, bearing work other engineering components. These coatings exhibit excellent properties like high hardness, oxidation resistance, chemical stability, etc. [7-8]. Chromium nitride (CrN) and chromium oxide (Cr_2O_3) are very good candidates for protection of steels, decorative applications due to their distinct colours and for their mechanical properties [9-10]. In fact, and due to the CrN excellent mechanical properties, oxidation resistance, chemical stability and slide, it has been used as a material for cutting tools, plastic metal molds, and frictional parts [11]. It also finds applications in automotive industry as coatings for lubricated tribological systems. They are also used in molds and pins for aluminium die casting, where mechanical resistance and high temperature oxidation resistance is required [12]. Chromium nitride (CrN) films have drawn wide attention in electronics industry because of their high hardness (1090 Hv) and lower electrical resistivity (640 μΩ cm) [14].

Among the various chromium oxides, Cr_2O_3 is the most stable under ambient conditions, and it is characterized by its chemical inertness, stability, mechanical strength and relatively high hardness Previous research shows that the hardness of chromium oxide coatings strongly depends on the stoichiometric polycrystalline Cr_2O_3 phase present in the coating [12], with high quality Cr_2O_3 stoichiometric coatings reaching nearly 30 GPa hardness combined with good scratch resistance. In terms of optical-based applications Cr_2O_3 thin films include electrochromic coatings, infrared (IR)-transmitting coatings, selective black absorbers, and optically selective surfaces of solar collectors [13].

As chromium oxide is an insulating antiferromagnetic material it is also suitable as a tunnel junction barrier. Depending on its stoichiometry CrN_x shows a metallic-like ($\rho_{CrN} \approx 6.4\times10^{-4}$ Ω cm, x ≈ 0.93) or semiconducting behavior ($\rho_{CrN} > 1\times10^{-2}$ Ω cm, x ≈ 1.06) while chromium oxide is a wide-band gap semiconductor ($E_g \approx 4$ eV, $\rho_{Cr2O3} >> 1$ Ω cm). Combining both materials as chromium oxynitride opens the possibility to tune the energy band gap and hence the electronic properties in a wide range [14].

Fig. 1.2. *Application of the thin films based on chromium*

In comparison with Cr_2O_3, the chromium oxynitride has a higher corrosion resistance and the layer has a better adhesion and a uniform structure [3].
Chromium oxynitride crystallize in the rock salt structure (fcc) and are antiferromagnetic with a Néel point of about 273K [9]. The density of bulk CrN (6.2 gcm^{-3}) is higher by 12% compared to Cr_2O_3 (5.2gcm^{-3}). This is plausible, since chromium oxide crystallizes only at substrate temperatures of ≥ 300 ºC [4].

1.2.2. Thin films based on aluminium

Among the group of possible oxynitrides, aluminium oxynitrid thin films (AlN_xO_y) may have some interesting applications in different technological fields, due to a wide difference in the two base materials: aluminium nitride (AlN) and aluminium oxide (Al_2O_3). However, the available knowledge on this particular system is still much reduced and its application is still very limited.

Anyway, and similarly to the other already studied oxynitride systems, the wide variation between the properties of Al_2O_3 and those of AlN opens a significant number of possible applications for the Al–N–O system, which, in a first approach, would allow to tailor the properties of the oxynitride films between those of the pure oxide and nitride films, or to combine some of their advantages by varying the concentration of aluminium, oxygen and nitrogen in the film, according to the particular application envisaged.

Aluminium nitride (AlN) is known as being a semiconductor with a large band gap (6.2eV) [1] in its more stable and common hexagonal (wurtzite) crystalline structure [2]. Beyond this structure, AlN has also two kinds of cubic structures (with two different lattice

parameters) [2] and it was considered, a couple of decades ago [3],as one of the best existing thermal conductors, being an important ceramic material used in many applications such as substrate in microelectronic devices. The hexagonal AlN also exhibits a high chemical stability, high hardness (25 GPa) [4] and high electrical resistivity (1020 cm) [5]. The thermal conductivity and electrical resistivity are even higher for the cubic AlN [2]. Polycrystalline aluminium nitride has also high dielectric strength (between 400 and 550 Vm^{-1}), which can be improved if one produces amorphous AlN [1]; a moderated dielectric constant (8.8 at 1 MHz) [5];and it is an excellent piezoelectric material [6].

AlN also resists to high temperatures (melting point above 2670 K) and caustic chemical etching [7]. All these physical/chemical properties allowed the use of this material in the fabrication of optical sensors (in the UV–visible region), high power and high temperature electronic devices, surface acoustic wave (SAW) devices [8], electronic packages, among several other examples.

On the other hand, aluminium oxide, or simply alumina (Al_2O_3), is an insulator material which is commonly prepared in the form of polymorphous material, since it can exist in many metastable structures that are divided into two broad categories: a face-centered-cubic (fcc) or a hexagonal close packed (hcp) arrangement of oxygen anions. The arrangement of aluminium cations can produce different structures, those that are based in fcc packing of oxygen and those based on hcp packing of oxygen. The first case includes γ- Al_2O_3 and η- Al_2O_3 (cubic arrangement), θ- Al_2O_3 (monoclinic), and δ- Al_2O_3 (either tetragonal or orthorhombic); while in these second case we have α- Al_2O_3 (trigonal), k- Al_2O_3 (orthorhombic), and x- Al_2O_3 (hexagonal) phases [9]. The dominant and stable phase of alumina, α- Al_2O_3, possesse strig on asymmetry with rhombohedral Bravais lattice. It exhibits chemical and mechanical stability at a temperature of up to 1250 K and melts at 2326 K [10] and it is considered as the best anti-oxidization coating at high temperatures, being an important coating used in the metal working industry [11]. An important fact about α- Al_2O_3 (or corundum phase of alumina) is that it only can be produced at temperatures above 1023 K, using Physical Vapour Deposition (PVD) techniques [11].

The particular dielectric properties of alumina allow to use it in a large variety of applications, which can vary from microelectronics and optical applications to wear resistant coatings [12], as protective films for metal reflectors, for dark mirrors, and in metal–oxide semiconductor devices [13]. Regarding the “mixed” aluminium oxynitride films, its use is not yet very common, despite some very few examples that are known in the field of protective

coatings against wear, diffusion and corrosion, optical coatings, optoelectronics, microelectronics [14], multilayer capacitors as dielectric [1], among others.

Fig. 1.3. *Application of the thin films based on aluminum*

Taking into account that the properties of the materials significantly depend on their interdependence of composition, structure and morphology, an understanding of these relationships will be a major concern in this work. For this purpose a set of Cr-N-O and Al–N–O films was prepared and analyzed in terms of all the above items. The study will allow the establishment of limits for practical applicability of devices coated with these materials, providing new areas of application and supplying criteria for new materials design for specific applications.

1.3. Conclusion

The this first chapter presents information regarding Surfaces engineering and the PVD deposition methods of thin layers, and data about the coatings used based on chromium and aluminum in particular the oxynitride type.

During PVD deposition, the material that has to be deposited is vaporized or sprayed, is mixed with a gas and then it condenses under a vapor form of a thin film on the substrate. The coatings are obtained by condensation on the surface of the substrate of an atomic or molecular species, under vapor phase.

Thin films as the chromium oxynitride have interesting properties like, high hardness and a beautiful decorative colour green, therefore, have industrial applications as hard and decorative coatings. Regarding the mixed coatings, as aluminum oxynitride type, its use is not yet very common, despite some very few examples that are known in the field of protective

coatings against wear, diffusion and corrosion, optical coatings, optoelectronics, microelectronics [14], multilayer capacitors as dielectric [1], among others.

References

[1]. G. Mares, Ingineria suprafeţelor metalice: Prelucrări termomecanice, termochimice, chimice, electrochimice şi fizice ale stratului superficial, Ed. Universităţii Transilvania, Braşov (2004);

[2]. Cristian Ionescu, Alexandru Munteanu, Daniel Munteanu, Straturi dure de tip Ti-Si-C, obişnuite la temperaturi joase prin depunere fizică din vapori, Ed. Universităţii Transilvania Braşov, (2009);

[3]. I. Vedinaş, E. Creţu, Elemente de nanotehnologie, Editura Universităţii Titu Maiorescu, Bucureşti, (2007);

[4]. G. Mares, Tehnologii de suprafaţare:bazele ingineriei suprafeţelor materialelor, Ed. Universităţii Transilvania, Braşov, (2002);

[5]. G. Mares, V. Ditu, Tehnologii de suprafaţare:bazele ingineriei suprafeţelor materialelor, Ed. Universităţii Transilvania, Braşov, (1999);

[6]. Cahn, R.W. – The coming of materials science, Pergamon, Amsterdam, (2001);

[7]. B. Gakovic, M. Trtica, P. Panjan, M. Cekada: Appl. Phys. A79, 1353–1355 (2004);

[8]. Yongjing Shi, Siyuan Long, Liang Fang, Shicai Yang, Fusheng Pan: Applied Surface Science 254, 5861–5867, (2008);

[9]. Said Agouram, Franz Bodart, Guy Terwagne: Surface and Coatings Technology 180–181, 164–168, (2004);

[11]. Tsuneo Suzuki, Hajime Saito, Makoto Hirai, Hisayuki Suematsu, Weihua Jiang, Kiyoshi Yatsui: Thin Solid Films 407, 118–121, (2002);

[12]. V. Ezirmik, E. Senel, K. Kazmanli, A. Erdemir, M. Ürgen: Surface & Coatings Technology 202, 866–870, (2007);

[13]. M.F. Al-Kuhaili, S.M.A. Durrani: Optical Materials 29, 709–713, (2007);

[14]. R. Mientus, R. Grötschel, K. Ellmer: Surface & Coatings Technology 200, 341–345, (2005);

[15]. Christoph Mitterbauer, Werner Grogger, Peter Wilhartitz, Ferdinand Hofer: Micron 37, 385–388, (2006);

[16]. Tsuneo Suzuki, Jun Inoue, Hajime Saito, Makoto Hirai, Hisayuki Suematsu, Weihua Jiang, Kiyoshi Yatsui: Thin Solid Films 515, 2161–2166, (2006);

[11]. Hong-Ying Chen, Fu-Hsing Lu : Thin Solid Films 515, 2179–2184, (2006);

[18]. St. Collard, H. Kupfer, G. Hecht, W. Hoyer, H. Moussaoui: Surface and Coatings Technology 112, 181–184, (1999);

[19]. K.R. Bray, R.L.C. Wu, S. Fries-Carr, J. Weimer, Thin Solid Films 518, 366–371, (2009);

[20]. J. Wang, W.L. Wang, P.D. Ding, Y.X. Yang, L. Fang, J. Esteve, M.C. Polo, G. Sanchez, Diamondand Related Materials 8, 1342–1344, (1999);

[21]. X. Qing, X. Hui, L.R. Arthur, Journal of Applied Physics 73, 8198–8200, (1993);

[22]. L. Yate, J.C. Caicedo, A.H. Macias, F.J. Espinoza-Beltrán, G.Zambrano, J.Munoz-Saldana, P.Prieto, Surface and Coatings Technology 203, 1904–1907, (2009);

[23]. H.C. Barshilia, B. Deepthi, K.S. Rajam, Thin Solid Films 516, 4168–4174, (2008);

[24]. V. Mortet, M. Nesladek, K. Haenen, A. Morel, M. D’Olieslaeger, M. Vanecek, Diamondand Related Materials 13, 1120–1124, (2004);

[25]. N. Rakov, A. Mahmood, M. Xiao, Scripta Materialia 50, 589–592, (2004);

[26]. Q.X. Guo, M. Yoshitugu, T. Tanaka, M. Nishio, H. Ogawa, Thin Solid Films 483, 16–20, (2005);

[27].L. Igor, B. David, Journal of the American Ceramic Society 81 (1998) 1995–2012.

[28]. J.M. Schneider, W.D. Sproul, A. Matthews, Surface and Coatings Technology 98, 1473–1476, (1998);

[29]. A. Aryasomayajula, S. Canovic, D. Bhat, M.H. Gordon, M. Halvarsson, Thin Solid Films 516, 397–401, (2007);

[30]. H. Kakati, A.R. Pal, H. Bailung, J. Chutia, Applied Surface Science 255, 7403–7407, (2009);

[31]. B.G. Segda, M. Jacquet, J.P. Besse, Vacuum 62, 27–38, (2001);

[32]. S. Dreer, R. Krismer, P. Wilhartitz, G. Friedbacher, Thin Solid Films 354, 43–49, (1999).

Chapter II

Deposition Technique:

Reactive magnetron sputtering

2.1. Deposition technique: reactive magnetron sputtering

2.1.1. Basic concept

The term sputtering comes from the Dutch "sputteren" meaning "to spit out in small particles and with a characteristic explosive sound". Sputtering was first observed by Groves in 1852 but was Plücker first to suggest, in 1858, that this discovery can be used as a tool to produce metallic films. Today, sputtering is a powerful tool used for the deposition of thin films, in chemical analysis, etching and cleaning. Sputtering is commonly utilized for thin film deposition, as the extreme conditions for melting or chemically reacting high melting point materials are not required, as with evaporation or an electrochemical process [1].

In the basic sputtering process, a target plate is bombarded by energetic ions, generated by a glow discharge plasma, located in front of the target. The bombardment process causes the removal of atoms of the target, which will condense on a substrate (part to be coated) as a thin film [2]. Secondary electrons are also emitted from the target surface as a result of the ion bombardment. These electrons play an important role in maintaining the plasma.

Sputtering is a physical vapour deposition process (PVD) and is driven by momentum transfer between the ions and atoms in the material (Fig. 2.1). Collisions are elastic or inelastic, depending on whether the internal energy of the colliding specie is preserved. In an elastic collision, only kinetic energy is interchanged and there is conservation of the momentum and kinetic energy of translational motion, and no atomic excitation occurs and potential energy is conserved [3].

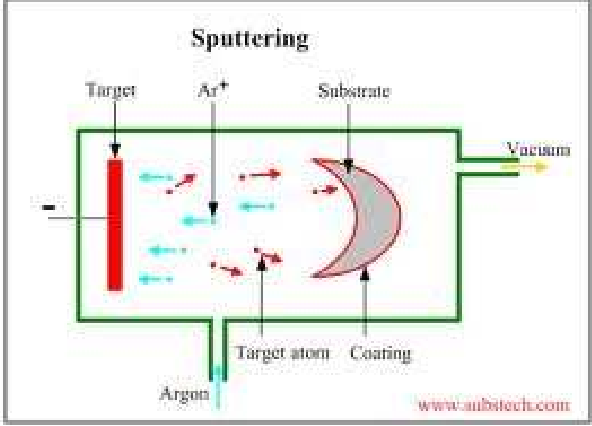

Fig. 2.1. *Scheme of the sputtering process*

As a result of both momentum and kinetic energy conservation laws, the ratio of the kinetic energies between the two species that collide is:

$$\frac{E_1}{E_2} = \frac{4M_1M_2}{(M_1+M_2)} cos^2 \quad \text{(eq.2.1)}$$

where (M_1, E_1) and (M_2, E_2) refer to the mass and energy of the impinging particles and the sputtered target atoms, respectively. The angle is defined by the initial trajectory of impinging particle and the line joining their centres at contact. Nevertheless, the first collision pushes atoms deeper into the material, the subsequent collisions between the atoms result in some of the atoms near the surface being ejected away from the surface of the target (Fig. 2.1).

The first and most well-known scientific work on the quantification of the sputtering process was carried out by P. Sigmund [3]. He proposed that the momentum transfer processes occurring at the surface are caused by a collision cascade, within the surface layers, Fig.2.1. The amount of ejected atoms from the surface per incident particle is called the sputter yield, which is an important measure of the efficiency of the sputtering process. The sputter yield depends not only on the energy and masses of the incident ions, but also on the atoms of the target and their surface binding energy and/or on the possible compounds formed at the target surface [4-7].

The sputtering process is quantified in terms of the sputtering yield, defined as the number of target atoms ejected per incident particle. The yield depends on the target species and the nature, energy, and angle of incidence of the bombarding species.

During sputtering process there are two main processes that occur: plasma generation and ion bombardment. There are several ways to supply the necessary energy for plasma generation from a neutral gas. In magnetron sputtering the plasma is achieved by applying an electric field to a neutral gas (Fig. 2.2) [8]. A variety of power supplies are used for plasma generation, ranging from direct current (DC) to alternate current (AC), with frequencies into the mega-hertz range – radiofrequency (RF) – being the most common ones. In dc sputtering, a potential difference of several hundred volts is generated between the substrate holder and the magnetron, creating an intense electric field between them (Fig. 2.2) [9]. The electrons in neutral gas are accelerated by the intense electric field applied between the electrodes, generating new electrons and ions (electron-impact ionization) and thus mantaining the plasma.

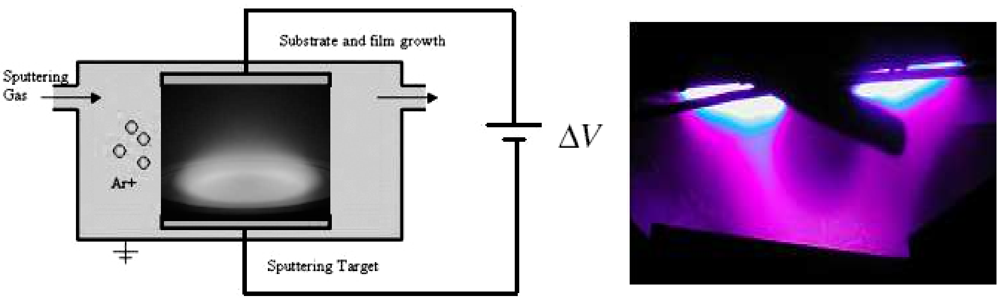

Fig. 2.2. *Scheme of the system used to obtain the plasma*

2.1.2. Sputtering regimes

The fundamental understanding of sputtering emerges from investigations that study the interactions between bombarding charged particles and atoms in a solid [5]. In 1908, Stark was the first to propose the momentum transfer theory, which states that target atoms are ejected when momentum is transferred from bombarding ions to target atoms. The momentum transfer processes occurring at the surface are caused by a collision cascade within the surface layers, which was first proposed by Sigmund.

At low kinetic energies (below 50 eV), the ions don't have sufficient energy to dislocate the target atoms and thus the ejection of target particles occurs only for very special collision geometries. The momentum transferred from the ion impact will drive only the surface target atoms further into the target. For moderate energies (between 50 and roughly 1 keV), the ion impact dislocate ("knock-on") atoms into the target, which by their turn will dislocate other target atoms. This induces a collision cascade that eject atoms, ions, electrons and neutrals from the first 10 to 50Å of the surface of a target. Several studies show that, to induce sputtering, the ion energies must exceed four times the binding energy of the atoms at the target surface [10,11]. It is in this range of energies that most common PVD systems operate and can be illustrated schematically in fig. 2.3.

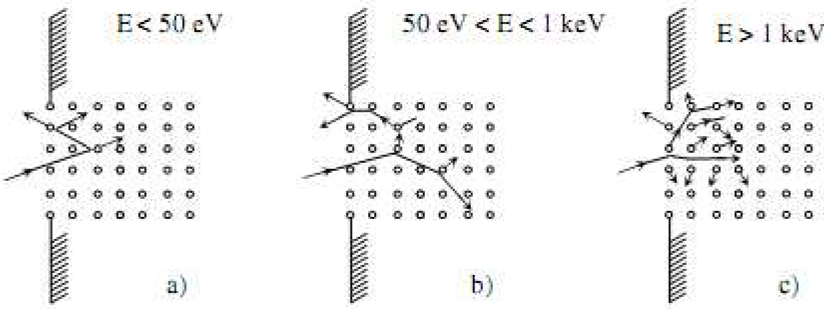

Fig. 2.3. *Scheme of the three sputtering regimes:* ***a)*** *single-knock-on;* ***b)*** *linear cascade;* ***c)*** *spike*

2.1.3. Magnetron sputtering

Magnetron sputtering has developed rapidly over the last decade to the point where it has become established as the process of choice for the deposition of a wide range of industrial important coatings. The driving force behind this development has been the increasing demand for high-quality functional films in many diverse market sectors.

The basic sputtering process has been known and, despite its limitations, used for many years. It consists in the bombardment of a target (or cathode) plate by energetic ions generated in a glow discharge plasma, situated in front of the target. The bombardment process causes the removal, i.e., ``sputtering``, of target atoms, which may then condense on a substrate as a thin film [13]. Secondary electrons are also emitted from the target surface as a result of the ion bombardment, and these electrons play an important role in maintaining the plasma. However, basic sputtering is limited by low deposition rates, low ionisation efficiencies in the plasma, and causes high substrate heating.

The introduction of what is now termed ``conventional``, or ``balanced`` magnetron, in the early 1970s was an important step forward in overcoming these limitations. However, it was the development of the unbalanced magnetron in the late 1980s and its incorporation into multi-source ``closed-field`` systems in the early 1990s, that transformed the capabilities of this technique, and has subsequently been responsible for the raise of its importance [12]. Magnetron is, in basic terms, a system composed by magnets with a specific orientation, positioned behind the target. The magnets are positioned in order that one pole is situated at the central axis of the target and the second pole is formed by a ring of magnets around the outer edge of the target. The introduction of a magnetic field parallel to the target surface

constrains the electron motion to the vicinity of the target, forcing them to describe helicoidally trajectories around magnetic field flux lines near the target surface (Fig.2.4). The electrons are thus confined (“trapped”) in front of the target, but ions are allowed to travel across the sheath and gain acceleration towards the target [14]. This confinement, results in an increased ionization efficiency within the regions close to the target, and thus in a higher plasma density. This, in turn, leads to an increase in ion bombardment of the target, originating higher sputtering rates and, therefore, higher deposition rates at the substrate [15].

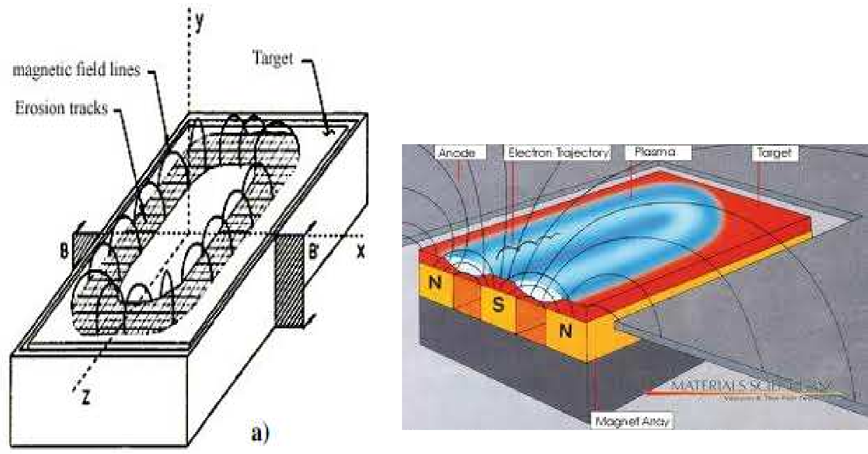

Fig. 2.4. *Scheme of a magnetron and the correspondent magnetic field lines*

The increased ionization efficiency achieved in the magnetron, allows the discharge to be maintained at lower operating pressures (typically, 10^{-3} mbar, compared to10^{-2} mbar) and lower operating voltages (typically, -500V, compared to -2 to -3 kV), than it is possible in the basic sputtering [15]. In spite of these advantages, the plasma confinement close to the target induces localized sputtering phenomena, reducing the sputtered area of the target to less than 30 % of the target material- the erosion zone [16]. To overcome this limitation of conventional magnetrons, new magnetrons have been designed with different degrees of magnetic field unbalancing [17]. There are two types of planar magnetrons, unbalanced and balanced, with slight differences in design, which are illustrated in fig 5. In a conventional balanced magnetron, the plasma is strongly confined to the target region, typically extending to few tens of millimeters (typically between 60 and 100 mm) from the target surface. In a type-1 unbalanced magnetron the outer ring of magnets is strengthened relative to the central pole. In this case, not all the field lines are closed between the central and outer poles in the magnetron, but some are directed towards the substrate, and some secondary electrons are

able to follow these field lines. Consequently, the plasma is no longer strongly confined to the target region, but is also allowed to flow out towards the substrate [18]. In this case the field lines which do not close on themselves are directed towards the chamber walls and the plasma density in the substrate region is low. (Fig. 2.5). In an unbalanced-type magnetron (type 2), not all the magnetic field lines are closed between the central and outer poles in the magnetron, but some are focused in the direction of the substrate, [12], resulting that some secondary electrons are able to follow these field lines. This generates plasmas that are no longer strongly confined to the target region, but are also allowed to run out in the direction of the substrate, originating higher ionic currents from the plasma without the requirement of externally biasing the substrate. Thus, in addition to providing a high flux of adatoms, an unbalanced magnetron also acts as a very effective ion source.

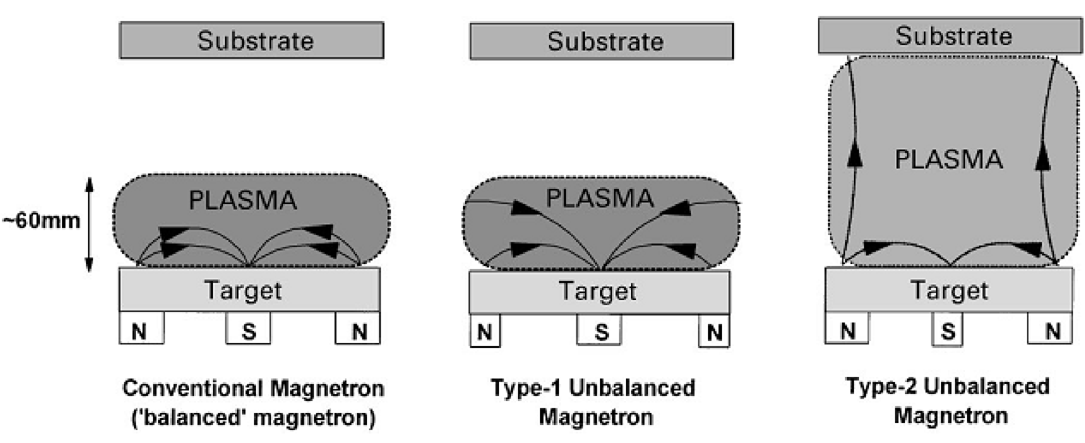

Fig.2.5. *Schematic representation of the plasma confinement observed in conventional and unbalanced magnetrons*

2.1.4. Reactive sputtering

Reactive sputtering can be defined as the sputtering of elemental targets in the presence of chemically reactive gases that react with both the ejected target material and the target surface. It has become a very popular technique in today's search for new materials, for the deposition of a wide range of compound and alloy thin films including oxides, nitrides, carbides, fluorides or arsenides [20].

Although reactive sputtering is conceptually simple, it is in fact a complex and nonlinear process which involves many interdependent parameters. The presence of the reactive gas at both the cathode surface and the substrate results in strong interactions of their

active gas not only with the condensing material but also with the cathode surface, resulting in the so-called target poisoning. If flow control of reactive gas is used, such reactions are marked by a change in the impedance of the operating plasma, an abrupt increase in the system pressure or more precisely, in the reactive gas pressure, a drastic drop in the deposition rate and a change in the film composition from metal-rich to gas-rich [20].

The simplest experiment to study the reactive sputtering process is the so called hysteresis experiment: the discharge is ignited in pure argon, at a given pressure by introducing a certain argon flow to vacuum chamber. The ratio between the argon flow and the argon pressure defines the argon pumping speed. Keeping the discharge current constant, the oxygen flow is stepwise increased. When the target is completely poisoned the measuring procedure is reversed, i.e. the oxygen flow is stepwise decreased until the discharge is again in pure argon.

This value of reactive gas flow is defined as the critical flow where transition between metallic and compound mode occur at the target. For reactive gas flows lower than the critical value, the target works in a “metallic mode”, while for reactive gas flows higher than that critical value, it works in the “poisoned mode”. The transition from the “metallic mode” to “poisoned mode“, most of the times, exhibits a hysteresis that can be reduced by increasing the pumping speed (Fig.2.6).

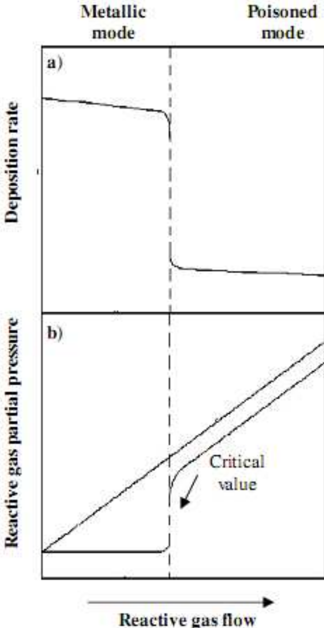

Fig.2.6. *Typical behaviour of the deposition rate, and partial pressure of the reactive gas versus the reactive gas flow rate, during a reactive magnetron sputtering*

Figure 2.6 shows the behaviour of the partial pressure of the reactive gas, as function of the reactive gas flow rate, when the plasma is on and off. When the plasma is off, the partial pressure varies linearly with the reactive gas flow rate injected into the deposition chamber, while when the plasma is on, the partial pressure of the reactive gas remains almost constant until the reactive gas flow reaches the critical value.

This constancy of the partial pressure of the reactive gas is due to the trapping of the reactive gas, by compounds formation on the target surface, as well as by the metal deposited on the walls and the substrate (getter effect). When the reactive gas flow is higher than the critical value, the target becomes poisoned and the consumption of reactive gas drops, inducing linear behaviour of the partial pressure of the reactive gas with the reactive gas flow injection [24].

In a general way, the behaviour of the target voltage during reactive magnetron sputtering can be mostly attributed to the formation of a compound layer on the target surface, which has a different ion-induced secondary electron emission (ISEE) coefficient than the target material. In terms of target voltage, it is widely known and accepted that the minimum voltage required to sustain the magnetron discharge is given by:

$$V_{min} = \frac{W_0}{\gamma_{ISEE}\, E_{\varepsilon_i \varepsilon_e}} \qquad \text{(eq.2.2)}$$

with W_0 representing the effective ionization energy; γ_{ISEE} the ion induced secondary electron emission coefficient; and E the effective gas ionization probability. The other two parameters, ε_i and ε_e, are close to unit for magnetron sputtering, which means that the cathode voltage essentially depends on the γ_{ISEE} coefficient [22-23].

2.2. Deposition system

For this work, CrN_xO_y and AlN_xO_y thin films were prepared by dc reactive magnetron sputtering, in a laboratory-sized deposition system (Fig. 2.7) [25]. The system is mainly composed by a deposition chamber, a vacuum system, a gas flow control system, an electrical system, a pre-chamber and a control unit.

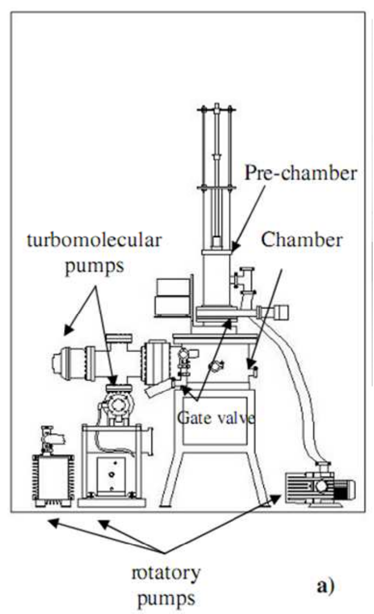

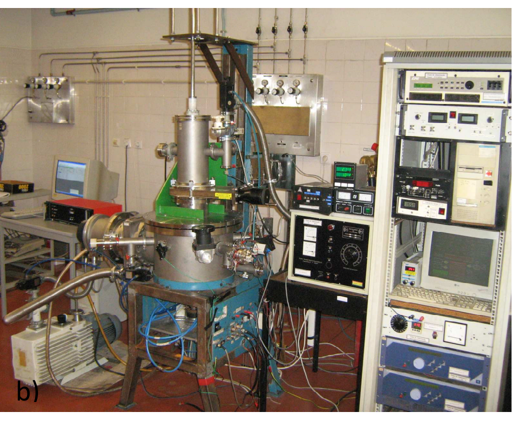

Fig.2.7. ***a)*** *Schematic representation of the home-made deposition system;* ***b)*** *image of the deposition system*

2.2.1. Deposition chamber

The deposition chamber has a cylindrical shape, with a diameter close to 0.4 m and with a volume of approximately 0.14 m^3. The system can accommodate four magnetrons in a closed or mirrored field configuration. In the case of the samples deposited in framework of this thesis, only one vertically rectangular magnetron (unbalanced of type 2), in a closed field configuration, was used [26]. The target rest in front of the water cooled magnetron with dimensions 200×100×6 mm (Fig. 2.8).

Fig. 2.8. *Image of the inside of the deposition chamber*

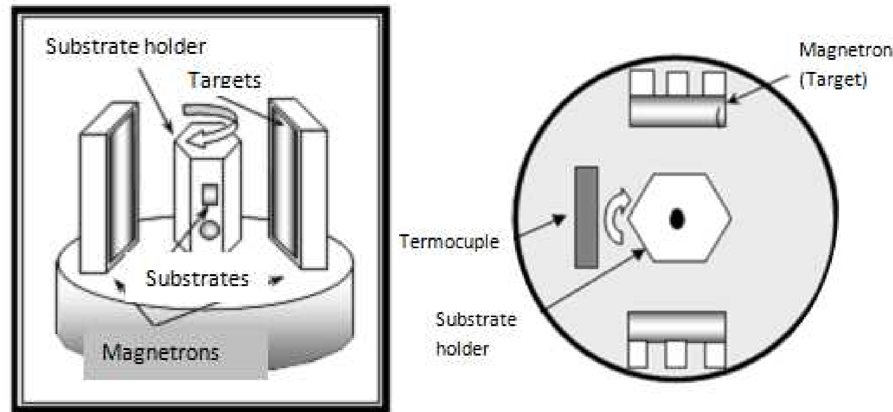

Fig. 2.9. *Schematics representation of the disposition of the magnetron and substrate holder in the interior of the chamber*

2.2.2. Vaccum system

The vacuum system is composed by three rotatory pumps and two turbomolecular pumps see Fig. The primary vacuum (~0.5 Pa) in the deposition chamber is obtained by two parallel rotatory pumps: a Trivac D8B and a Balzers DUO 012A, with nominal pumping speeds of 2.36 L/s and 3.33 L/s, respectively. The base pressure was obtained by the two parallel turbomolecular pumps: a Balzers TPU200 and an Alcatel PTM 5400, with nominal pumping speeds of 190 L/s and 400 L/s, respectively. The overall pumping speed was measure to be approximately 356 L/s. The pressure inside the chamber was controlled by two pressure gauges: a pirany for primary vacuum (model PRL 10) and a penning (model CP25-K) for secondary vacuum, both models from Edwards.

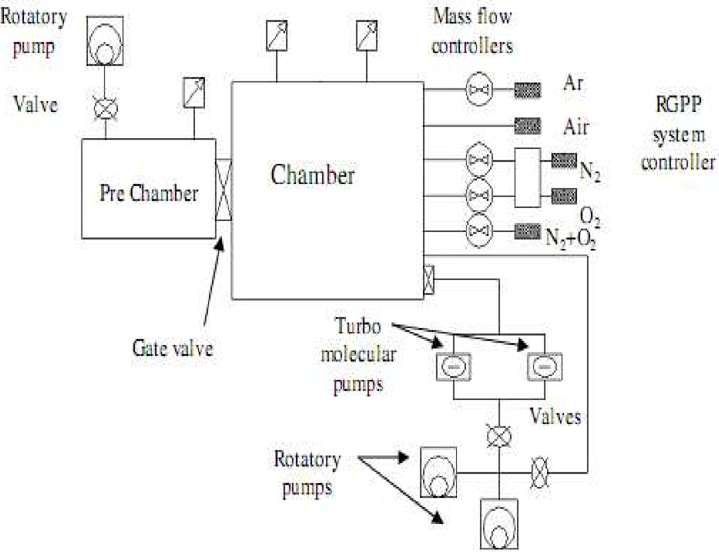

Fig. 2.10. *Schematics of the vacuum system*

2.2.3. Pre-chamber and electric system

A rotatory pump, Edwards E2M18, was connected to a pre-vacuum chamber, with a pumping speed of 5.7 L/s. This pump allowed reaching to a primary vacuum in the order of 2 Pa, before the substrates (placed at the substrate holder) were transferred, through a gate valve (placed between the main chamber and the pre-chamber) to the main chamber. This allowed reaching the base pressure much faster. The electrical system is composed by two Hüttinger dc generators, a PFG 2500 DC and a PFG 7500 DC, with a maximum output power of 2.5 and 7.5 kW, respectively. A Pulsed power supply from ENI (model RPG 50) was used for the etching of the substrates (in-situ pre-cleaning). A current rectifier from Delta (Portugal) was used for the biasing of the substrates (maximum current of 2 A). The power supplies, as well as the different opening/closing of the valves and the gas feeds are computer controlled.

2.3. Samples preparation

Magnetron sputtering has become the process of choice for the deposition of a wide range of industrially important coatings. Examples include hard, wear-resistant coatings, low friction coatings, corrosion resistant coatings, decorative coatings and coatings with specific optical, or electrical properties [12].

Recently,a new class of materials has become very important for several technological fields, but poorly explored, the oxynitrides: MeNxOy (with Me=metal). The importance of this class of materials is based on the fact that oxygen is much more reactive than nitrogen and, due to this higher reactivity, the addition of a small amount of oxygen to a growing transition metal nitride film induces the production of ionic metal–oxygen bonds in a matrix of roughly covalent metal–nitrogen bond. Among the group of already studied oxynitrides, aluminium oxynitride (AlN_xO_y) and chromium oxynitride (CrN_xO_y) have many interesting applications in different technologic fields, but the available knowledge on these two systems, specially the first one, is somewhat limited. The use of aluminium oxynitride is not yet very common, nevertheless there are some very few applications in the field of microelectronics, such as dielectric in multilayer capacitors, barrier diffusion [22].

On the other hand, chromium oxynitride coatings have been investigated for over a decade and were successfully implemented in many areas. These coatings exhibit excellent properties like high hardness, oxidation resistance and chemical stability and have used also as temperature dependent resistors in thermal radiation detectors [27]. Taking in to account that the properties of the materials significantly depend on their interdependence of composition, structure and morphology, an understanding of these relationships will be a major concern in this work. For this purpose a set of Al and Cr–N–O thin films was prepared and analyzed in terms of all the above items. This study will allow the establishment of limits for practical applicability of devices coated with these materials, providing new areas of application and supplying criteria for new materials design for specific applications.

In basic terms, the work consisted in the deposition of different series of samples, in which the main purpose was to study in detail the influence of deposition parameters in film's properties in special the influence on electrical and optical properties.

Two series of samples were prepared, a first one with chromium oxynitride (set of 15 samples) and a second one of aluminium oxynitride (a set of 15 samples).

The first series, noted in the text as series CrN_xO_y, is a set of 15 samples that were prepared with the substrate holder positioned at 70 mm from the target in a rotation mode-type (9 rpm), using a gas atmosphere composed of argon and a reactive gas mixture composed of 85 % N_2 + 15 % O_2 (17:3 ratio). The working pressure was approximately constant during the depositions (varying slightly between ~0.4 and 0.5 Pa).

The substrates used were:

i) glass (used for optical and electrical characterization);

ii) silicon (100 – for structural, composition and morphological analysis).

The substrates were grounded and kept at a constant temperature of approximately 373 K during the 1.5 or 2 h deposition. A delay time of five minutes was used before positioning the surface of the samples in front of the Cr target (99.6 at.% purity). This delay time was used to avoid the deposition of material resulting from the target cleaning process and also to assure a practically constant deposition temperature of the substrates during film growth.

Table I– Summary of deposition parameters selected for the deposition of CrN_xO_yfilms.

Parameter	Value
Traget current density	75 $A.m^{-2}$
Argon flow	70 sccm
Argon partial pressure	0.3 Pa
Gas mixture (N_2+ O_2) flow	0 to 32 sccm
Gas mixture (N_2 + O_2) partial pressure	0 to 0.256 Pa

The second series, noted in the text as series AlN_xO_y, is a set of 16 samples that were prepared using the same basic conditions as the first series (series AlN_xO_y).

The coated substrates were:

iii) glass (used for optical and electrical characterization);

iv) silicon (100 – for structural, composition and morphological analysis).

Table II summarizes the deposition conditions used for this second series of samples.

Table II – Summary of deposition parameters selected for the deposition of AlN_xO_yfilms.

Parameter	Value
Traget current density	75 $A.m^{-2}$
Argon flow	70 sccm
Argon partial pressure	0.3 Pa
Gas mixture (N_2+ O_2) flow	0 to 11.3 sccm
Gas mixture (N_2 + O_2) partial pressure	0 to 0.0902Pa

2.4. Conclusion

This chapter presents the deposition system used for the deposition of thin films systems regarding the AlN_xO_y and CrN_xO_y type. Was used the reactive magnetron sputtering in special the DC magnetron sputtering in a system consisting in an Cr and Al target with a high purity (99.6%).

Substrates that were used for the deposition are glass and silicon, and were deposited a set of 10 samples of CrN_xO_y type and 15 samples of AlN_xO_y type. The deposition process is divided in two major parts: the etching and the actual deposition.

The two sets of thin films of oxynitride type were deposited in a static way using a gas atmosphere composed of argon and a reactive gas mixture composed of oxygen and nitrogen with a constant temperature of about 373 K during the deposition, which lasted about 1.5 or 2 hours. A delay time of five minutes was used before positioning the surface of the samples in front of the Cr and Al. This delay time was used to avoid the deposition of material resulting from the target cleaning process and also to assure a practically constant deposition temperature of the substrates during film growth.

References

[1]- D. Ross Mcgregor Jr, Growth optimization and characterization of reactively sputtered zirconium nitride thin films for III-IV buffer layer applications

[2]- S. M. Rossnagel, in Sputter Deposition, Sproul WD, Legg KO, editors. Opportunities for Innovation: Advanced Surface Engineering. Switzerland: Technomic Publishing Co, 1995.

[3]- P. Sigmund, Topics in Applied Physics: Sputtering by Particle Bombardment I, ed. R. Behrisch, v. 47, Springer Verlag, Berlin, 1981.

[4]- J. L. Vossen, J. J. Cuomo, in Thin Film Processes, eds. J. L. Vossen and W. Kern, Academic Press, New York, 1978.

[5]- W. D. Westwood, in Microelectronic Materials and Processes, ed. R. A. Levy, Kluwer Academic, Dordrecht, 1989.

[6]- B. N. Chapman, Glow Discharge Processes, Wiley, New York, 1980.

[7]- J. A. Thornton, Thin Solid Films 54 (1978) 23.

[8]- H. Conrads, M. Schmidt, Plasma Sources Sci. Technol. 9 (2000) 441.

[9]- N. Kumar, K. Pourrezaei, B. Lee, E. C. Douglas, Thin Solid Films 164 (1988) 417.

[10]- R. A. Powell, S. M. Rossnagel, Thin Films: PVD for Microelectronics: Sputter Deposition Applied to Semiconductor Manufacturing, Academic Press, San Diego, 1999.

[11]- G. K. Wehner, G. S. Anderson, Vacuum Technology, Thin Films and Sputtering: an Introduction, ed. R. V. Stuart, Academic Press, New York, 1983.

[12]- P.J. Kelly, R.D. Arnell, Vacuum 56 (2000) 159-172.

[13]- Sproul WD, Legg KO, editors. Opportunities for Innovation: Advanced Surface Engineering. Switzerland: Technomic Publishing Co., 1995.

[14]- K. Wasa, M. Kitabatake, H. Adachi; Thin film materials technology; Sputtering of compounds materials , ed. Springer (2004), pp. 71-111.

[15]-Musil J,Kadlec S. Vacuum 1990; 40 (5) :435-44

[16]- L. I. Maissel, R. Gland (eds.) in Handbook of Thin Film Technology, McGraw – Hill, New York, USA, 1970.

[17]- Gencoa Product Information: V-Tech Magnetrons. Gencoa, 4 Wavertree Boulevard South, Liverpool L7 9PF, UK. Web address: www.Gencoa.com.

[18]- Nyaiesh AR. Thin Solid Films 1981; 86: 267-77.

[19]- W. D. Westwood, S. Maniv, P.J. Scanlon, J. Appl. Phys. 54 (1983) 6841.

[20]- I.Safi, Surface and Coatings Technology 127 (2000) 203-219.

[21]- L. B. Freund, S. Suresh, Thin Films Materials. 2003.

[22]- J. Borges, F. Vaz, L. Marques, Appl. Surf. Sci. 257 (2010) 1478.

[23]- D. Depla, S. Mahieu, Reactive sputter deposition, Springer (2008)

[24]- T. Nyberg, S. Berg, U. Helmersson, K. Kartig, Appl. Phys. Lett. 86 (2005) 16410.

[25]- E. Ribeiro, A. Malczyk, S. Carvalho, L. Rebouta, J. V. Fernandes, E. Alves, A. S. Miranda Surf. Coat. Technol. 151-152 (2002) 515.

[26]- B. Window, N. Savvides, J. Vac. Sci. Technol. A 4 (1986) 196.

[27]- R. Mientus, R. Grotschel, K. Ellmer, Surface & Coatings Technology 200, (2005), p. 341–345.

Chapter III

Prepared Samples

3.1. Introduction

Typically, PVD processes are used to deposit films with thicknesses in the range of a few nanometers to thousands of nanometers; however they can also be used to form multilayer coatings, graded composition deposits, very thick deposits and freestanding structures [1].

Reactive sputtering is well-known to be a suitable technique to deposit several types of thin films, including the cases of metallic oxide and nitride thin films, and specially those of that are related to this work. Regarding its application, it is known that different films, using almost all periodic table elements, for the most varied purposes are being produced by Physical Vapour Deposition techniques, where reactive sputtering is one of the most used methods. Reactive sputtering has some important characteristics, among which, its high versatility should be one of most important ones, connected to an easy control of the deposition parameters and thus particularly suitable to modulate the final properties of the coatings [2-7].

Typically, a problem in reactive sputter deposition is to prevent the “poisoning” of the sputtering target by the formation of a compound layer on its surface. Poisoning of a target surface greatly reduces the sputtering rate and sputtering efficiency. This problem is controlled by having a high sputtering rate (magnetron sputtering) and controlling the availability of the reactive gas, such that there will be enough reactive species to react with the film surface to deposit the desired compound, but not so much that it will unduly poison the target surface [1].

Reactions in the gas phase are ruled out for the same reasons that ions can not be neutralised in the gas phase (there is no mechanism which can dissipate the heat of neutralisation to conserve both momentum and energy in a two-body system, therefore it can only happen at a surface) .These cathode reactions are seen to increase suddenly at some rate of reactive gas flow. If flow control of reactive gas is used, such reactions are marked by a change in the impedance of the operating plasma, an abrupt increase in the system pressure (or more precisely in the reactive gas pressure), a drastic drop in the deposition rate and a change in the film composition from metal-rich to gas-rich [8].

Within the different controls that are done in modern laboratories (and production lines), there are always special features that need to be taken into account if high quality films are expected to be prepared the so-called process instabilities. If these process instabilities are

always seen as undesirable and responsible for deviations in film's responses (electrical, optical, mechanical, among others), the case of decorative films is particularly serious since it will have severe consequences in thin film colour. Among others, typical instability phenomena of experimental parameters are frequently met with the reactive process involving one metallic target with one (or more) reactive gas(es) [9-13].

In reactive sputtering, the reaction at the cathode is called an oxide mode and the reaction at the substrate is called a metallic mode. The deposition rate is significantly affected by the surface condition of the target and/or the mode of the reactive sputtering. Deposition rates will show the hysteresis curve with the variation of the flow rates of the reactive gas [14].

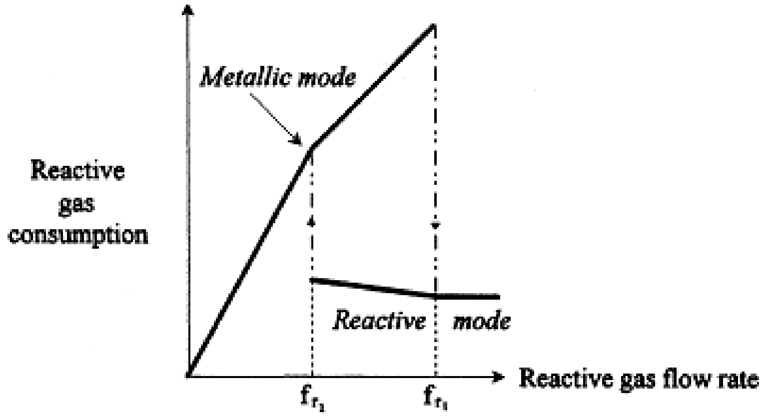

Fig. 3.1. *Hysteresis behaviour of reactive gas consumtion*

The hysteresis effect is very undesirable and has to be eliminated, if flow control of reactive gas is used, because the process is unstable inside this region [8]. At one value of f_r, it is likely to deposit compound films of different stoichiometries and thus physical properties. This is due to the existence of two stable operating states corresponding to an individual value of f_r ,when f_r is in the region of hysteresis. Fast and sophisticated process control systems are required in order to operate inside this region.

3.2. Characterization techniques

Instead of light, the Scanning Electron Microscopy (SEM) uses secondary electrons emitted from the surface to form the image. The intensity and angle of emission of the electrons depend both on the surface topography and the material. The angle of emission depends on the surface morphology so the spatially-collected electrons allow an image of the surface to be collected and visually presented [15].

The SEM technique provides the investigator with a highly magnified image of the surface of a material that is very similar to what one would expect if one could actually "see" the surface visually. In the SEM, a source of electrons is focused (in vacuum) into a fine probe that is rastered over the surface of the specimen. As the electrons penetrate the surface, a number of interactions occur that can result in the emission of electrons or photons from (or through) the surface. A reasonable fraction of the electrons emitted can be collected by appropriate detectors, and the output can be used to modulate the brightness of a cathode ray tube (CRT) whose x- and y-inputs are driven in synchronism with the x-y voltages rastering the electron beam. In this way an image is produced on the CRT; every point that the beam strikes on the sample is mapped directly onto a corresponding point on the screen [1].

The principle images produced in the SEM are of three types: secondary electron images, backscattered electron images, and elemental X-ray maps. Secondary and backscattered electrons are conventionally separated according to their energies.

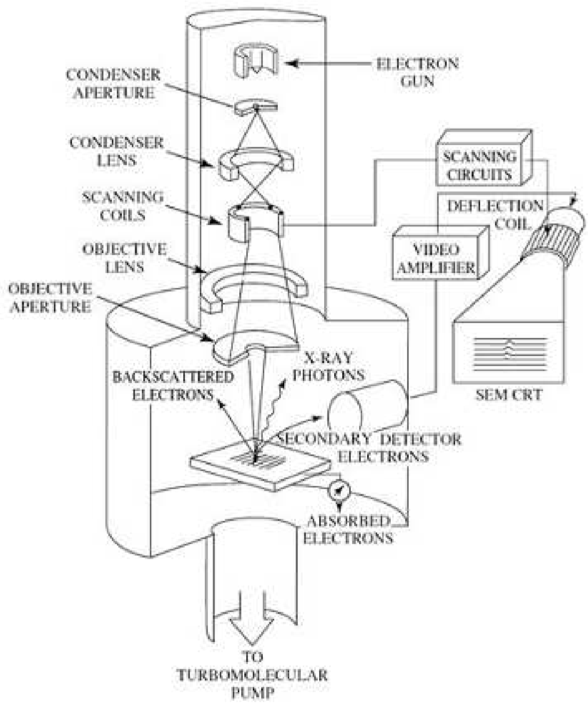

Fig. 3.2. *Schematic of the scanning electron microscope*

The most common imaging mode relies on detection of this very lowest portion of the emitted energy distribution. Their very low energy means they originate from a subsurface depth of no larger than several angstroms. The image magnification is then simply the ratio of scan lengths on the CRT to that on the specimen.

Backscattered electrons are the high- energy electrons that are elastically scattered and essentially possess the same energy as the incident electrons. The probability of backscattering increases with the atomic number Z of the sample material. Since the backscattered fraction is not a very strong function of Z (varying very roughly as - 0.05Z for primary electron beams employed in the SEM).

A SEM is like a large X-ray vacuum tube used in conventional X-ray diffraction systems. Electrons emitted from the filament (cathode) are accelerated to high energies where they strike the specimen target (anode). In the process, X-rays characteristic of atoms in the irradiated area are emitted. By an analysis of their energies, the atoms can be identified and by a count of the numbers of X-rays emitted the concentration of atoms in the specimen can be determined [16].

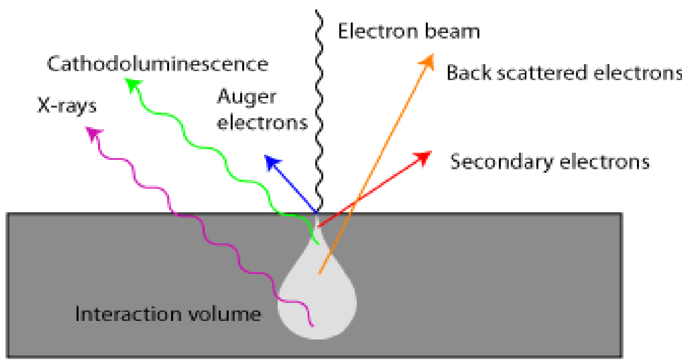

Fig. 3.3. *Electron and photon signals emanating from tear-shaped interaction volume during electron-beam impingement on specimen surface*

All these signals are the result of strong electron-specimen interactions, which depends on the energy of the incident electrons and the nature of the specimen and can be used to form images or diffraction patterns [17-19]. As the higher energy primary electrons penetrate the solid, they undergo scattering which increases the interaction volume [20]. Fig.3.4 shows the range and spatial resolution of backscattered electrons, secondary electrons, X-ray and Auger electrons incident on a solid.

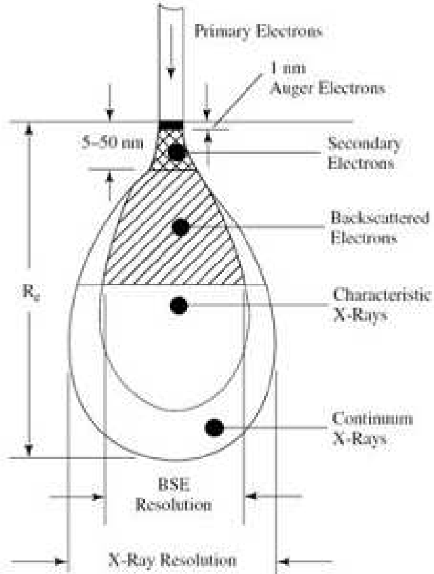

Fig. 3.4. *Summary of the range and spatial resolution of backscattered electrons, secondary electrons, X-ray and Auger electrons incident on a solid*

Some of the primary electrons will be backscattered toward the surface with little or no energy loss; these high energy electrons yield better image contrast in many situations [1, 21]. Energetic primary electrons ionize atoms in the solid producing X-rays which are characteristic of the elements that are present [21].

Samples to be analyzed in SEM have to be: stable in high vacuum, stable physical and chemically and have electrical conductive in the surface. Due to the last condition (and because some samples have high resistivity) the samples are coated with a thin film of usually gold to ensure electrical conductivity [19].

In our case the determination of the thickness was made on a Leica Cambridge S-360 SEM that is equipped with a fully automated stage, with a maximum travel of 100 mm in the X and Y axes, and 50 mm in the Z axis. In addition to all of the features of the S-200 this instrument has the following capabilities:

High resolution digital capture and storage of SEM images using the PC based Orion software. Capture and store images at 2992 x 2272 resolution in tiff or jpeg format. Storage of stage positions, allowing the user to return to any preselected position [22].

Fig. 3.5. *Scanning electron microscope Leica Cambridge S-360*

Thickness is one of the most important thin-film parameters since it largely determines the properties of a film. On the other hand, almost all properties of thin films depend on the thickness and can therefore be used for the thickness measurement. From this fact follows a great diversity in methods of measurements. The very concept of thickness depends on the method of measurement selected or, more accurately, different methods of measurement may yield different results, different thickness for the same film [23].

There are many direct and indirect techniques for measuring the thickness of a deposited thin film. A general problem in measuring film thickness is the definition of the "surface." Since films have a low thickness, substrate surface roughness can play a major role in the thickness measurement. Film and coating thickness may be defined in three ways: geometrical thickness, mass thickness, property thickness.

Different thickness measuring techniques may give differing values for the thickness. Many of the indirect thickness measuring techniques require careful calibration. Often thickness is determined by depositing the film on a smooth substrate (witness plate) in an equivalent position and determining the geometrical thickness. Since the growth and geometric area on the witness plate is different from that of the real substrate, the thicknesses may differ but the measurement is good for relative values from run-to-run [23].

A large variety of different methods are shown in figure 3.6.

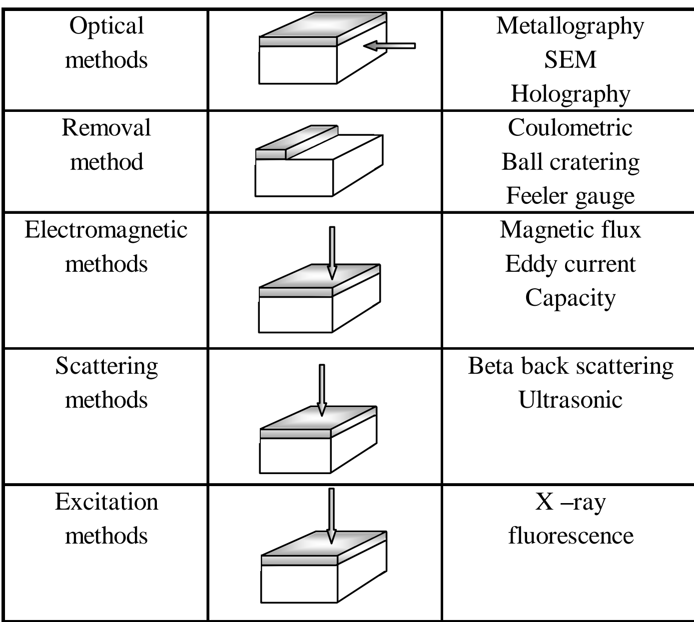

Fig. 3.6. *Different methods of measuring the coating thickness*

3.3. Results and discussion

3.3.1. Chromium oxynitride

Target potential

The characterization of target voltage is always seen as a simple, but also powerful technique, giving important indications on the process characteristics. In fact, and in terms of industrial production, this characterization is often used as the main measure for quality control. Since in this work a mixture of oxygen and nitrogen was used as a reactive gas, it is possible that the formation of oxide and nitride compounds takes place at the target surface, and thus ruling both potential and deposition rate behavior.

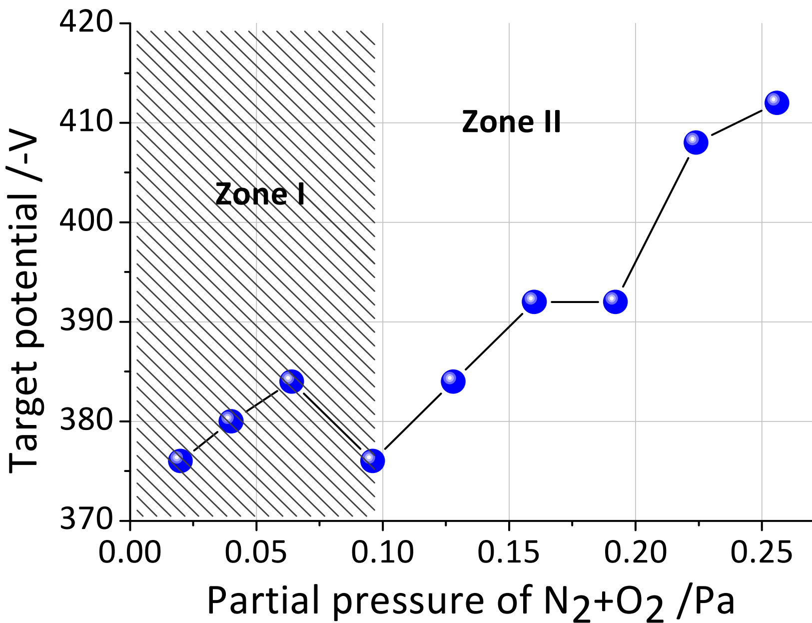

Fig. 3.7. *Evolution of the target potential, as a function of the partial pressure of reactive gas (N_2+O_2). The pressure was measured prior to discharge ignition*

From the analysis of the target potential evolution with reactive gas pressure one can observe two major deposition regimes for the prepared samples. A first regime with gas partial pressures between 0.01 and 0.1 Pa and characterized by relatively low target voltages, has values varying only slightly around -380 V. The set of samples within this zone were prepared with reactive gas flows lower than 8 sccm, exhibiting metallic-like surface tones. A second zone follows, for partial gas pressures between 0.1 and 0.27 Pa, where the target voltage increased gradually from -375 V to values close to -420 V. Due to this variation of target voltage, one would expect a gradual change in the growth modes of the samples within

this zone, as well as in its properties. This assumption was firstly confirmed by the sudden modification in the surface appearance of the coatings within this second zone, which varied from metallic-like to interference-like ones.

To explain the behaviour of the target voltage with the reactive gas pressure, one has to consider the gettering of the reactive gas by the target material, as shown by Berg et al. [24], leading to the formation of a compound layer on the target surface and thus, influencing the reactive gas partial pressure and also the ion-induced secondary electron emission (ISEE) coefficient of the target material [25].

In terms of target voltage, it is widely known and accepted that the minimum voltage required to sustain the magnetron discharge is given by:

$$V_{min} = \frac{W_0}{\gamma_{ISEE}\, E_{\varepsilon_i \varepsilon_e}} \qquad \text{(eq.3.1)}$$

with W_0 representing the effective ionization energy; γ_{ISEE} the ion induced secondary electron emission coefficient; and E the effective gas ionization probability. The other two parameters, ε_i and ε_e, are close to unit for magnetron sputtering, which means that the cathode voltage essentially depends on the γ_{ISEE} coefficient [26]. The dependence of this coefficient on the reactive gas partial pressure varies for different target materials and reactive gases [27]. In short the Berg model describes the gettering of the reactive gas by the target material which influences the reactive gas partial pressure. At low reactive gas flow, the reactive gas is almost completely gettered and hence the target condition remains metallic. When on increasing the reactive gas flow the maximum amount of reactive gas which can be gettered is reached, the reactive gas partial pressure increases and the target becomes completely poisoned. Depending on the experimental conditions this change from metallic to poisoned mode can occur abruptly [28].

In this respect, it is widely known and accepted that the minimum voltage required to sustain the magnetron discharge is roughly inversely proportional to the γ_{ISEE} coefficient of the target material [27]. The dependence of this coefficient on the reactive gas partial pressure varies for different target materials and reactive gases, increasing for some metals like Al and Y, with increasing reactive gas incorporation on the target, while for other materials, like Cr, Ti, Zr decreases with the reactive gas incorporation [26]. For the present case, at low reactive gas flow, the reactive gas is almost completely gettered and hence the target condition remains metallic, which explains the low constant target voltage observed for Cr target. On increasing

the reactive gas flow, the amount of gas that can be gettered by the Cr target is reached, the reactive gas partial pressure increases and the target becomes gradually poisoned, which explains the steady increase in the target voltage observed for then set of samples that were indexed to the second zone.

Deposition rate

Since deposition rate can influence the crystallinity and structural defects of the coatings and consequently the final properties of the thin films, the first characterization done was the evaluation of the deposition rate as a function of the gas mixture (N_2+O_2) partial pressure.

Being a direct reflex of the material that constitutes the growing film, and thus related with the atmosphere present within the reactor, the characterization of the deposition rate enables to follow the first differences in the prepared films and, above all, to establish some rules of thumb regarding the types of films that have been grown: metallic-like, oxide-like, etc.

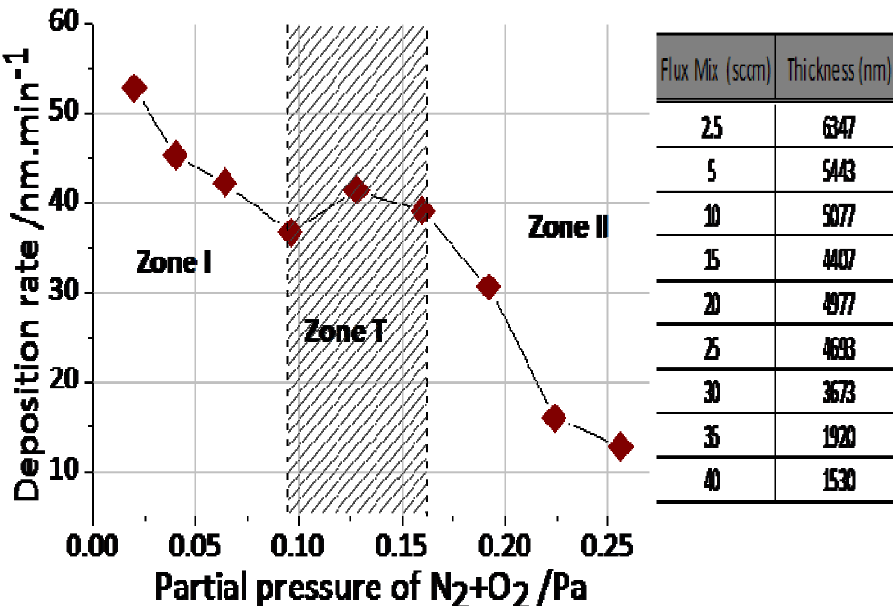

Flux Mix (sccm)	Thickness (nm)
2.5	6347
5	5443
10	5077
15	4407
20	4977
25	4693
30	3673
35	1920
40	1530

Fig. 3.8 *Evolution of the deposition rate as a function of the partial pressure of reactive gas (N_2+O_2). The pressure was measured prior to discharge ignition*

Following the variation of target potential, the deposition rate measurements reveal different types of films, which seem to clear out the analysis made above of the different film depositions. The evolution of deposition rate, Fig. 3.8, indicates that the set of samples that were firstly divided into two major zones after the target potential analysis, should be in fact split into 3 different modes (regimes) – i) a set of samples that were deposited within a metallic mode regime, which will be indexed from hereafter as zone I films; ii) a second set of samples that were deposited in an compound mode (oxide) regime, indexed from hereafter as zone II films; and in between, a set of films that seem to have been deposited in a some kind of transition regime, which will be noted as being in a zone T.

Regarding the available literature about this deposition rate variation issue, and based on Safi's hysteresis behaviour of reactive magnetron sputtering [29], Spencer et al. [30] proposed a conceptual model of the reactive sputtering process, in which the deposition rate variations were the motive of extensive analysis. This model describes the effects of raising the reactive gas partial pressure at the target and the substrate.

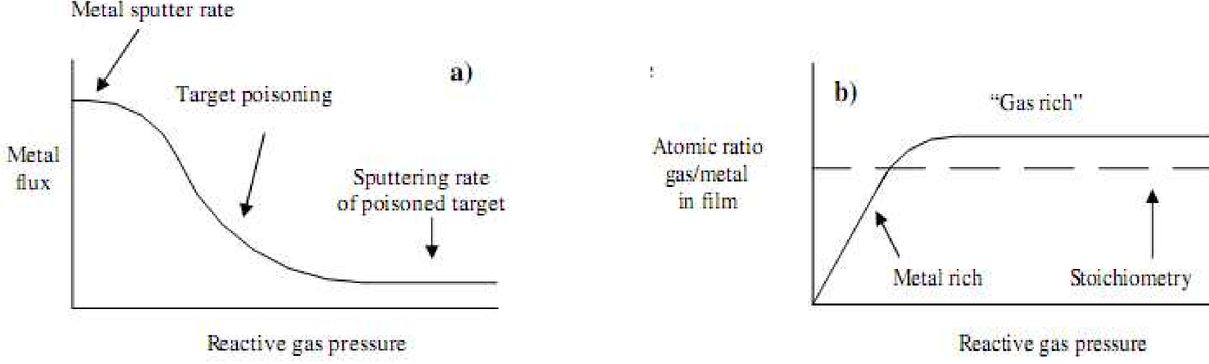

Fig 3.9. *The origins of the reactive gas consumption reproduced from Spencer et al. [22]; **a)** Evolution of the metal flux as a function of reactive pressure; **b)** Evolution of the atomic ratio gas/metal as a function of reactive gas pressure*

At the target, a partially poisoned surface results when the poisoning rate is higher than the cleaning rate. Since the sputtering yield of metal atoms from a poisoned surface is less than that from a pure metallic target, the metal flux from the target decreases with increasing reactive gas partial pressure until the entire target is poisoned, as can be seen in Fig. 3.9a. At the substrate, when the reactive gas partial pressure is low, the formation rate of the compound film is limited by the impact rate and utilization of the reactive gas atoms and

hence a metal rich, or sub-stoichiometric, film is deposited. Since the impact rate of the reactive gas atoms increases with its partial pressure, the reactive gas content of the compound film increases with the reactive gas partial pressure until a gas-rich, or over-stoichiometric saturated, film is deposited Fig. 3.9b.

The first regime – metallic mode, includes the group of samples prepared with reactive gas flows up to 8 sccm (corresponding to partial pressures varying from 0.01 to 0.1 Pa), revealing higher deposition rates (above 35 nm/min), which is characteristic of the sputtering process occurring in the metallic regime [31].

For reactive gas partial pressures above 0.16 Pa, there is a clear tendency for a progressive decrease of the deposition rate, reducing from roughly 40 nm/min. to a value close to 10 nm/min. at the highest reactive gas flow. The progressive decrease of deposition rate within the oxide zone (zone II) is a consequence of the well-known poisoning effect of the target by both reactive gases [32]. Both chromium nitride and oxide layers form at the surface of the Cr target. Since the sputtering yield of both compounds is lower than that of Cr, a decrease in the deposition rate is expected. Between these two main zones (corresponding to the group of samples prepared with reactive gas flows between 12 and 20 sccm), one can clearly distinguish the previous mentioned transition zone, which maybe associated to the transition regime between the metallic and compound regime in the hysteresis cycle of pure nitrides, where the deposition rate tends to stabilize at about 40 $nm.min^{-1}$. The fact that the deposition rate does not change significantly induces that the set of samples that were prepared within this growth mode will probably reveal very similar characteristics, namely in what concerns to morphology and structure, and thus their set of basic properties. The almost consistency in the deposition rate values maybe due to the almost constant target potential values, consistent with an almost steady state of the sputtering process.

Morphology of the films

Fig. 3.10 presents Scanning Electron Microscopy (SEM) micrographs of the cross-section morphologies of the films relevant for all three zones.

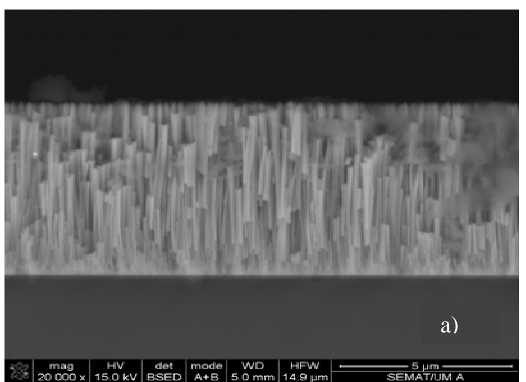

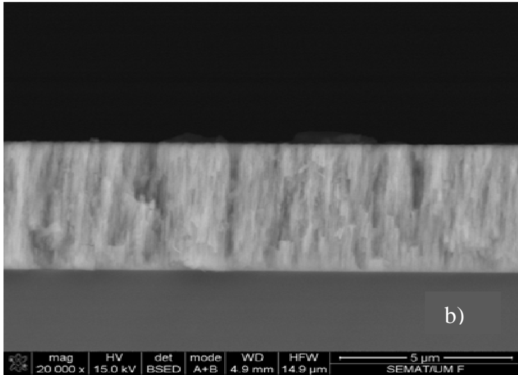

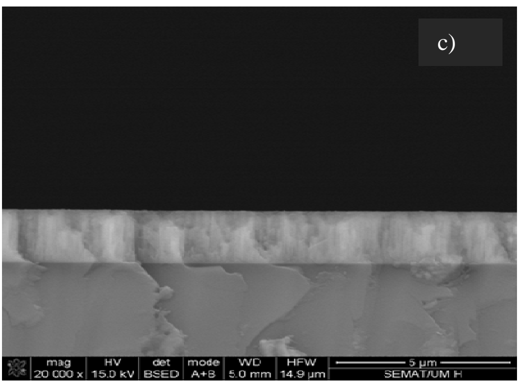

Fig. 3.10. *SEM cross-sections images of the films:* ***a)*** *Zone I,* ***b)*** *Zone T,* ***c)*** *Zone II*

Regarding the samples deposited, they developed a typical columnar microstructure that is very well correlated with the decrease in the deposition rate presented and discussed in Fig. 3.8. With the increase of the partial pressure of reactive gas mixture the type of the growth is changed from a columnar-like type in zone I were the amount of metallic atoms sputtered are very high to a more dense columnar-like growth for the samples that compose zone T.

The second zone indexed with low values of deposition rate and with a completely poisoned chromium target reveals a very dense microstructure with a less pronounced columnar morphology.

3.3.2. Aluminium oxynitride

Target potential

Fig. 3.11 shows the evolution of target potential, –V, of the different coatings as a function of the gas mixture (N_2 +O_2) partial pressure.

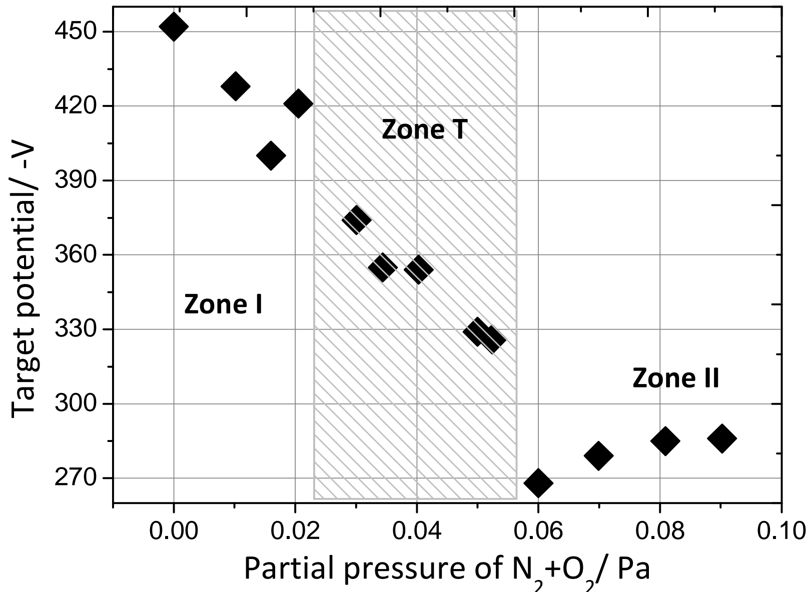

Fig. 3.11. *Evolution of the target potential, as a function of the partial pressure of reactive gas (N_2+O_2). The pressure was measured prior to discharge ignition*

As it can be observed, the target potential varies from about 450 V, for an atmosphere without reactive gas, to values between 428 and 422 V, when the reactive gas partial pressures vary from 0.01 to 0.02 Pa, respectively. When the partial pressure reaches the value of approximately 0.03 Pa, there is a significant decrease in the target potential, dropping about 11% to a value of about374 V. This decrease persists until a minimum value of 268 V is reached for a reactive gas mixture partial pressure of 0.06 Pa. Above this pressure, the target potential remains approximately constant.

According to the obtained results in Fig. 3.11, one might identify two main zones, with a transition zone between them like the case of CrN_xO_y discussed before. The first one–zone I, is observed for gas mixture partial pressures up to 0.02Pa, corresponding to high target potentials. A second zone–zone II–is indexed to the films prepared with gas partial pressures of 0.06 Pa and above, which are characterized by low values of target potential.

Between these two zones, one can consider a transition zone–zone T ($0.03Pa \leq p_{N2+O2} \leq 0.05Pa$), where target potential is decreasing gradually.

In the case of aluminium sputtering, the increase of the reactive gas partial pressure (oxygen/nitrogen) induces the formation of an oxide/nitride layer on the target surface, leading to an increase of the γ_{ISEE} coefficient and the consequent decrease of the discharge voltage (–V) [33-35]. This particular behavior can be used to explain the evolution of both target potential and deposition rate as a function of the reactive gas partial pressure observed. For the case of the films indexed to zone I, the target remains in a clean surface state (metallic mode), corresponding to a low value of the γ_{ISEE} coefficient thus explaining the high value of cathode voltage. The slight decrease of the target potential observed in zone I, can be explained by the raise of the γ_{ISEE} coefficient due to the increasing on the reactive gas ion implantation on the target. In the case of the films prepared with in the transition zone (zone T), the target is most likely becoming partially oxidized, since the free Gibbs energy of formation of aluminium oxide (alumina), $\Delta G^{0}_{f,at\ 298\ K}(Al_2O_3) = -1.58 \times 10^{3} kJ\ mol^{-1}$ is much lower than of the aluminium nitride, $\Delta G^{0}_{f,at\ 298\ K}(AlN) = -2{,}87 \times 10^{2} kJ\ mol^{-1}$ [36], meaning that oxidation of the target surface predominates over nitrating. In this zone T, the cathode voltage decreases with reactive gas pressure, due to the increase of γ_{ISEE} coefficient as the target becomes more and more oxidized.

Finally, in the case of the films prepared within zone II, the target is completely poisoned and thus the discharge voltage reaches its minimum value, meaning that the γ_{ISEE} coefficient is at its maximum value.

Deposition rate

Fig. 3.12 presents the evolution of the deposition rate, of the different coatings as a function of the gas mixture (N_2 +O_2) partial pressure.

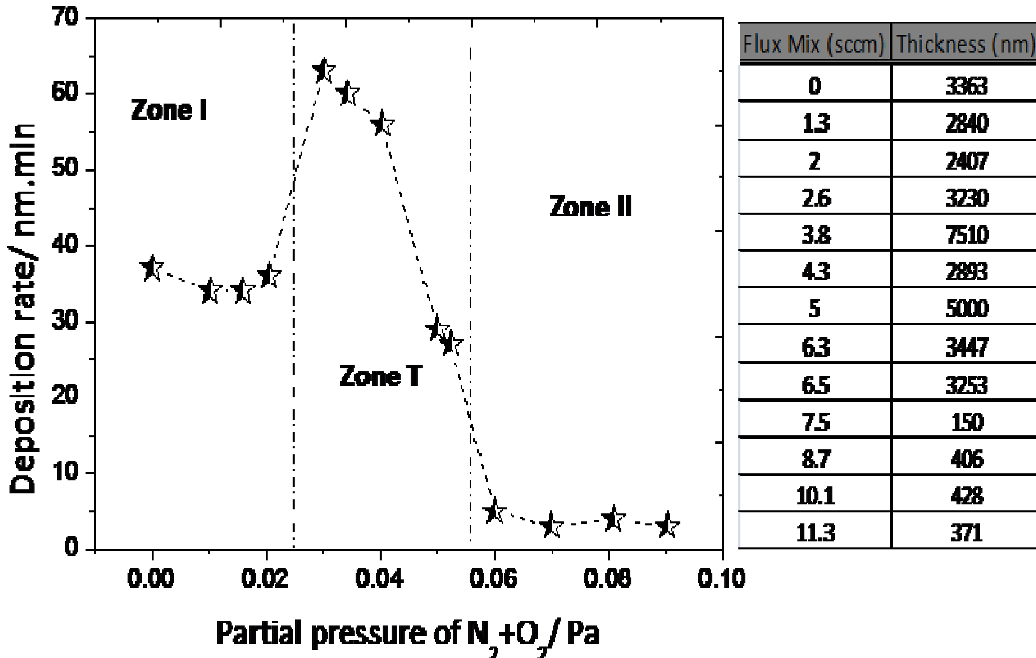

Flux Mix (sccm)	Thickness (nm)
0	3363
1.3	2840
2	2407
2.6	3230
3.8	7510
4.3	2893
5	5000
6.3	3447
6.5	3253
7.5	150
8.7	406
10.1	428
11.3	371

Fig. 3.12. *Evolution of the deposition rate as a function of the partial pressure of reactive gas (N_2+O_2). The pressure was measured prior to discharge ignition*

Regarding the deposition rate, Fig. 3.12 shows for zone I within the range of reactive gas partial pressures (0.00 Pa $\leq p_{N2+O2} \leq$ 0.02Pa), a deposition rate that remains approximately constant at a value around 35 nm.min^{-1}.

Zone T shows a significant increase of the deposition rate from about 43% to a value of 63 nm.min^{-1}, when the partial pressure is increased from 0.02 to 0.03 Pa. Increasing further the reactive gas pressure, the deposition rate decreases steeply until a minimum value of about 4–5 nm.min^{-1} is reached, for a gas mixture partial pressure of 0.06 Pa and above that is indexed in zone II.

In order to clarify the three zones evolution, one must take into account that reactive magnetron sputtering is a complex process, depending on many parameters that are commonly strongly correlated. The reactive gas used to sputter the target, not only reacts with the sputtered material in the plasma region, but also interacts with the cathode surface, leading to ion implantation or chemisorptions of reactive species on the target surface. These

processes modify the sputtering yield, thus affecting the deposition rate, but also the ion induced secondary electron emission coefficient of the target, which, in its turn, is closely related to the minimum sustaining discharge voltage. During reactive magnetron sputtering there are three general working regimes for the sputtered target: the first one, a so-called metallic mode, occurs when the partial pressure of reactive gas is too low to react with the metallic target, which remains clean. This induces the preparation of films with relatively high deposition rates and target voltages that can be relatively low in some cases [37], but also relatively high, such as the case demonstrated here for the aluminium oxynitrides.

This would be the case demonstrated here by the samples indexed to zone I. A second regime appears as a result of the increase of the reactive gas pressure, which starts to “poison” the target surface, resulting on a decrease of its sputter yield [8], and in a decrease of the deposition rates, to get her with a significant variation on the target potential values. This would be the case of the films prepared in the frame work of this study indexed to the transition zone. Finally, the third regime (target poisoning) occurs when the sputtered targets are close or completely poisoned, leading to a strong decrease in the sputter yield and consequently in the obtained deposition rate. In this case, the target voltages are commonly observed to be relatively low (or high) [38] in comparison to those observed for zone I. This would be the case of the films prepared for this study that were indexed to zone II.

Concerning the deposition rate of the films (calculated based on SEM observations), one should note that for the same deposition time, the thickness of the samples depends on the amount of material that arrives to the substrate, which is correlated with the amount of atoms sputtered from the target. Since the sputter yield of a poisoned target is less than that from a metallic target, it is expected that the deposition rate decreases as the partial pressure increases until the target becomes totally poisoned.

Morphology of the samples

Regarding the morphology of the Al-N-O system an analysis of the SEM images was made for a better understanding of the results from all the three zones as it this shown in fig. 3.13(a-c). The observation of the obtained results are revealing the type of growth of the films that present a significantly difference between the films prepared in zone I and those from zone T, whereas the zone I films present a typical columnar-like growth, the transition zone are very porous with a cauliflower-like growth. Therefore the high deposition rates within

zone T do not imply a higher quantity of material that was being deposited, but the formation of films with lower density.

The increase of the partial pressure within zone T induces a decrease of the deposition rate that is a direct consequence of the reduction of the target sputtering yield.

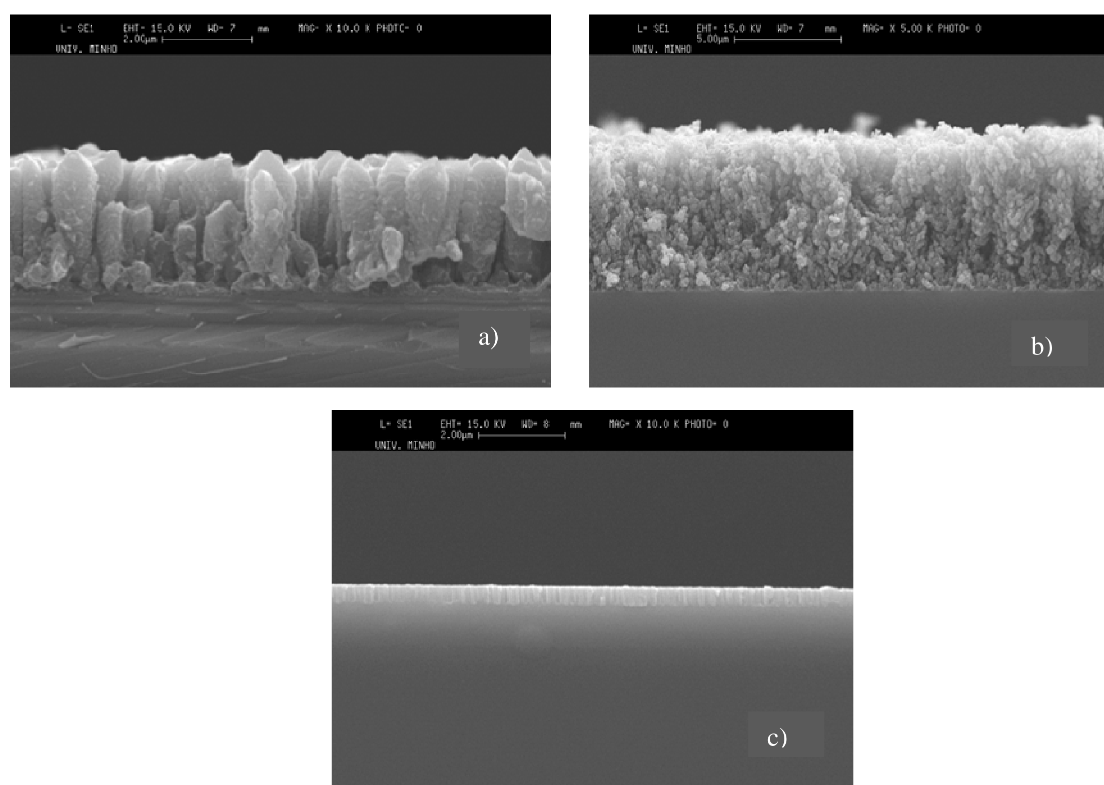

Fig. 3.13. *SEM cross-sections images of the films:* ***a)*** *Zone I,* ***b)*** *Zone T,* ***c)*** *Zone II*

Finally, zone II reveal a dense but featureless –type growth that is explained by the roughly constant deposition within this zone that is a consequence of the aluminium target that is completely poisoned and the amount of metallic atoms that are very low.

3.4. Conclusions

This chapter presents the fundamental characterizations of the coatings in special the target potential, deposition rate determined with the use of the thickness and morphology of these coatings.

The samples of the CrN_xO_y system presents an analysis of the evolution of the target potential dividing the coatings into two main zones, one with the relative small target voltage and the other area with values of the target voltages that increase gradually.

Instead, determining the deposition rate leads to a new classification of the samples meaning dividing them into three regimes. Zone I is an area consisting of deposited samples in a metallic regime, a zone T with samples deposited in a somewhat transition regime and the third zone indexed to as zone II with samples deposited in a compound (oxide) regime. In the case of morphology of deposited coatings they have developed a columnar type microstructure.

The system of AlN_xO_y type presents an analysis of the target potential in a continuously decreasing and the coatings are divided in three zones. Zone I is a zone with high values of target potential, zone T presents values of target potential that are gradual decreasing and zone II is characterized by low values of target potential. Deposition rate remains almost constant over zone I with a metallic regime, zone T shows a significant increase of the deposition rate and zone II shows a sharp drop of the deposition rate in the oxide type regime. The morphology of this system presents a typical columnar growth for zone I, the coatings from zone T are porous with an cauliflower type growth, as for the coatings from zone II they present a dense growth without specific form.

References

[1] Donald M. Mattox, Handbook of physical vapor deposition (PVD) processing, Westwood, New Jersey Noyes publications, (1998).

[2] S. Hofmann, Thin Solid Films 191 (1990) 335.

[3] G. Lemperière, J. M. Poitevin, Thin Solid Films 111 (1984) 301.

[4] S. Berg, T. Larsson, C. Nender, H. O. Blom, J. Appl. Phys. 63 (1988) 887.

[5] X. Chu, S. A. Barnett, M. S. Wong, W. D. Sproul, J. Vac. Sci. Technol. A 14 (1996) 3124.

[6] L. J. Meng, M. P. Dos Santos, Thin Solid Films 250 (1994) 26.

[7]- A. Billard, C. Frantz, Surf. Coat. Technol. 59 (1993) 41.

[8] I. Safi, Surface and Coatings Technology 127 (2000) 203-219

[9] W. D. Westwood, S. Maniv, P. J. Scanlon, J. Appl. Phys. 54 (1983) 6841.

[10] S. Berg, H. O. Blom, T. Larsson, C. Nender, J. Vac. Sci. Technol. A 5 (1987) 202.

[11] J. Heller, Thin Solid Films 17 (1973) 163.

[12] J. Affinito, R.R. Parsons, J. Vac. Sci. Technol. A 2 (1984) 1275.

[13] F. Shinoki, A. Itoh, J. Appl. Phys. 46 (1975) 3381.

[14] K. Wasa, M. Kitabatake, H. Adachi, Thin film materials technology, William Andrew, Inc. publications, (2004).

[15] C. Richard Brundle, Charles A. Evans, Jr and Shaun Wilson, Encyclopedia of Materials Characterization, (1992).

[16] Milton Ohring, The materials science of thin films, Academic press., (1992).

[17] Cao, Guozhong and Brinker, C Jeffrey, [ed.]. Annual review of nano research. s.l.: World Scientific Publishing Co. Pte. Ltd., Vol. 2, (2008).

[18] Yao, Nan and Wang, Zhong Lin. Handbook of microscopy for nanotechnology. s.l.: Kluwer Academic Publishers, (2005).

[19] Sá, C. Morphologic, microstructural and microanalitic characterization by scanning electron microscope (SEM) and X-ray microanalises (EPMA:EDS/WDS), CEMUP, Porto: s.n., (2007).

[20] Schroder, Dieter K., Semiconductor material and device characterization, Handbook: John Wiley & Sons, Inc, (2006).

[21] Bunshah, R. F., [ed.]. Handbook of Deposition Technologies for Films and Coatings, 2nd. Park Ridge: Noyes Publications, (1994).

[22] http://cgc.rncan.gc.ca/labs/ebeam/sem_guide_e.php

[23] K.S.Sree Harsha, Principles of Physical vapor deposition of thin films, (2007)

[24]. D. Depla, S. Mahieu, Reactive sputter deposition, Springer (2008).

[25]. D.A. Glocker, S.I. Shah, Thin Film Process Technology, edited by Institute of Physics Publising Ltd, (Bristol, UK, 1995).

[26]. P. Carvalho, J. M. Chappé, L. Cunha, S. Lanceros-Méndez, P. Alpuim, F. Vaz, E. Alves, C. Rousselot, J.P. Espinós, and A.R. González-Elipe: J. Appl. Phys. 103 (2008) 104907.

[27]. J. Borges, F. Vaz, L. Marques, Appl. Surf. Sci. 257 (2010) 1478.

[28]. F. Vaz, P. Carvalho, L. Cunha, L. Rebouta, C. Moura, E. Alves, A.R. Ramos, A. Cavaleiro, Ph. Goudeau, J.P. Rivière: Thin Solid Films 469-470 (2004) 11.

[29]. I. Horcas, R. Fernandez, J.M. Gomez-Rodriguez, J. Colchero, J.G. Herrero, A.M. Baro: Rev. Sci. Inst. 78 (2007) 013705.

[30]. E. Ando, S. Suzuki: Journal of Non-Crystalline Solids 218 (1997) 68-73.

[31]. M. Ohring, The Materials Science of Thin Films, edited by Academic Press, (New York, 1992).

[32] D. Depla, R. DeGryse, Target Surface and Coatings Technology 183 (2004) 184–189.

[33] D. Depla, R. DeGryse, Surface and Coatings Technology 183 (2004) 190–195.

[34] S. Venkataraj, D. Severin, R. Drese, F. Koerfer, M. Wuttig, Thin Solid Films 502 (2006) 235–239.

[35] N Jacobson, Journal of Chemical Education 78 (2001) 814.

[36] P. Carvalho, F. Vaz, L. Rebouta, L. Cunha, C.J. Tavares, C. Moura, E. Alves, A. Cavaleiro, G. Ph, E. L. Bourhis, J.P. Riviere, J.F. Pierson, O. Banakh, Journal of Applied Physics 98 (2005) 023715.

[37] D. Depla, J. Haemers, R. DeGryse, Thin Solid Films (2006) 468–471.

Chapter IV

Composition and Structural characterization

4.1. Introduction

Ion implantation has been extensively used to obtain a wide variation in near-surface microstructure and properties. Using MeV ions it has become possible to make structures of interest such as buried conducting layers [1] and very large scale integration (VLSI) deep wells. The damage produced during MeV ion implantation can be used to reduce minority carrier life time in Si and to provide buried gettering sites for collection of metallic impurities. Energetic ions induce damage in the silicon and at higher fluences, a phase transformation from crystalline Si (c-Si) to amorphous Si (a-Si) can occur. Damage induced by ion irradiation in Si depends on fluence, flux, energy of the ion, mass of the ion, target temperature, tilt angle of the target, etc. Understanding the amorphization process is still an active area of research and various mechanisms have been put forward [1]. As it is well known, RBS is an ion beam analysis technique based on the elastic collision between the incoming particles and target nuclei [2]. From the study of scattered projectiles, atomic composition depth profiles can be obtained for the near surface region of materials, making RBS a powerful nondestructive technique for this purpose.

The term structure is used as a commonly accepted concept in materials engineering, although many systems are more or less nanoscaled in nature. Due to the nature and characteristics of PVD processes, the structural properties of thin films are, in general, strongly dependent of the deposition parameters, such as deposition rate, deposition temperature, gas (working and reactive ones) pressures, impurities, ion bombardment etc [3]. Diffraction effects are observed when electromagnetic radiation impinges on periodic structures with geometrical variations on the length scale of the wavelength of the radiation. The interatomic distances in crystals and molecules amount to 0.15–0.4 nm which correspond in the electromagnetic spectrum with the wavelength of x-rays having photon energies between 3 and 8 keV.

Accordingly, phenomena like constructive and destructive interference should become observable when crystalline and molecular structures are exposed to x-rays [4]. When a crystalline film is irradiated with short wavelength X-rays the crystal planes can satisfy the Bragg diffraction conditions giving a diffraction pattern. This diffraction pattern can be used to determine the crystal plane spacing (and thus the crystal phase), preferential orientation of the crystals in the structure, lattice distortion, and crystallite size [5]. Thin-film XRD is important in many technological applications, because of its abilities to accurately determine

strains and to uniquely identify, the presence and composition of phases. In semiconductor and optical materials applications, XRD is used to measure the strain stare, orientation, and defects in epitaxial thin films, which affect the film's electronic and optical properties.

For magnetic thin films, it is used to identify phases and to determine preferred orientations, since these can determine magnetic properties. In metallurgical applications, it is used to deter-mine strains in surface layers and thin films, which influence their mechanical properties. For packaging materials, XRD can be used to investigate diffusion and phase formation at interfaces [6].

4.2. Characterization techniques

4.2.1. Composition analysis: Rutherford Backscattering (RBS)

The method was first employed by nuclear physicists to analyze their targets in 1951. Extensive application to material science began in the late1960s. The technique has been refined and now constitutes one of the most common methods for compositional analysis of the surface region [7].

This popular thin-film characterization technique relies on the use of very high energy (MeV) beams of low mass ions. These have the property of penetrating thousands of angstroms or even microns deep into films or film- substrate combinations. Interestingly, such beams cause negligible sputtering of surface atoms. Rather, the projectile ions lose their energy through electronic excitation and ionization of target atoms. These "electronic collisions" are so numerous that the energy loss can be considered to be continuous with depth. Sometimes the fast-moving light ions (usually $^{4}He^{+}$) penetrate the atomic electron cloud shield and undergo close-impact collisions with the nuclei of the much heavier stationary target atoms.

The analysis of the surface and near-surface region of solids has become an important field of science and technology. RBS is one of the most powerful methods among a number of analyzing techniques. In RBS, high-energy ion beams, usually H or He ions with energies in the range 1–4 MeV, are used as probes. A sample is irradiated by the ion beam. Almost all ions penetrate deep inside the sample up to ca. 10 µm until they entirely lose their kinetic energy. During the penetration some ions collide with the target atoms and are subject to elastic Coulomb scattering (Rutherford scattering) between the projectile and the target nuclei and maybe backscattered from the sample. The energy of the ion backscattered from the target

atom depends on the target atom mass. This allows compositional analysis of a surface region of several micrometers by measuring the energy spectrum of the backscattered ions.

Figure 4.1 illustrates a schematic set-up of RBS and an example of an energy spectrum for a two-element thin film on a low mass substrate. The ions scattered from each element form a separated peak. The number of target atoms in the film can be derived from the peak yields and the peak width gives the film thickness [8].

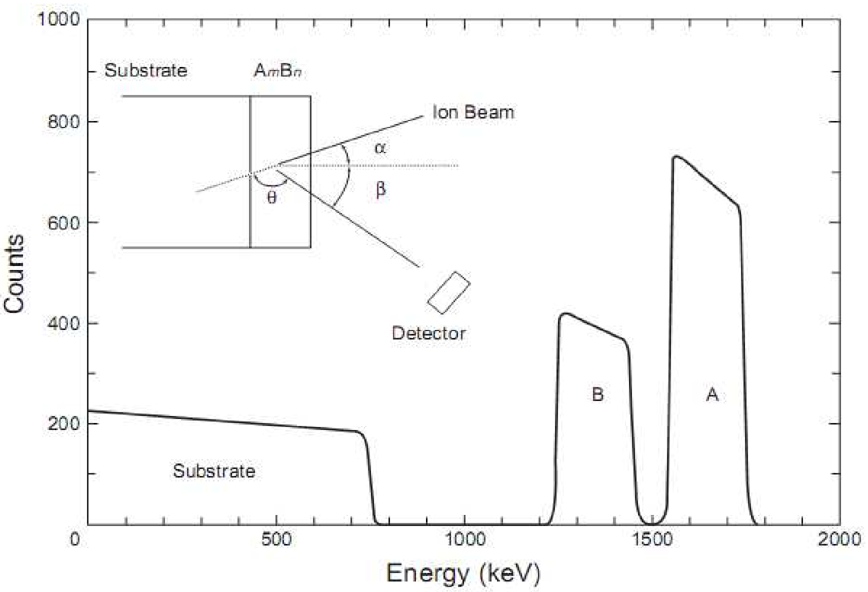

Fig. 4.1. *RBS spectrum for a two element compound film ($A_m B_n$) on a low mass substrate. The inset shows the schematic set-up of RBS*

The resulting scattering from the Coulomb repulsion between ion and nucleus has been long known in nuclear physics as Rutherford scattering. The primary reason that this phenomenon has been so successfully capitalized upon for film analysis is that classical two-body elastic scattering is operative. This, perhaps, makes RBS the easiest of the analytical techniques to understand.

At a basic level, RBS demonstrates the electrostatic repulsion between high energy incident ions and target nuclei. The specimen under study is bombarded with monoenergetic beam of $^4He^+$ particles and the backscattered particles are detected by the detector analysis system which measures the energies of the particles. During the collision, energy is transferred from the incident particle to the target specimen atoms; the change in energy of the scattered particle depends on the masses of incoming and target atoms. For an incident particle of mass M_1, the energy is E_0 while the mass of the target atom is M_2.

After the collision, the residual energy E of the particle scattered at angle Ø can be expressed as:

$$E = k^2 E_0 \qquad \text{(eq.4.1)}$$

$$k = \frac{(M_1 cos\theta + \sqrt{M_2^2 - M_1^2 \sin^2\theta}}{M_1 + M_2} \qquad \text{(eq.4.2)}$$

where k is the kinematic scattering factor, which is actually the energy ratio of the particle before and after the collision. Since k depends on the masses of the incident particle and target atom and the scattering angle, the energy of the scattered particle is also determined by these three parameters.

For a particular combination of M, m_r, and θ the equation 2 allows to correlate the energy of the incident ion before and after to interaction with the target atom.

$$E_i = K_i * E_0 \qquad \text{(eq.4.3)}$$

K_i is known as the kinematic factor and can be calculated from equation 4.3.

Once the incident ion mass, energy and angular position of the ion detector are selected, K_i just depends on the atomic weight of the target atom. The majorities of the incident ions penetrates below the film surface and are continuously losing energy at a linear rate with distance traversed, but the scattered ion energy is still given by equation 4.3 only the E_0 is now the ion incident energy at that point in the matrix. The backscattered ions that collide with the detector generate an impulse that is proportional to the energy of the detected particles allowing the determination of their energy.

Measuring the E_i allows the determination of the mass of the target atmos. In the course of passage through the target material, the ion beam can be thought of as splitting into two separate chemical elements, each spanning a different range of energies. For each broad elemental peak detected, the highest and lowest energies correspond to atoms on the front and back film surfaces, respectively. Therefore, by measuring the number and energy of backscattered ions, information about the nature of the elements present, their concentration, and their depth distribution can all be simultaneously acquired [9]. A simplified layout of backscattering experiment is shown in Fig.4.2.

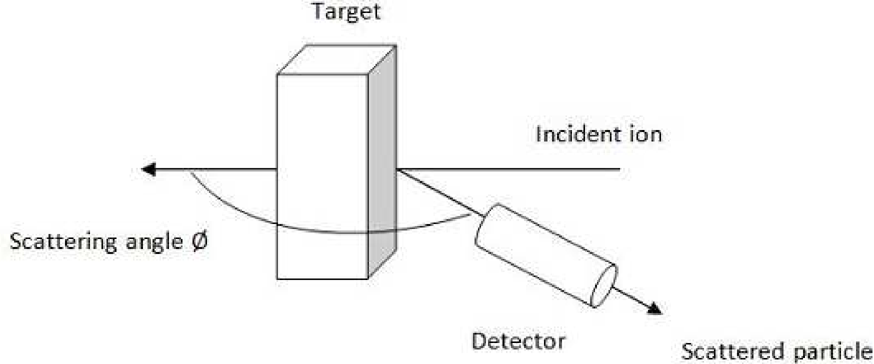

Fig. 4.2. *Schematic representation of the experimental setup for Rutherford backscattering analysis*

In the standard RBS, 1–4 MeV He ion beams and a SSB detector are commonly used. Although both the mass and depth resolutions are poorer for H ions than for He ions, H ions are sometimes used in RBS in order to analyze deeper regions. Ions generated by an ion source are accelerated by an electric field. The most widely used devices for the production of a megaelectronvolt ion beam are the Van de Graaff- type and Cockcroft and Walton type accelerators. The accelerated ions are analyzed by a magnet to eliminate contamination species and to select the ion energy. The calibration of the analyzing magnet is usually done using resonant nuclear reactions. After passing the analyzing magnet, the ion beam is collimated by apertures to a size of ca.1 mm and introduced to a scattering chamber where targets are mounted on a manipulator. The beam current is usually monitored by target current or a beam monitor system installed between the final aperture and the target. The typical beam current is of the order of 10 nA. For a channeling measurement, the beam divergence angle and the precision of the manipulator should be less than 1mrad [7].

4.2.2. Characterization Techniques - X-ray diffraction (XRD)

X-rays were discovered in 1895 by the German physicist Wilhelm Conrad Röntgen. Currently, already well-known and studied, this radiation, which consists of electromagnetic waves of wavelength ranging between 0.1 and 10 Å, it is produced when fast electrons collide with a metallic target [10]. X-ray Diffraction (XRD) is a powerful technique used to uniquely identify the crystalline phases present in materials and to measure the structural properties (strain state, grain size, epitaxy, phase composition, preferred orientation, and defect structure) of these phases. XRD is also used to determine the thickness of thin films and

multilayers, and atomic arrangements in amorphous materials (including polymers) and at interfaces [11].

An integral part of the process of crystal structure determination is an experiment and the techniques used to collect the experimental data. The experiment consists of scattering radiation from crystalline matter, the radiations that are usually employed being x-rays, electrons and neutrons. Although all three radiations can be employed, the vast majority of structure determinations are based on x-ray diffraction data [12.].

Diffraction occurs when a wave encounters a series of regularly spaced obstacles that are capable of scattering the wave, and have spacings that are comparable in magnitude to the wavelength. Furthermore, diffraction is a consequence of specific phase relationships that are established between two or more waves that have been scattered by the obstacles [13].

Bragg`s law

X-rays are a form of electromagnetic radiation that have high energies and short wavelengths—wavelengths on the order of the atomic spacings for solids. When a beam of x-rays impinges on a solid material, a portion of this beam will be scattered in all directions by the electrons associated with each atom or ion that lies within the beam's path [14].

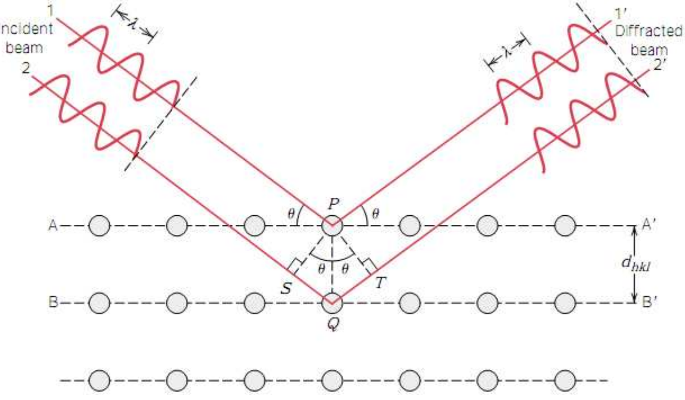

Fig. 4.3. *Bragg's diffraction condition for a reflection of x-rays in two planes of atoms in a solid*

For constructive interference between two waves, a certain geometric configuration is needed. X-rays 1 and 2 are reflected by the atoms P and Q (Fig. 4.3) and the path difference between them will be:

$$QS + QT = 2d\sin\theta \qquad \text{(eq.4.4)}$$

The high degree of order and periodicity in a crystal can be envisioned by selecting sets of crystallographic lattice planes that are occupied by the atoms comprising the crystal. The planes are all parallel to each other and intersect the axes of the crystallographic unit cell. Any set of lattice planes can be indexed by an integer triple hkl with the meaning that a/h, a/k and a/l now specify the points of intersection of the lattice planes with the unit cell edges. This system of geometrical ordering of atoms on crystallographic planes is well known to be indicated by the so-called Miller indices hkl. As an example, the lattice planes with Miller indices (110) and (111) are displayed in fig. 4.4 for the simple cubic lattice.

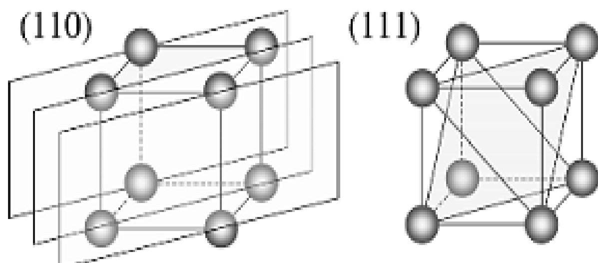

Fig. 4.4. *Lattice planes with Miller indices (110) and (111) in a simple cubic lattice*

The distance between two adjacent planes is given by the interplanar spacing d_{hkl} with the indices specifying the Miller indices of the appropriate lattice planes. For cubic lattices it is found by simple geometric consideration that the interplanar spacing depends on the unit cell parameter *a* and the Miller indices according to [4]:

$$d_{hkl} = \frac{a}{\sqrt{h^2+k^2+l^2}} \qquad \text{(eq.4.5)}$$

For a set of crystalline plans with Miller indices (hkl), the condition for constructive interference to be observed is the transposition in Bragg's law (eq.4.3) [15] which relate between the wavelength of X-radiation (λ), the angle between the incident beam, the plane responsible for Bragg diffraction (θ) and the distance between crystal planes (d_{hkl}):

$$2d_{hkl}\sin\theta = n\lambda \qquad \text{(eq.4.6)}$$

n represents the diffraction order.

The variation of the angle of the beam on the sample allows the detection of the peaks that correspond to the crystal planes in the sample.

Bragg-Brentano geometry

The basic measurement geometry of by far the most frequently used x-ray diffraction instrument is depicted in Fig.4.5. The angle of both the incoming and the exiting beam is θ with respect to the specimen surface. Its measurement geometry may also be applied to the investigation of thin films, especially if the layer is polycrystalline and has been deposited on a flat substrate, as is often the case [4].

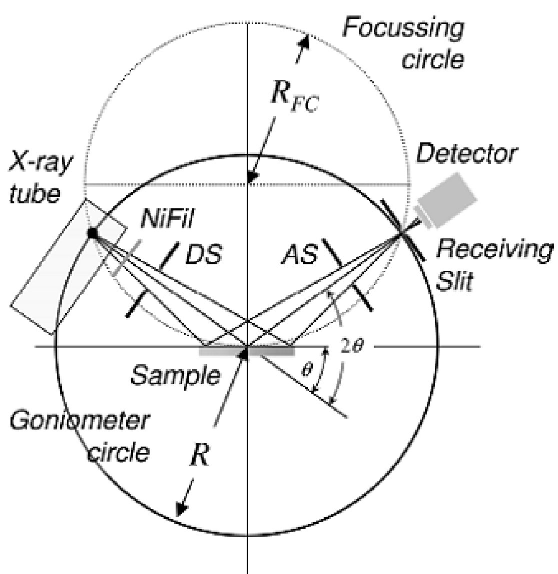

Fig 4.5. *Schematic representation of θ/2θ diffraction in Bragg–Brentano geometry*

After passing through receiving slits, the diffracted X-rays are detected. The specimen is rotated at one- half the angular velocity of the detector. Since the incident and diffracted X rays make the same angle to the specimen surface, structural information is obtained only about (hkl) planes parallel to this surface [16].

Glancing Incidence X-ray Diffraction (GIXD)

For ultrathin epitaxial films (less than - 100 Å), Grazing Incidence X-ray Diffraction (GIXD) is the preferred method and has been used to characterize monolayer films. Here the incidence angle is small (-0.5°) and the X rays penetrate only - 100- 200 Å, into the specimen.

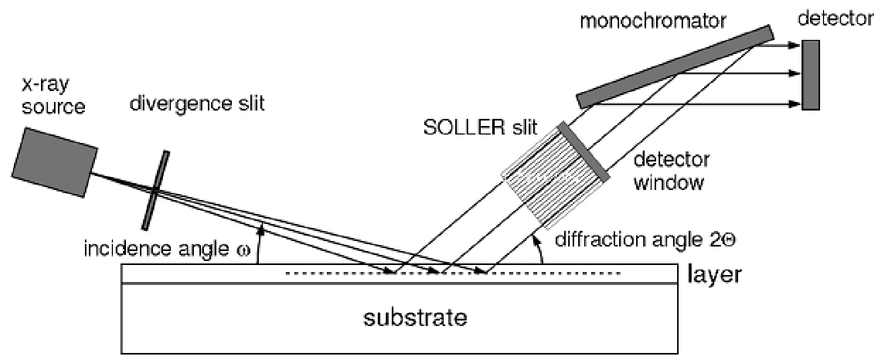

Fig. 4.6. *Schematic diagram of grazing incidence X-ray diffractometry (GIXRD), 2θ Bragg angle, ω angle of incidence*

The exit angle of the diffracted X rays is also small and structural information is obtained about (hkl) planes perpendicular to the specimen surface [15]. GIXRD can therefore be used for the extreme situation of surface structure, or epitaxial relationships at the interfaces of films, where atomic positions can be determined to an accuracy of 0.001 Å in favorable cases [8].

4.3. Results and discussion

4.3.1 Chromium oxynitride

Composition of the films

The atomic composition of the as-deposited samples was measured by Rutherford Backscattering Spectroscopy (RBS) using (1.4, 1.75) MeV and 2 MeV for the proton and ^{4}He beams, respectively. The scattering angles were 140º (standard detector, IBM geometry) and 180º (annular detector), tilt angles 0º and 25º. Composition profiles for the as-deposited samples were generated using software NDF [17]. For the ^{14}N, ^{16}O and ^{28}Si data, the cross-sections given by Ramos et al. were used [18]. The analyzed area was about 0.5×0.5 mm^{2}.

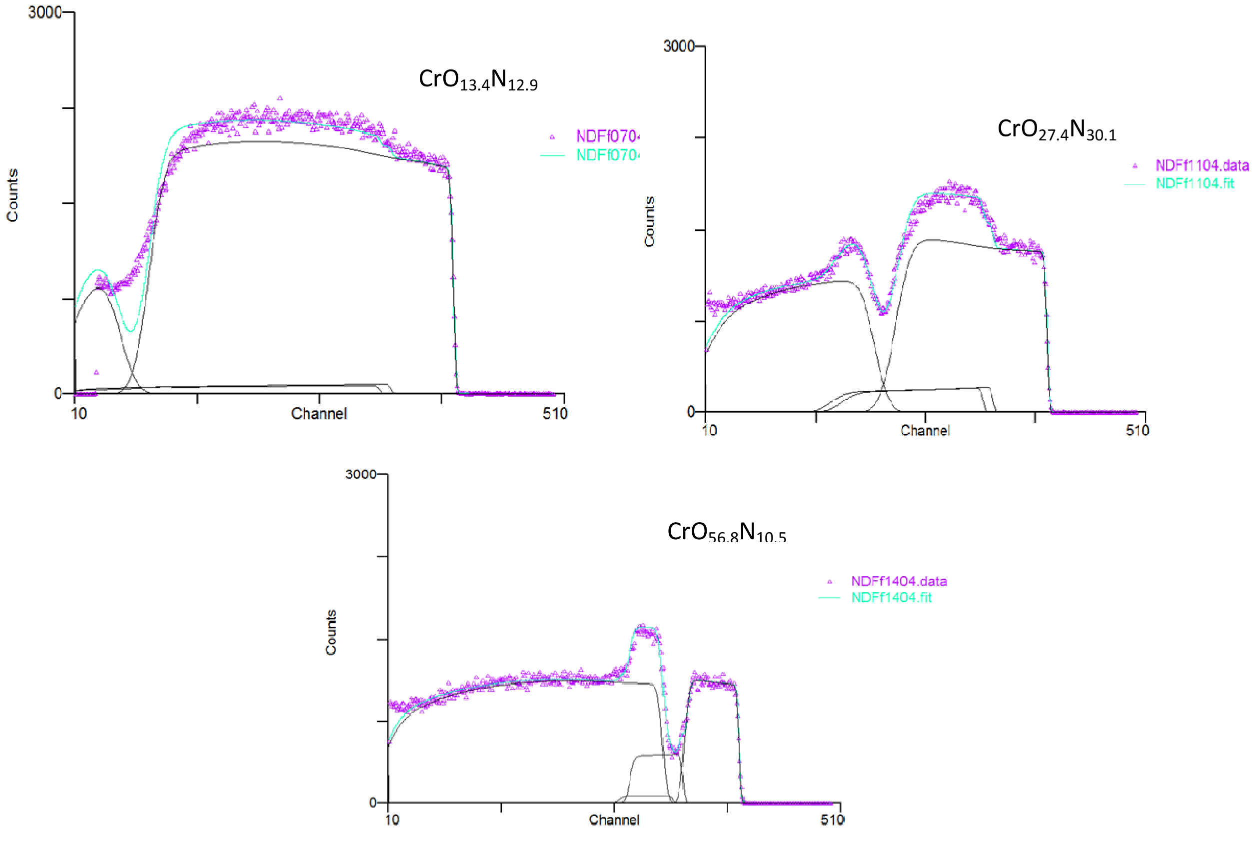

Fig. 4.7. *RBS spectra obtained for the measurements of the series of samples prepared with different reactive gas flows*

As a summary, figure 4.7 shows the obtained RBS spectra and simulations of the representative samples prepared with different reactive gas flows from the three different zones. The first important fact that should be mentioned is that the results from the RBS simulations revealed an almost homogenous in depth composition profiles.

Following the previous analysis, the samples in fig 8 can be divided in the same three zones, which actually correspond to important variations of the composition.

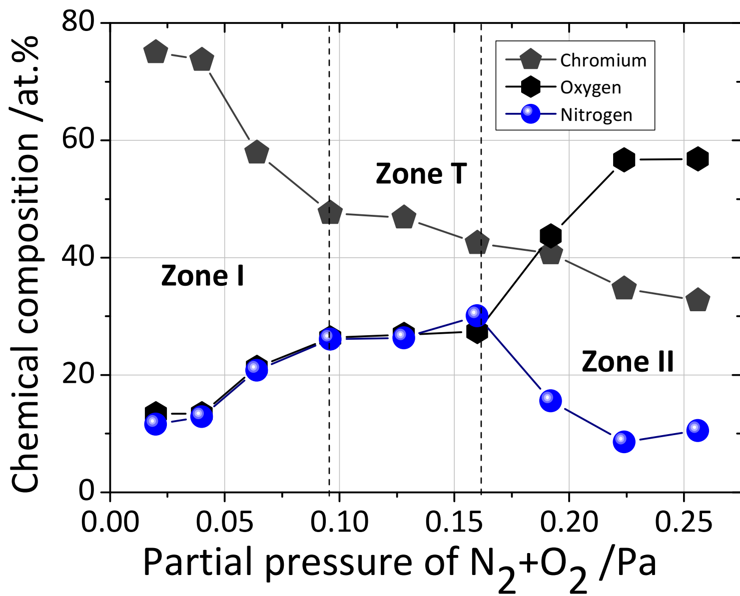

Fig. 4.8. *Evolution of the chemical composition as a function of the partial pressure of reactive gas (N_2+O_2). The pressure was measured prior to discharge ignition. The chemical composition of all samples was determined within an error of about 3-5 at. %*

For the films in Zone I, prepared with low partial pressure of reactive gas mixture ($p_{N2+O2} \leq 0.1$ Pa), the concentration of chromium decreases suddenly from 75 at. % to a value close to 58 at. %, thus confirming the high sub-stoichiometric condition of these samples and their metallic nature, as in fact anticipated by their visual inspection. The concentration of oxygen and nitrogen presents quite similar behaviours in this first zone, with the oxygen varying from about 13 to 21 at. %., and the nitrogen from around 11 to 21 at. %. For films prepared within zone T, the chromium content reveals a slight decrease from around 47 to a value close to 45 at. %. Oxygen and nitrogen contents are approximately constant and with a quite similar value within this zone, at about 30 at. %.

Regarding the samples prepared with the highest gas mixture partial pressures (between 0.16 to 0.25 Pa), zone II, the composition analysis, Fig. 4.8, reveals again the decrease of the chromium content from around 40 to a value close to 32 at.%. The RBS analysis shows for this zone a slightly decrease of the nitrogen content from to around 8 at. % and a significant increase of the oxygen content from 43 at.% to a value close to 56 at.%.

Beyond these absolute values of composition and their variations, it is particularly important to notice the evolution of the atomic ratios of the different elements as shown in

Fig. 4.9, which may give the first indication about the particular tendency for compound formation.

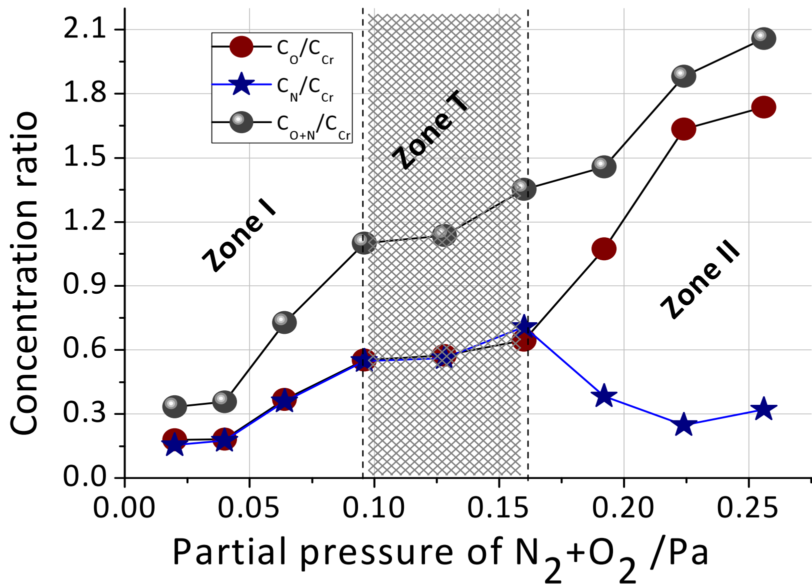

Fig. 4.9. *Evolution of the concentration ratio as a function of the partial pressure of reactive gas (N_2+O_2). The pressure was measured prior to discharge ignition. The chemical composition of all samples was determined within an error of about 3-5 at. %*

Within zone I, results show that all non-metals to chromium atomic ratios (C_O/C_{Cr}, C_N/C_{Cr} and C_{O+N}/C_{Cr}) have values below one, indicative of the sub-stochiometric nature of the films, forming a kind of metastable solid solution of $Cr(N,O)_x$.

Within the transition zone, the C_O/C_{Cr} and C_N/C_{Cr} ratios are approximately constant, with values close to 0.6, while the C_{O+N}/C_{Cr} ratio is higher than 1, characteristic of an over-stoichiometric compound. On the other hand, the fact that the C_{O+N}/C_{Cr} ratio in this zone is still below 1.5 (the value that would correspond to the Cr_2O_3 compound), would mean, in a first approximation, that there is not enough oxygen (even if together with N) to form oxide-like compounds (N-doped if this element could occupy some of the O positions within the a $Cr_2(O,N)_3$-type compound), but at the same time also too high to form a oxygen-doped nitride-like phase. This may induced the possibility to have over-stoichiometric Cr (O,N)-type compound in this transition zone.

Finally, the films from zone II show an increase of the C_O/C_{Cr} and the C_{O+N}/C_{Cr} ratios to values around 1.7 and 2, respectively, with the C_N/C_{Cr} ratio decreasing to a value close to 0.3. This set of results can be explained by the higher binding enthalpy of chromium oxide (-564

kJ/mol per chromium atom) compared to chromium nitride (-125 kJ/mol), favouring thus the bonding of Cr atoms with oxygen [19]. The films from this zone are likely to be oxide-based Cr_2O_3 or CrO_2 compounds, with the excess of nitrogen probably being incorporated in lattice or in interstitial positions within the oxide phase [20-21].

Structure analysis of prepared films

The crystallographic structure was investigated by X-ray diffraction (XRD), using a Philips PW 1710 diffractometer (Cu-Kα radiation) operating in a Bragg- Brentano configuration. XRD patterns were deconvoluted, assuming to be Pearson VII functions to yield the peak position, peak intensity and integral breadth [22].

Fig. 4.10 shows a summary of the different structural features revealed by the overall set of prepared samples. In fact, and following both the deposition characteristics (target potential end deposition rate) and composition analysis, the structural characterization revealed the development of three major types of crystalline structures, represented by each of the diffractograms depicted in Fig. 4.10.

Thus, the set of samples that were prepared within the metallic-like zone, zone I, represented in Fig. 4.10 by the sample prepared with the highest C_{O+N}/C_{Cr} ratio within this zone ($CrN_{0.36}$ $O_{0.37}$), showed the development of a very poorly crystallized structure (quasi-crystalline), where the position of the different diffraction patterns suggest that it may be similar to a fcc CrN-type one. It is worth mentioning, that a hcp Cr-type phase may also be present, as evidenced by the large and broad peak at around $2\Theta = 44°$, as well as the peak tail at $2\Theta \approx 65°$, meaning that the samples in this zone probably consist of a mixture of both CrN(O) and Cr(O) phases. The (O) representation is inserted here to take into account the non-neglecting possibility that it may be incorporated in both structures [20-21].

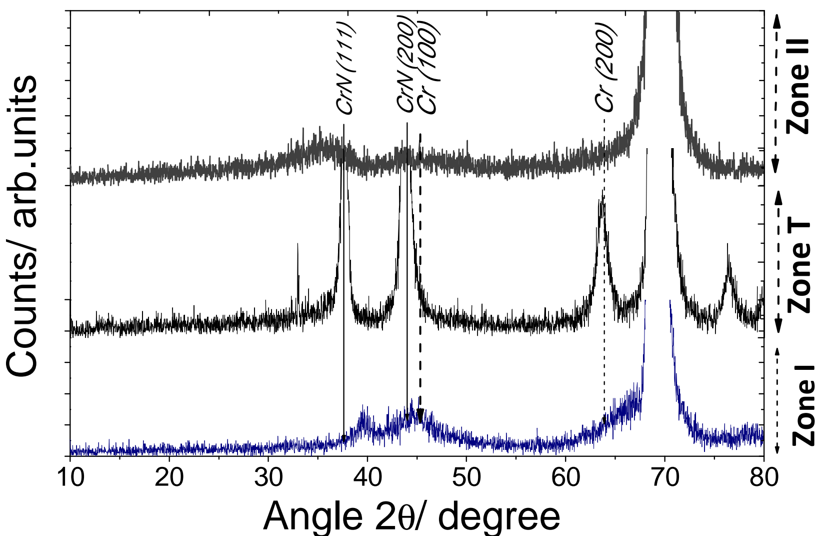

Fig. 4.10. *X-ray diffraction patterns for representative samples of each of the three identified zones with different crystallographic features.*

Notice also the relatively high shift in the peak positions for the CrN(O) phase, which can be easily understood taking into account the sub-stoichiometric condition of the samples in this zone (C_O/C_{Cr} and C_N/C_{Cr} below 0.4 and C_{O+N}/C_{Cr} ratio below 0.7), and the fact that oxygen being very reactive, may be occupying nitrogen positions in the CrN lattice (as mentioned above), thus inducing significant lattice distortions.

Regarding the samples that were indexed to zone T, Fig. 4.10 clearly shows that a CrN-type structure is present, with relatively high crystallinity, as demonstrated by the XRD pattern of the $CrN_{0.71}\,O_{0.65}$ sample. The two diffraction peaks observed correspond to (111) and (200) planes of that fcc CrN(O)-type structure, with a (111) preferential growth. As already anticipated by the composition analysis, no oxide phase is observed, which may be easily understood by the insufficient oxygen content in the films to form such a Cr_2O_3 phase. Important also to note is the much higher crystallinity of this zone T samples when compared to the results obtained for the zone I samples. Furthermore, it is also to note the significantly less shift in the peaks position, again if compared to those of zone I.

The main reason for such behaviour is certainly associated with the particular stoichiometry of the samples within this zone. As demonstrated by Fig. 4.10, the samples prepared within zone T have C_O/C_{Cr} and C_N/C_{Cr} ratios close to 0.6, while the C_{O+N}/C_{Cr} ratio is varies between about 1 and 1.3. Taking into account the possibility to have O occupying N

positions within the fcc CrN lattice (quite probable due to the low C_N/C_{Cr} ratio), this would lead to an increasing stoichiometric-condition of the crystalline phase and thus to a continuous approach towards the CrN peak positions.

Finally, the samples prepared within zone II develop an amorphous-type structure, as shown in the diffractogram of the sample with composition $CrN_{0.25}O_{1.64}$. Beyond the composition analysis, Fig. 4.8, which induced an oxide-like nature of the films prepared within this zone II, their structural features are clearly different from the two previous zones, where the amorphous type structure may correspond to an oxide-like phase, as demonstrated by R. Mientus et al. [19].

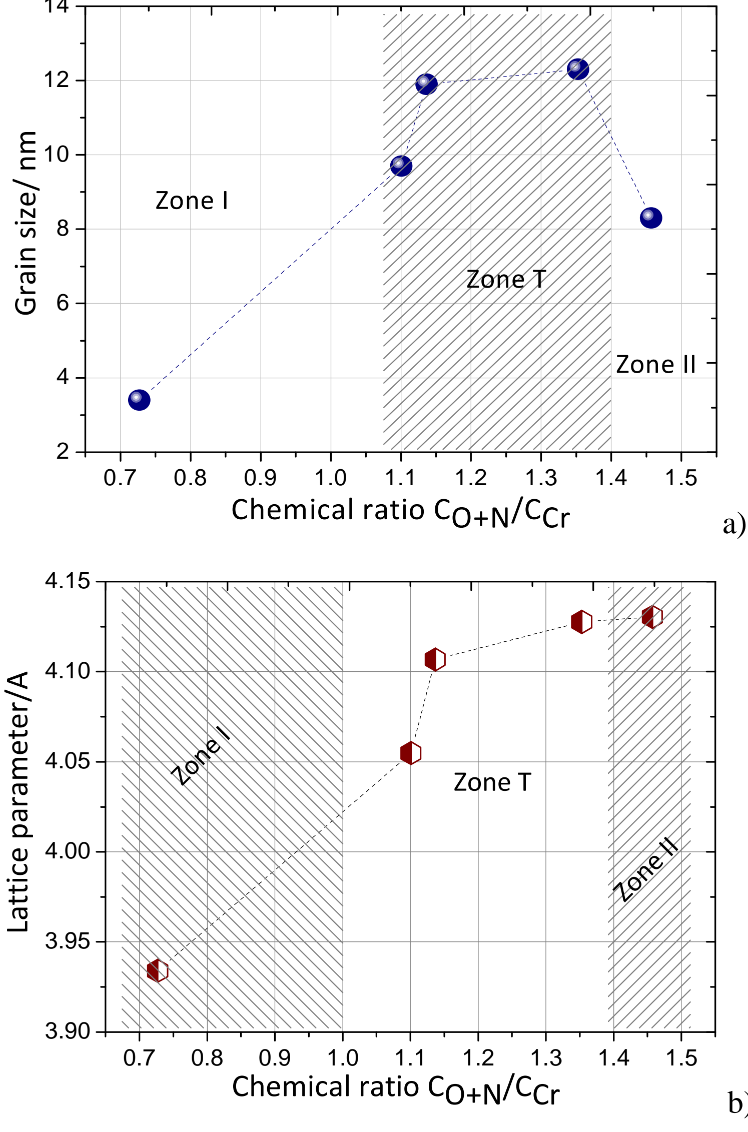

Fig. 4.11. *Grain size (**a**) and lattice parameter (**b**) of the crystals as a function of the concentration ratio*

Taking in too account the structural transitions grain size and lattice parameter (determined by using the integral breadth method) were carry out as a function of the non-metallic/metallic ratio (Fig. 4.11a). The results are showing an increase of the grain size from ~3.5 to 12.5 nm with the increase of concentration ratio ($0.7 < C_{O+N}/C_{Cr} < 1.3$) that is given by the improvement on the crystallinity of the films from zone T. Zone II with a concentration ratio, C_{O+N}/C_{Cr} between 1.3 to 2.0 presents a decrease of the grain size revealing the tendency of the films to become amorphous with an increase of the oxygen content which is an important factor for the changes occurring in the structure of the films. This behaviour can be explained by a deformation energy dominant process that is mainly due to the oxygen incorporation in the CrN lattice and thus the creation of inherent structural defects [27].

Fig. 4.11b presents the lattice parameter as a function of the concentration ratio C_{O+N}/C_{Cr}. The increase of the lattice parameter presented in the plot can be described by the insertion of nitrogen and oxygen in interstitial positions. Another factor that can have an impact over the increase on the lattice parameter is the compressive residual stress state in which the films may be. This factor is revealed by the lattice parameters of the CrN coating in zone T (a=4.05Å) that are lower than the reference value of this material (a_{CrN}= 4.149Å) that might be turn by the structural defects or doping of the oxygen.

4.3.2. Aluminium oxynitride

Composition of the films

Fig. 4.12 (a - b) shows the chemical composition (at.%) and the concentration ratios of non-metallic/metallic elements of the films as a function of the partial pressure of the reactive gas mixture.

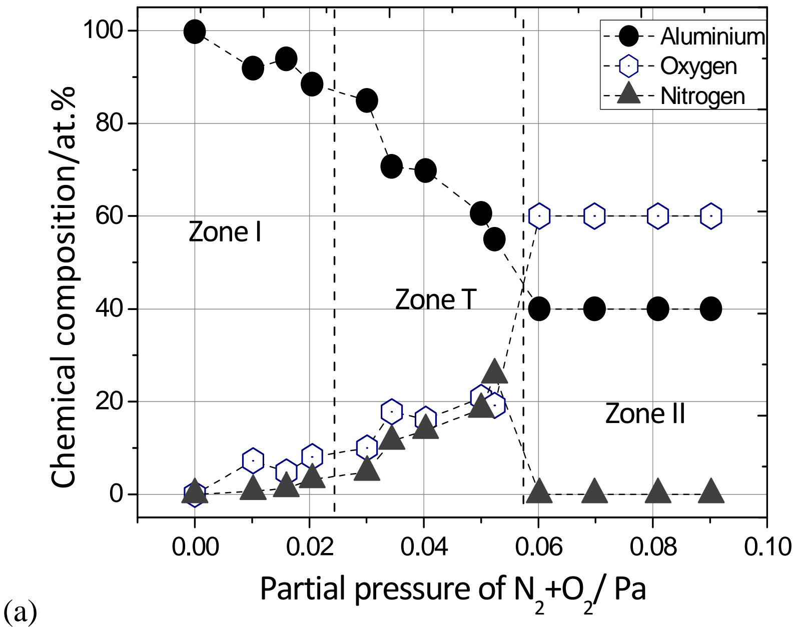

(a)

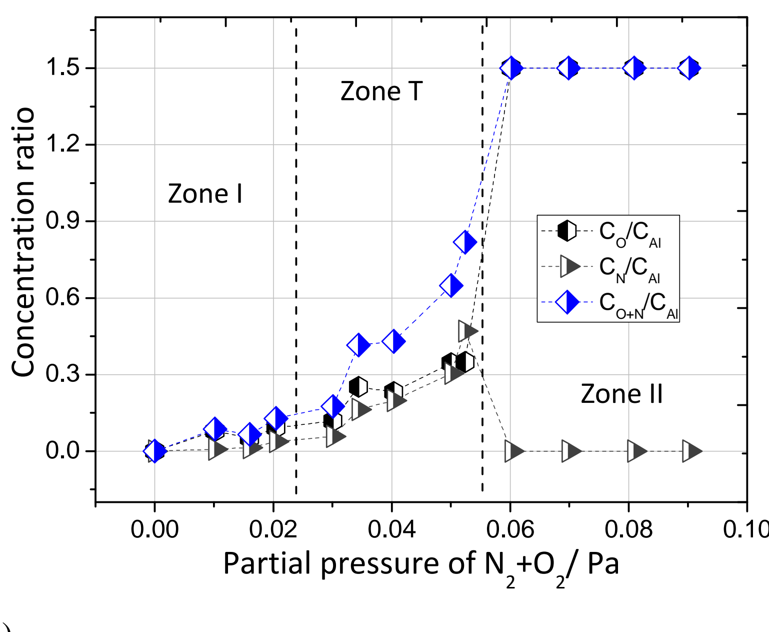

(b)

Fig. 4.12 *Evolution of the* ***(a)*** *chemical composition and* ***(b)*** *concentration ratio, as a function of the partial pressure of reactive gas (N_2 +O_2). The pressure was measured prior to discharge ignition. The chemical composition of all samples was determined within an error of about 3-5at.%*

For films belonging to zone I, prepared with low partial pressures of the reactive gas mixture ($p_{N2+O2} \leq 0.02$Pa), the concentration of aluminium decreases slightly with the increase of the reactive gas pressure, from 100 at.% pure Al concentration to a value close to 90 at.%. The concentration at.% of oxygen and nitrogen increased slightly for these films, with the oxygen varying from 0 to 8 at.% ($0< C_O/C_{Al} <0.09$); and the nitrogen from 0 to 3 at.% ($0< C_N/C_{Al} <0.04$), as shown in Fig. 4.12 (a and b). The films in this zone have a characteristic metallic color, as a result of the high aluminium content and the small incorporation of nitrogen and oxygen in the films. The films within this first zone will be noted here after as belonging to a metallic-like zone.

Regarding the samples that were prepared with the highest gas mixture partial pressures ($p_{N2+O2} \geq 0.06$Pa), zone II, the RBS analysis revealed that all films have very similar compositions, with an aluminium content around 40 at.% and an oxygen amount close to 60 at.%. The nitrogen concentration drops to a residual value non-detectable within the resolution of the experimental setup, meaning that its amount should be below 3-5 at.%. This set of results induces a roughly stoichiometric composition of the films in the form of Al_2O_3 (alumina) films. This is to be expected since the lower sputter yield of the poisoned target reduces significantly the amount of aluminium that arrive to the substrate and it is completely consumed due to high density of reactive gas in the plasma.

The higher affinity of oxygen to bond aluminium compared to nitrogen, explains this non-incorporation of nitrogen in the films. In accordance with this oxide-like concentration, the films have interference-like colorations, consistent with their semi-transparency. The films within this second zone will be thus noted here after as belonging to a compound-like zone. Between these two main zones, a transition region was already identified (zoneT), corresponding to the films that were prepared with reactive gas partial pressures between 0.03 and 0.05 Pa.

Within this transition zone, the incorporation of aluminium decreases more sharply than in zone I, varying from 85 to 55 at.%. In these films the incorporation of nitrogen and oxygen becomes more important, as can be observed from the sharp increase of the C_{O+N}/C_{Al} ratio up to 0.81, with the oxygen concentration rising from 10 to 20 at.% ($0.12\leq C_O/C_{Al} \leq 0.34$) and the nitrogen content also increasing, from 5 to 25 at.% ($0.06\leq C_N/C_{Al} \leq 0.47$). The films in this transition zone have dark grey opaque-like surface tones, which is most likely the result of their decreasing metallic content.

Structure analysis of prepared films

Fig. 4.13 shows X-ray diffraction diagrams of representative AlN_xO_y films, prepared within the frame of the present work.

Given the three different zones of films identified previously, the obtained results revealed crystalline-like thin films within zones I and T, and amorphous-type ones for the case of the films prepared within zone II.

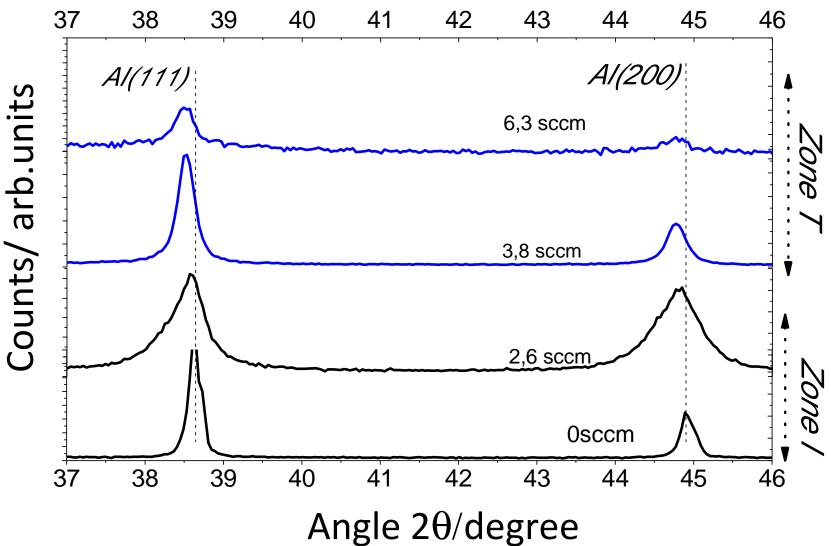

Fig. 4.13. *X-ray diffraction patterns for representative samples for metallic-like and transition zone*

The coating deposited without reactive gas ("pure" aluminium thin film) exhibits, as expected, a face-centered cubic (fcc) structure, characteristic of aluminium [23]. The two diffraction peaks represented in Fig. 4.13 correspond to (111) and (200) planes of such fcc structure, with a clear (111) preferential growth. A second important note is that in spite of the differences in the composition of the films within zones I and T, the structure is maintained, although the peak intensity is gradually decreasing with increasing pressure of reactive gas. This means that the films are becoming less crystalline, ending up as completely amorphous or the highest partial pressures ($p_{N2+O2} \geq 0.06$Pa), zone II.

Furthermore, with increasing reactive gas partial pressures, the diffraction peaks also are shifting to lower diffraction angles, corresponding to higher lattice parameters, which could be a sign of the presence of some nitrogen and oxygen in interstitial positions or even substituting metallic atoms in the fcc crystalline structure of the aluminium.

This change in the lattice parameter can be observed in Fig. 4.14b, where the values of the lattice parameter and grain size (estimated by XRD peak fitting with a Pearson VII function, using the integral breadth method) are plotted as a function of the concentration ratios of the films.

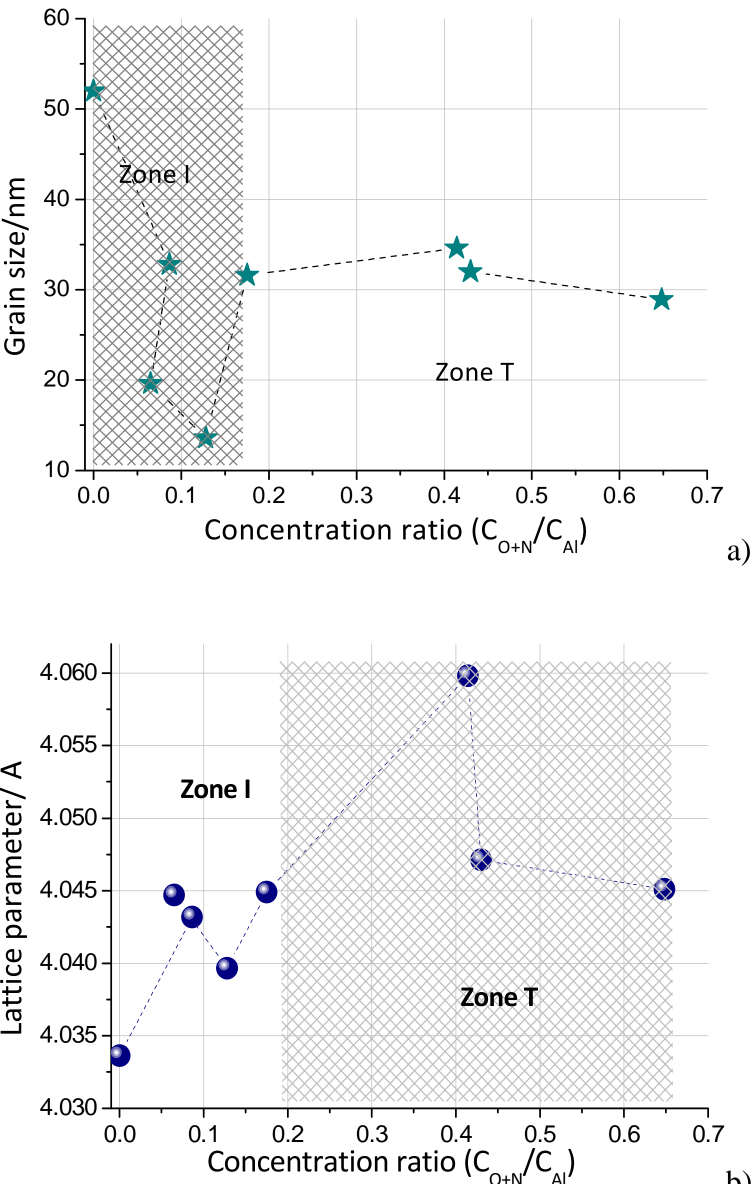

Fig. 4.14. *Grain size* ***(a)*** *and lattice parameter* ***(b)*** *of the crystals as a function of the concentration ratio*

The results show that there is a general tendency for the increase of the lattice parameter as more oxygen and nitrogen is incorporated in the films. Another important fact is that the lattice parameter of the aluminium coating (a =4.034Å for p_{N2+O2}= 0.00Pa) is lower than the reference value of this material found in the available literature [24] (a_{Al}=4.0496nm), which is a typical behavior for the films deposited by magnetron sputtering, indicating that the film is in a compressive residual stress state [25], which by its turn may result from structural defects such as interstitials, vacancies and some residual doping elements such as those of argon and oxygen.

Concerning the film's grain size, the results plotted in Fig.4.14a show that there is a sharp decrease of this property as a function of the non-metallic/metallic ratio (C_{O+N}/C_{Al}) in zone I, from 52 nm (C_{O+N}/C_{Al} =0.00 Pa) to 14 nm (C_{O+N}/C_{Al} =0.13). This decreasing can be explained by the incorporation of oxygen in the films that is segregated to the surface and grain boundaries, which inhibits the grain coarsening during columnar film growth, due to the reduced mobility of aluminium atoms on oxide layers [26].
Interesting to note for the different zones films is the behaviour that can be observed for the grain size evolution within the transition zone. In this zone, no significant variation of the grain size is reported, which assumes a value of about 30 nm. This behavior is consistent with the formation of round shape grains whose growth is completely blocked by a surrounding oxide layer in an early stage of grain formation [26].

4.4. Conclusions

This chapter presents the determination of atomic composition of the deposited samples and the depth profiles of the concentration (in the direction of growth) has been achieved by Rutherford backscattering spectroscopy (RBS), crystallographic structure was investigated by X-ray diffraction (XRD) and XRD patterns were deconvoluted assuming to be Pearson VII functions to yield the peak's position, peak intensity and integral breadth and from here determination of grain size and lattice parameter.

CrN_xO_y system presents a chemical composition were the Cr concentration reveals a continuously decreasing from 75 at.% in zone I to 32 at.% to zone II, while the concentration of nitrogen and oxygen shows a continuous increase in the first and the transition zone, and in

zone II oxygen due to the higher reactivity makes its presence felt increasing to a value of 56 at% compared to nitrogen that decreases considerably.

Besides this, the concentration ratio reveals for zone I a sub-stochiometric nature of films that forms a metastable solid solution of Cr(N,O)x, transition and zone II shows a over-stochiometric nature f the films but where the formed compounds are different as fallows, over-stochiometric compounds such as Cr(O,N) with compounds such as Cr_2O_3, CrO_2, with an excess of nitrogen. This system developed a CrN centered cubic structure with low crystalline for zone I to a CrN(O) structure with relatively high crystallinity in the transition zone and an amorphous type structure with oxide phases in zone II. Concentration and structure lead to determination of grain size that shows an increase for the first zones, from ~ 3.5 to 12.5 nm and a lattice parameter that grows continuously up to ~ 4.05 Å.

In the second system of AlN_xO_y chemical concentration is similar to the one of the first system that shows the reducing of the chromium concentration for zone I and T, reaching stable values in Zone II. The nitrogen concentration fallows a decrease for zone II, and an increase of the oxygen for all the three zones. The concentration ratio revels a sub-stoichiometric nature of films from the first zones and a stoichiometric behaviour of the coatings of Al_2O_3 (alumina) in zone II. .

These concentrations helps to form the structure which in this case the presents a fcc crystalline structure of the aluminium in zone I, with a decrease of the cristallinity during the transition zone and becoming amorphous for the samples from zone II.

Determination of grain size shows a decrease with increasing the non-metallic /metallic and a lattice parameter is characterized by an increase given by the non-metallic /metallic ratio.

References

[1] J. Kamila, B. Satpati, D. K. Goswami, M. Rundhe, B. N. Dev, P. V. Satyam, Nuclear Instruments and Methods in Physics Research B 207 (2003) 291–295.

[2] F.J. Ager, M.A. Respaldiza, J. Botella, J.C. Soares, M.F. da Silva, J.J. Benitez and J.A. Odriozola: Acta. Mater. Vol. 44, No. 2, pp. 6755681, (1996).

[3] B. North, Surf Coat Technol. 106 (1998) 129.

[4] M. Birkholz, Thin Film Analysis by X-Ray Scattering, WILEY-VCH Verlag GmbH & Co. KGaA Publishing, Weinheim, (2006).

[5] Donald M. Mattox, Handbook of physical vapor deposition(PVD) processing, Westwood, New JerseyNoyes publications,(1998).

[6] C.R. Brundle, C.A. Evans, Jr., S. Wilson, Encyclopedia of Materials Characterization, Butterworth-Heinemann-Reed Publishing USA, (1992).

[7] Jiang Lei, Liu Bo, Zhou Zhu-ying, HE Mian-hong, Zhao Guo-qing, In Situ Rutherford Backscattering Spectrometry analysis of films combination with sputter etching, (1999).

[8] Kenji Kimura, Encyclopedia of Analytical Chemistry, John Wiley & Sons Ltd, Chichester, (2000).

[9] P.E. Schmid, M. Sato Sunaga, F. Lévy, J. Vac. Sci. Technol. A 16 (1998) 2870.

[10] I. Petrov, P.B. Barna, L. Hultman, J.E. Greene, J Vac Sci Technol A (5) (21) (2003) 117-28.

[11] P.E. Schmid, M. Sato Sunaga, F. Lévy, J. Vac. Sci. Technol. A 16 (1998) 2870.

[12] David WL Hulkins, X-Ray Diffraction by Disordered and Ordered Systems, Pergamon Press .

[13] Pyotr Ya. Ufimtsev, Fundamentals of the Physical Theory of Diffraction (2007).

[14] W.D. Callister, Jr., Fundamentals of Materials Science and Engineering, Fifth edition, John Wiley & Sons, Inc.(2001).

[15] R. Jenkins, R. L. Snyder, “Introduction to X-ray Powder Diffractometry”, John Wiley & Sons, New York (1996).

[16] http://fds.oup.com/www.oup.com/pdf/13/9780199219667.pdf

[17] N.P. Barradas, C. Jeynes, R.P. Webb: Appl. Phys. Lett. 71 (1997) 291.

[18] A.R. Ramos, A. Paúl, L. Rijniers, M.F. Silva, J.C. Soares: Nucl. Instr. and Meth. B 190 (2002) 95.

[19] R. Mientus, R. Grotschel, K. Ellmer: Surf. Coat. Technol. 200 (2005) 341-345.

[20] P. Carvalho, F. Vaz, L. Rebouta, L. Cunha, C. J. Tavares, C. Moura, E. Alves, A.

Cavaleiro, Ph. Goudeau, E. Le Bourhis, J. P. Rivière, J. F. Pierson, O. Banakh, J. Appl. Phys. 98 (2005), 023715.

[21] P. Carvalho, J. M. Chappé, L. Cunha, S. Lanceros-Méndez, P. Alpuim, F. Vaz, E. Alves, C. Rousselot, J.P. Espinós, and A.R. González-Elipe: J. Appl. Phys. 103 (2008) 104907.

[22] I. Horcas, R. Fernandez, J.M. Gomez-Rodriguez, J. Colchero, J.G. Herrero, A.M. Baro: WSXM: A software for scanning probe microscopy and a tool for nanotechnology, Rev. Sci. Inst. 78 (2007) 013705.

[23] R.T. Downs, K.L. Bartelmehs, G.V. Gibbs, M.B. Boisen, American Mineralogist 78 (1993) 1104–1107.

[24] V.A. Lubarda, Mechanics of Materials 35 (2003) 53–68.

[25] F. Vaz, L. Rebouta, P. Goudeau, J.P. Riviere, E. Schaffer, G. Kleer, M. Bodmann, Thin Solid Films 402 (2002) 195–202.

[26] I. Petrov, P.B .Barna, L. Hultman, J.E. Greene, Journal of Vacuum Science and Technology A: Vacuum Surfaces and Films 21 (2003) S 117–S128.

[27] P. Carvalho, F. Vaz, L. Rebouta, L. Cunha, C.J. Tavares, and C. Moura, Journal of Applied Physics 98, 023715 (2005).

Chapter V

Electrical Characterization

5.1. Introduction

The capability to design novel non equilibrium solid structures using thin film technologies has boosted in recent years the growth and practical use of a wide variety of 3d transition metal (TM) nitrides, oxides, and oxynitrides. This interest has triggered numerous efforts to investigate their electronic structure and consequently their potential for applications. As a consequence of their high electro negativity, nitrogen and oxygen have a strong tendency to attract electrons from neighboring metal atoms, creating strong crystal fields which result in metallic, semiconducting, or insulating behaviors [1].
Several studies have been performed recently on Cr–O–N coatings, to investigate the effect of oxygen on their electronic, structural, morphological and mechanical properties [2].
Depending on its stoichiometry CrN_x shows a metallic-like ($\rho_{CrN} \approx 6.4\times 10^{-4}\ \Omega$ cm, $x\approx 0.93$) or semiconducting behavior ($\rho_{CrN} > 1 \times 10^{-2}\ \Omega$ cm, $x\approx 1.06$) but chromium oxide is a wide-band gap semiconductor ($E_g\approx 4$ eV, $\rho_{Cr2O3} \gg 1\ \Omega$ cm). Combining both materials as chromium oxynitride, promises the possibility to vary the energy band gap and hence the electronic properties in a wide range. Another possible application is the use of chromium oxynitride films as temperature dependent resistors in thermal radiation detectors [3].

Among the group of possible oxynitrides, aluminium oxynitride thin films (AlN_xO_y) may have some interesting applications in different technological fields, due to a wide difference in the two base materials: aluminium nitride (AlN) and aluminium oxide (Al_2O_3).
Aluminium nitride (AlN) is known as being a semiconductor with a large band gap (6.2 eV) [4] in its more stable and common hexagonal (wurtzite) crystalline structure [5]. Beyond this structure, AlN has also two kinds of cubic structures (with two different lattice parameters) and it was considered, a couple of decades ago [6],as one of the best existing thermal conductors, being an important ceramic material used in many applications such as substrate in microelectronic devices [7].

On the other hand, aluminium oxide, or simply alumina (Al_2O_3), is an insulator material which is commonly prepared in the form of polymorphous material, since it can exist in many metastable structures that are divided into two broad categories: a face-centered-cubic (fcc) or a hexagonal close packed (hcp) arrangement of oxygen anions [8]. The particular dielectric properties of alumina allow using it in a large variety of applications, which can vary from microelectronics and optical applications to wear resistant coatings [9],

as protective films for metal reflectors, for dark mirrors, and in metal–oxide–semiconductor devices [10].

For a better understanding of the other characterizations discussed in the previous chapters with the electronic properties of the films, an analysis of the resistivity was carried out. This chapter will allow an establishment of the difference in the electrical behaviour of the films and how it is influenced the film properties. The characterization of the electrical properties will also establish the limits of practical applicability and new areas of application for these thin films.

5.2. Electrical resistivity

Electrical resistivity is a key physical property of all materials. It is often necessary to accurately measure the resistivity of a given material. The electrical resistivity of different materials at room temperature can vary by over 20 orders of magnitude. No single technique or instrument can measure resistivities over this wide range [11]. Electrical resistance (R) is a physics quantity that expresses the "impairment" suffered by charge carriers, subject to the action of an electric field, when crossing from a point to another in a given ``body``, being dependent on the dimensions and type of material for which this body is constituted. Moreover, electrical resistivity (ρ, electrical resistivity) is a quantity that is also related to an impairment suffered by the charge carriers, however, is an intrinsic property of matter, being independent of the size of the body [12].

The electrical resistivity of a material describes how much it resists the flow of electricity. This property does not depend on the physical dimensions of the material. The resistivity of a material can vary greatly at different temperatures. The resistivity of metals usually increases as temperature increases, while the resistivity of semiconductors usually decreases as temperature increases. The resistivity of a material can also depend on the applied magnetic field.

The resistivity of a material ρ is related with a local applied electric field (E) and the resultant current density (J) by the following expression:

$$E \equiv \rho J \qquad \text{(eq.5.1)}$$

where E is the electric field (V/m), J is the current density (A m^{-2}), and ρ is a proportionality coefficient (Ω m). Equation 5.1 is one form of Ohm's law. Note that E and J are vectors, and ρ is, in general, a tensor. This implies that the current does not necessarily flow in the direction of the applied electric field. In the case of isotropic and homogeneous materials, it is assumed that ρ is a scalar [13-14].

In all conductors, semiconductors, and many insulating materials, only electronic conduction exists, and the magnitude of the electrical conductivity is strongly dependent on the number of electrons available to participate in the conduction process. However, not all electrons in every atom will accelerate in the presence of an electric field.

The number of electrons available for electrical conduction in a particular material is related to the arrangement of electron states or levels with respect to energy, and then the manner in which these states are occupied by electrons [15]. At relatively large separation distances, each atom is independent of all the others and will have the atomic energy levels and electron configuration as if isolated. However, as the atoms come within close proximity of one another, electrons are acted upon, or perturbed, by the electrons and nuclei of adjacent atoms. This influence is such that each distinct atomic state may split into a series of closely spaced electron states in the solid,to form what is termed an electron energy band.

Figure 5.1 exhibits the energy band diagrams of three classes of solids: insulators, semiconductors, and conductors. In insulators, the bandgap is relatively large and thermal energy or an applied electric field cannot raise the uppermost electron in the valence band to the conduction band. In metals or conductors, the conduction band is either partially filled or overlaps the valence band such that there is no bandgap and current can readily flow in these materials. In semiconductors, the bandgap is smaller than that of insulators, and thermal energy can excite electrons to the conduction band. The bandgap of a semiconductor decreases with higher temperature. For instance, for silicon, Eg is 1.12 eV at room temperature and 1.17 eV at zero Kelvin [16]

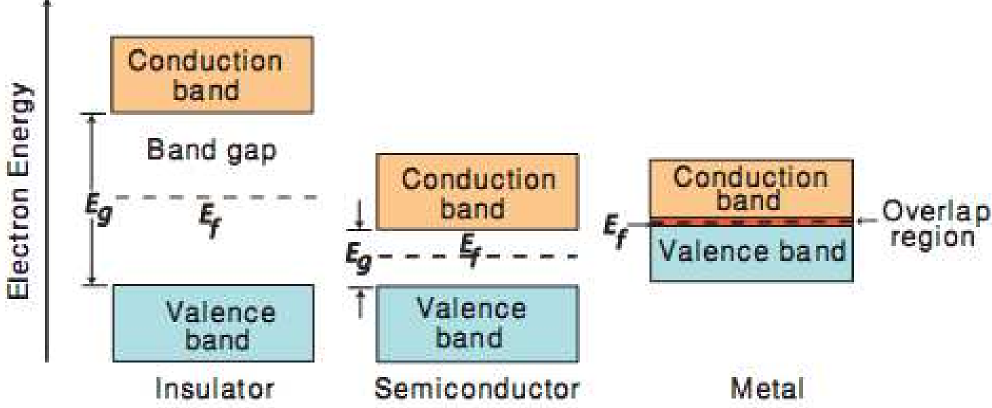

Fig.5.1. *Simplified diagram of the electronic band structure of insulators, semiconductors and conductors (metals). The position of the Fermi level is when the sample is at absolute zero temperature (0 K)*

The Fermi level is an important consequence of band theory, the highest occupied quantum state of electrons at absolute zero temperature. The position of the Fermi level relative to the conduction band is an important parameter that contributes to determine the electrical properties of a particular material. The position of the Fermi level position is also indicated in Figure 5.1. The Fermi energy E_F, also referred to as the Fermi level, is the highest energy occupied state at T = 0K for an electron, and very close to that for T > 0K, which is within about 0.1 eV at room temperature.

As a practical matter E_F represents the highest energy electrons in an equilibrium solid notwithstanding the Fermi tail. Therefore any excitations of electrons imposed, for example, by an external electric field, or even optical excitation, will potentially lift the equilibrium energy levels to higher energies [17].

5.2.1. Conductors

Metals are good conductors because the electrons in these valence bands are not fixed to their atoms. But that is not the only condition for conduction. What makes a metal a conductor is that if you apply an external electric field to it (a potential difference), the electrons will start to accelerate and move. Normally, the probability distribution of k of the electron "cloud" has zero average: (k) =0. If you apply an electric field E, the electrons start moving on average a bit more in the direction of E.

For an electron to become free, it must be excited or promoted in to one of the empty and available energy states above E_f. Thus, very little energy is required to promote electrons into the low-lying empty states. Generally, the energy provided by an electric field is sufficient to excite large numbers of electrons into these conducting states.

Even though these electrons are not locally bound to any particular atom, they, nevertheless, must experience some excitation to become conducting electrons that are truly free.

Thus, although only a fraction is excited, this still gives rise to a relatively large number of free electrons and, consequently, a high conductivity.

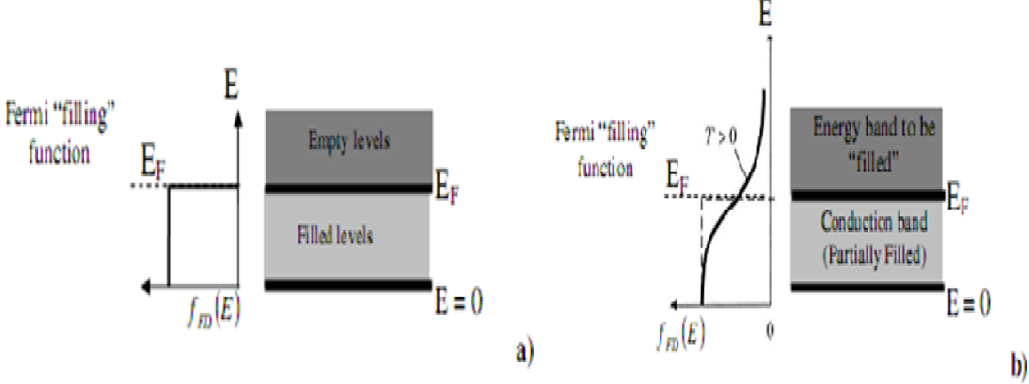

Fig. 5.2. a) *Detail of a half-filled band at T = 0, showing the Fermi-Dirac distribution of the left:* ***b)*** *Band structure of a metal at T > 0, showing the Fermi-Dirac distribution of the left.*

Their resistivity is typically on the order of 10nΩm at room temperature, decreases with decreasing temperature, and in an ideal crystalit would even vanish at T=0. A material is customarily considered metallic if its conductivity exceeds 10^6 $(\Omega m)^{-1}$ (i.e., its resistivity $\rho <$ 1μΩm).

5.2.2. Insulators

Insulators have higher-energy "conduction bands", but they do not energetically overlap with the (filled) valence band. There is a band gap between the valence and conduction bands. If the band gap ΔE is large compared to the temperature of the material, i.e. if $\Delta E \gg kT$, then the chance that an electron gets "accidently" thermally excited to the conduction band is so low that this virtually never happens [semiconductor based]. The most relevant band gap is the one that separates the bands that are filled completely in the ground

state from those that are completely empty. This can occur when the number of electrons per atom is even, and they completely fill one or more bands in the ground state, and the next, empty band is separated by a finite energy gap from the occupied ones. At finite temperatures those states whose energy is larger than the chemical potential can be partially filled by thermally excited electrons, and lower-energy states can be partially empty.

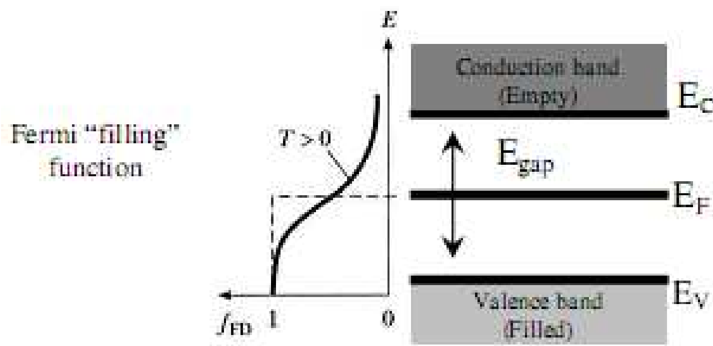

Fig. 5.3. *Band structure in which E_F lies in the gap between bands*

Therefore, strictly speaking, the conductivity does not vanish even when the energy gap exceeds the thermal energy k_BT. A material is considered to be electrically insulating if its conductivity is less than 10^{-8} $(\Omega m)^{-1}$. In general, those materials that are insulators at low temperatures remain insulators at room temperature, too [18].

5.2.3. Semiconductors

Among the materials whose band structure has a finite gap around the chemical potential particular behavior is observed in those for which the energy gap is larger than the thermal energy at room temperature but nonetheless sufficiently small, consequently electrons excited thermally across the gap carry an electric current that can be easily measured and has substantial effects. Such materials are called semiconductors.

However, suppose that some other process excites electrons into the conduction band, for instance the absorption of a photon. We then have a mobile electron that contributes to conductivity. But we also have a positively charged vacancy, called a "hole". The hole can now also move around, as if it is a positively charged particle in itself. If an electric field is applied to the material, the free electrons in the conduction band move in $-\vec{E}$ direction while the holes move in $+\vec{E}$ direction. Both movements contribute to the conduction.

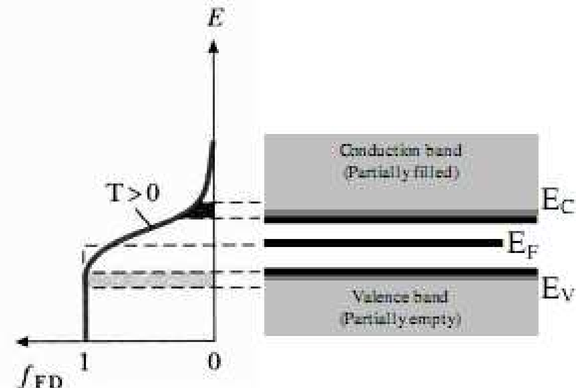

Fig. 5.4. *Band structure of a semiconductor The gap between bands is much smaller than in an insulator, so there is now a small population of the conduction band*

Since all the electrons in the conduction band came originally from the valence band, the number of vacancies in the valence band is exactly equal to the number of electrons in the conduction band. Thus, the values of (E_V - E_F) must be exactly equal to the values (E_C- E_F), and so the Fermi energy must be at midpoint of small energy gap between conduction and valence bands.

The thermal excitation across the energy gap between the valence and the conduction band is relatively probable leading to measurable electrical conductivity. Semiconductors depend more strongly on the temperature regarding the electrical conductivity then conductors and insulators [13, 17, 18].

5.3. Characterization techniques

5.3.1. Four-point probe

The most common way of measuring the resistivity of a semiconductor material is by using a four-point collinear probe. The four-point collinear probe technique of resistivity measurement involves bringing four, equally spaced, electrical conducting pins in contact with the material of unknown resistance. The array is placed in the center of the material.

An in-line four-point probe is used to determine the specimen sheet resistance at each desired measurement location. The number and positioning of measurement locations is determined by end-use needs, or by the parties to the test in the case of referee measurements. At each

location, a direct current is passed into the specimen, using two of the probes, as specified, and the potential difference is measured using the other two probes. Current polarity is reversed and the potential difference is remeasured to allow elimination of thermoelectric effects. Before the probe is raised, the process is repeated using a different combination of probes, as specified. At each location, the sheet resistance is obtained from the four ratios of potential difference to current [20-24].

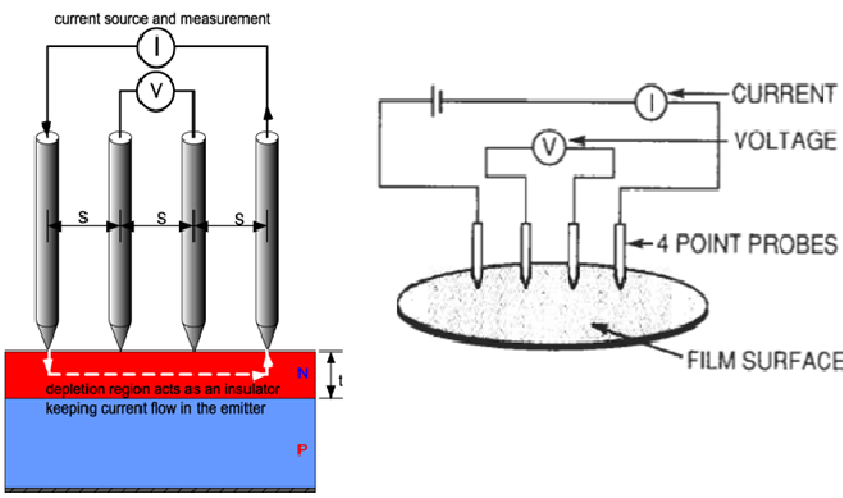

Fig. 5.5. *Four-point probe method for measuring the resistivity of the coatings*

The resistivity is then calculated from the following equation:

$$\rho = \frac{Vwh}{Il^1} \quad \text{(eq.5.2)}$$

Where ρ is the resistivity in Ωm, V voltage measured by voltmeter in volts, w- width of the sample bar measured in meters, h- height of the sample bar measured in meters, I- current the ammeter measures flowing through the sample in amperes, l^1- distance between the two points where the voltmeter wires make contact to the bar, measured in meters [14].

5.3.2. Two point technique I-V curves

The resistivity of a material can be obtained by measuring the resistance and physical dimensions of a bar of material. In this case, the material is cut into the shape of a rectangular bar of length *l*, height *h*, and widths w. Copper wires are attached to both ends of the bar. This

is called the two-point technique, since wires are attached to the material at two points. A voltage source applies a voltage V across the bar, causing a current I to flow through the bar. (Alternatively, a current source could force current through the sample bar, while a voltmeter in parallel with the current source measures the voltage induced across the sample bar). The amount of current I that flows through the bar is measured by the ammeter, which is connected in series with the bar and voltage source. The voltage drop across the ammeter should be negligible.

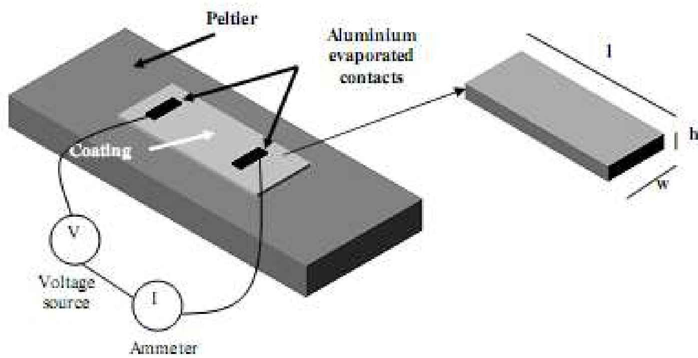

Fig. 5.6. *I-V technique for measuring the resistivity of the coatings*

The two-point resistivity of the material is then:

$$\rho \equiv \frac{Rwh}{l} \qquad \text{(eq.5.3)}$$

where ρ is the resistivity in Ωm, R is the measured resistance in Ω, and w, h, and l are the measured physical dimensions of the sample bar in meters.

In spite of the simplicity of this technique to measure electrical resistivity, there is usually some resistance between the contact wires and the material or inherent to the measuring equipment itself. This additional resistance is responsible for obtaining resistivity values higher than the real values of the tested material. Because of this problem, the experimental error is relatively smaller if it is used to measure the electrical resistivity of high electrical resistivity or insulating materials, where the electrical resistivity is several orders of magnitude higher than that one of the contacts [13-14].

5.4. Results and discussion

5.4.1. Electrical behaviour of the chromium oxynitride and aluminium oxynitride coatings

The electrical resistivity of the conducting films was measured using the four-pointed probe method (in linear geometry) [25]. For high resistivity films, aluminum contacts (1×6 mm^2) were vapor deposited on the top of the coatings and the electrical resistivity of the films was obtained from the I-V characteristic.

Following both the composition and structural characteristics evolutions of the systems, the electrical properties are showing, a wide range of different behaviors, as it can be observed by the evolution of the electrical resistivity at room temperature, as a function of the non-metallic/metallic concentration ratio (Fig. 5.7). The results correspond to the films from both systems AlN_xO_y (a) and CrN_xO_y (b).

The first conclusion to be drawn from this plot is that the evolution of resistivity is in good agreement with the different zones (regimes) analysed before for both systems , revealing that composition influences the film properties, as in fact it was already demonstrated for all films characteristics, such as the structural evolution.

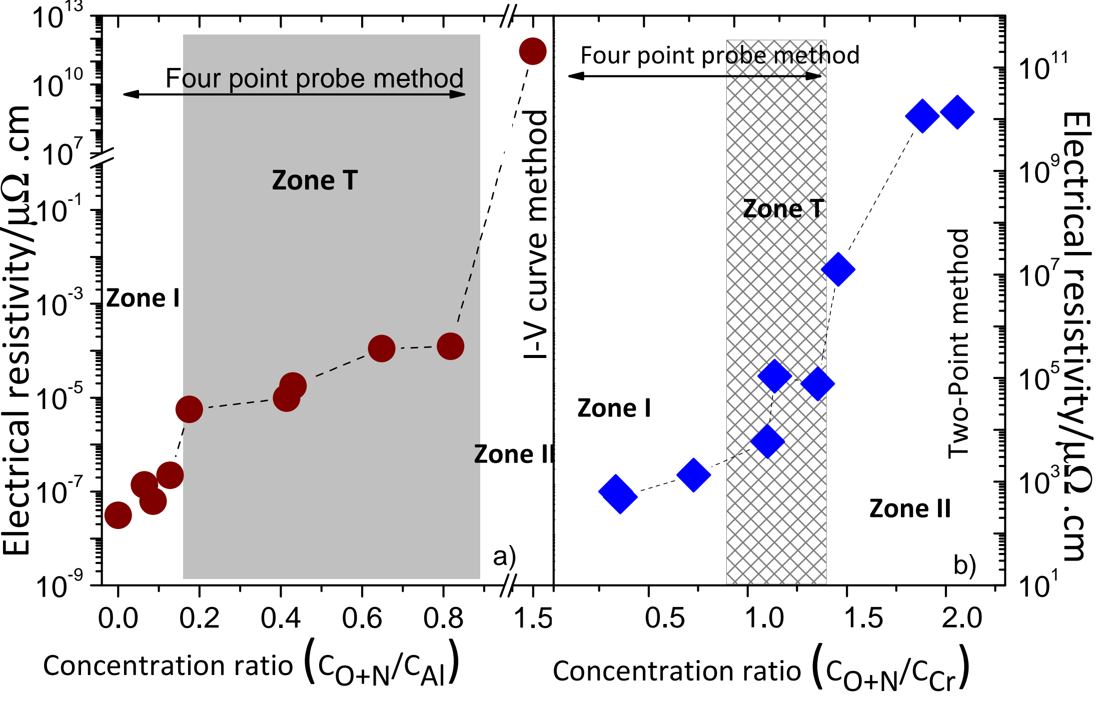

Fig. 5.7. *Electrical resistivity at room temperature of the films as a function of the:* ***a)*** *C_{O+N}/C_{Al} concentration ratio,* ***b)*** *C_{O+N}/C_{Cr} concentration ratio*

Regarding the AlN_xO_y system (Fig. 5.7a) the plot reveals for zone I films with low values of chemical ratio (C_{O+N}/C_{Al} <0.13) a very low electrical resistivity, close to the aluminium bulk resistivity (ρ = 2.67 μΩm). This zone consists in sub-stoichiometric thin films, with a fcc Al-type crystalline structure, were the electrical resistivity analyzed is between 3 and 23 μΩ cm corresponding to the metallic-like films.

Within the transition zone were the composition ratio is between 0.17< C_{O+N}/C_{Al} <0.65 that reveal the same sub-stoichiometric conditions and a crystallinity of the fcc structure. The incorporation of nitrogen and oxygen in the lattice leads to an increase in the electrical resistivity of the films to values between 5.6×10^2 and 1.1×10^4 μΩ cm. This behaviour can be explained by the decrease of the amount of the free electrons in the lattice, due to the reduction of the metallic content of the films.

Finally, the oxide films formed with a concentration ratio C_{O+N}/C_{Al} = C_O/C_{Al} =1.5 that revealed an over-stoichiometric condition with an amorphous Al_2O_3 structure that belongs to the compound-like zone respectively zone II.

The films from this zone exhibit an expected insulator behaviour with values of electrical resistivity between 10^{17} and 10^{18} μΩ cm. The electrical resistivity of these alumina films is in agreement with the values found in the literature for the alumina coatings [26-27].

Regarding the second system of thin films of CrN_xO_y, this are reviling for the samples from zone I, which presented a sub-stoichiometric condition and poorly crystallized XRD patterns of a fcc CrN-type structure, the resistivity analysis revealed relatively low values of resistivity, from 7.2×10^2 μΩ cm to around 1.5×10^3 μΩ cm, which are characteristic of metallic-like compounds, and relatively close to those of chromium nitride with varied stoichiometries, CrN_x ($1\times10^2 < \rho_{CrNx} < 15\times10^4$ μΩ cm) [28] but also higher the those of the Al-N-O system. R. Mientus et al. [29] reported the resistivity values of CrON films roughly in the vicinity of 1×10^4 μΩ cm for the lower nitride range - nitride-based coatings, the equivalent to zone I in this work. Anyway, their coatings were already in the stoichiometric condition and thus the range was not including all the set of sub-stoichiometric nitride compositions (O doped), which in the present case explains the variation from 1×10^2 to 1×10^4 μΩ cm.

For the samples prepared within the transition zone, where the composition analyses revealed a C_{O+N}/C_{Cr} ratio increase to an over-stochiometric condition, and the structural analysis showed a high crystalline fcc CrN-type phase, the resistivity analysis conducted to the development of an increase of the electrical resistivity of the films, with values ranging

between 7×10^3 and 1.4×10^5 μΩ cm. Again, there is a good agreement between these results and those obtained for both CrN_x and CrO_xN_y systems [28]. The first important note is the good agreement of the results obtained for the films within this transition zone and those obtained by R. Mientus et al. [29], which have quite similar values in their stoichiometric to close-stoiciometric-like CrO_xN_y films. Important also to note is the agreement of these resistivity values of the samples from zone T with those of bulk chromium nitride (ρ_{CrN} = 1×10^4 Ω cm) [29].

Finally, the oxide-like samples prepared within zone II presented an expected insulator-type behaviour, with high values of resistivity varying between $1,9\times10^7$ and 1.1×10^9 μΩ cm, consistent with Cr_2O_3 resistivity (ρ_{Cr2O3} >>10^8 μΩ cm), and far beyond the values obtained in zone T. This increase in the resistivity is also consistent with the increase in the stoichiometry of the samples, Fig. 3.9, especially that of C_O/C_{Cr}, which goes even beyond that of Cr_2O_3.
This work suggests that by simply changing the reactive gas flow it's possible to tune the electrical properties of CrNO and AlNO compounds in a wide range, from metallic like to semiconducting behaviour.

5.5. Conclusions

This chapter presents the evolution of the electrical resistivity measured at room temperature, according to the non-metallic/metallic concentration ratio which depends on both concentration and structure of the deposited films.
Regarding the first system of AlN_xO_y revelas for zone I samples that presents low values of concentration ratio and electrical resistivity, where electrical resistivity analyzed is between 3 and 23 cm μΩ cm. The second system with thin films of CrN_xO_y with samples deposited under sub-stoichiometric conditions showing relatively low resistivity of these films, with values from 7.2×10^2 μΩ cm to about 1.5×10^3 μΩ cm corresponding to a metallic films and yet higher than the ones from first system.

In the transition zone for the aluminium system where are sub-stoichiometric conditions and fcc crystal structure, the electrical resistivity of the samples have values between 5.6×10^2 and 1.1×10^4 μΩ cm. This behaviour can be explained by reducing the free electrons from the lattice, as a reduction of metal content within the layer. Instead the second

system presents the same conductor behaviour with higher values contained between 7×10^3 and 1.4×10^5 μΩ cm.

Finally, the formed oxide films presents a over-stochiometric condition with an amorphous structure of Al_2O_3 belonging to the compound zone, meaning zone II where the coatings present an insulating behaviour. The same insulator type is noted for zone II of the CrN_xO_y samples with values ranging between 1.9×10^7 and 1.1×10^9 μΩ cm which consistent with the higher oxygen content.

This work suggests that by simply changing the reactive gas flow is possible the adjustment of the electrical properties of AlNO and CrNO compounds in a wide range, from a metallic behaviour to a semiconductor one.

References

[1] L. Castaldi, D. Kurapov, A. Reiter, V. Shklover, and J. Patscheider, Journal of Applied Physics 109,053720 (2011).

[2] L. Castaldi, D. Kurapov, A. Reiter, V. Shklover , P. Schwaller, J. Patscheider, Surface & Coatings Technology 203 (2008) 545–549.

[3] R. Mientus, R. Grotschel, K. Ellmer, Surface & Coatings Technology 200 (2005) 341–345.

[4] K.R. Bray, R.L.C. Wu, S. Fries-Carr, J. Weimer, Thin Solid Films 518 (2009) 366–371.

[5] J. Wang, W.L. Wang, P.D. Ding, Y.X. Yang, L. Fang, J. Esteve, M.C. Polo, G. Sanchez, Diamond and Related Materials 8 (1999) 1342–1344.

[6] X. Qing, X. Hui, L.R. Arthur, Journal of Applied Physics 73 (1993) 8198–8200.

[7] L. Yate, J.C. Caicedo, A.H. Macias, F.J. Espinoza-Beltrán, G. Zambrano, J. Muñoz-Saldaña, P. Prieto, Surface and Coatings Technology 203 (2009) 1904–1907.

[8] L. Igor, B. David, Journal of the American Ceramic Society 81 (1998) 1995–2012.

[9] H. Kakati, A.R. Pal, H. Bailung, J. Chutia, Applied Surface Science 255 (2009) 7403–7407.

[10] B.G. Segda, M. Jacquet, J.P. Besse, Vacuum 62 (2001) 27–38.

[11] John. G. Webster, Electrical measurement, signal, processing and displays, CRC Press L.L.C, (2004).

[12] Emerson M. Girotto, Ivair A. Santos, Quim. Nova, Vol. 25, No. 4, (2002), 639-647.

[13] Pedro Carvalho, Development of new decorative coatings based on zirconium oxynitrides, Ph. D Thesis, Universidade do Minho (2008).

[14] Michael B. Heaney, Electrical Conductivity and Resistivity, CRC Press LLC, (2000).

[15] William D. Callister, Jr., Fundamentals of materials science and engineering, John Wiley & Sons, Inc., (2001).

[16] http://personal.cityu.edu.hk/~appkchu/AP4120/1.PDF

[17] Eugene A. Irene, Electronic Material Science, A John Wiley & Sons, Inc., Publication, (2005).

[18] http://www.mpia.de/homes/dullemon/lectures/obsastro/Chapter_CCDs.pdf

[19] http://physlab.lums.edu.pk/images/b/b9/Energybandgapv1.pdf

[20] C. A. C. Sequeira and D. M. F. Santos, Brazilian Journal of Physics 3B, (2007).

[21]-Ren Ye, The Laboratory Report of L226, (2006).

[22] http://en.wikipedia.org/wiki/Van_der_Pauw_method

[23] L. J. Van der Pauw, Philips Tech. Rev. 20 (1958) 220-224.

[24] A. Bartels, J. Appl. Phys. 15 (1995) 4271-4276.

[25] A.W. Robert, Review of Scientific Instruments 72 (2001) 3580.

[26] R. K. Bhan, A. Jain, D. Kumar, S. K. Mehta, Semiconductor Science and Technology 24 (2009) 9.

[27] J. Kolodzey, E. A. Chowdhury, T. N. Adam, Q. Guohua, I. Rau, J .O. Olowolafe, J. S. Suehle, C. Yuan, IEEE Transactions on Electron Devices 47 (2000) 121–128.

[28] E. Ando, S. Suzuki, Journal of Non-Crystalline Solids 218 (1997) 68-73.

[29] R. Mientus, R. Grötschel, K. Ellmer: Surf. Coat. Technol. 200 (2005) 341.

[30] G. Paglia, A.L. Rohl, C.E. Buckley, J.D. Gale, Phys. Rev. B 71 (2005) 224115.

[31] R.H. French, H.Mullejans, D.J. Jones, J.Am. Ceram. Soc. 81 (1998) 2549.

[32] A. Khanna, D.G. Bhat, Surf. Coating Technology. 201 (2006) 168.

[33] S. Cava, S.M. Tebcherani, S.A. Pianaro, C.A. Paskocimas, E. Longo, J.A. Varela, Mater. Chem. and Phys. 97 (2006) 102.

Chapter VI

Optical Characterization

6.1. Introduction

Optical measurements are attractive because they are almost always non-contacting with minimal sample preparation, a major advantage when contacts are detrimental. The instrumentation form any optical techniques are commercially available and are often automated. The measurements can have very high sensitivity [1]. In order to understand the optical behavior of films and film systems, one must become familiar with the optical constants of materials, their origins, magnitudes, and how they depend on the way film are processed. On this basis, optical properties are interpretable from what we know of the electronic structure and how it is affected by atomic structure, bonding, impurities, and defects [2].

From absorption spectrum as a function of photon energy, a number of processes can be contributed to absorption. At high energies photons are absorbed by the transitions of electrons from filled valence band states to empty conduction band states.

For energies just below the lowest forbidden energy gap, radiation is absorbed due to the formation of excitants, and electron transitions between band and impurity states. The transitions of free carriers within energy bands produce an absorption continuum which increases with decreasing photon energy. Also, the crystalline lattice itself can absorb radiation, with the energy being given off in optical phonons. Finally, at low energies, or long wavelengths, electronic transitions can be observed between impurities and their associated bands [3-4].

Optical measurements fall into three broad categories photometric measurements (amplitude of reflected or transmitted light is measured), interference measurements (phase of reflected or transmitted light is measured), and polarization measurements (ellipticity of reflected light is measured) [1]. The main optical techniques are summarized in Fig.6.1.

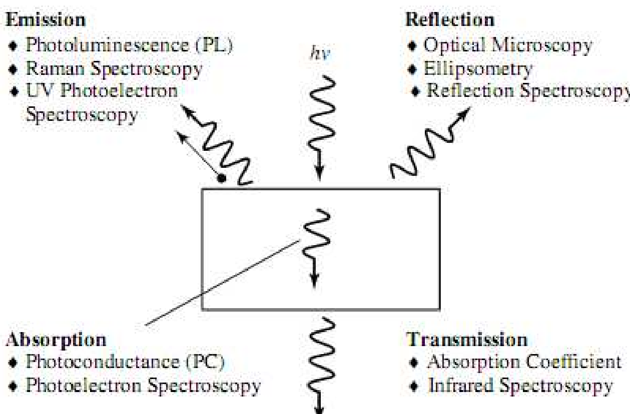

Fig.6.1. *Optical characterization techniques*

Investigations of optical properties of solids, including these of thin films, are aimed on: first, to obtain data for ascertaining their band structure; second, to determine such important parameters as refractivities and absorptivities necessary for designing devices and their elements. Thin films of transparent and light absorbing materials are widely used in manufacturing interferential and absorption filters, in production of multi-layer mirrors, polarizers, light detectors, in making antireflection coatings. In all enumerated cases one needs to have exact data upon optical constants, n and æ, of considered materials. For many years respective calculations were based on relationships that took into account repeated reflections and interference in a thin layer, and measured in experiment were intensities of light beams reflected and transmitted by the thin layer [5-6].

Optical properties of semiconductors typically consist of their refractive index *n* and extinction coefficient *k* or absorption coefficient α (or equivalently the real and imaginary parts of the relative permittivity) and their dispersion relations, that is their dependence on the wavelength, λ, of the electromagnetic radiation or photon energy *hv*, and the changes in the dispersion relations with temperature, pressure, alloying, impurities, etc [7].

The knowledge of accurate values of the wavelength dependent complex refractive index of thin solid films is very important, both from a fundamental and a technological viewpoint. It yields fundamental information on the optical energy gap (for semiconductors and insulators), defect levels, phonon and plasma frequencies, etc. Moreover, the refractive index is necessary for the design and modeling of optical components and optical coatings such as interference filters. If the model of an isotropic, homogeneous and plane-parallel thin film can be adopted, the real and imaginary parts of the refractive index at each wavelength completely determine

the optical properties of the film (in most instances, the film thickness can be determined at the same time) [8].

The important features in the α vs *hυ* behaviour as the photon energy increases can be classified in the following types of absorptions:

(a) Reststrahlen or lattice absorption in which the radiation is absorbed by vibrations of the crystal ions,

(b) free-carrier absorption due to the presence of free electrons and holes, an effect that decreases with increasing photon energy,

(c) an impurity absorption band (usually narrow) due the various dopants,

(d) exciton absorption peaks that are usually observed at low temperatures and are close to the fundamental absorption edge,

(e) band-to-band or fundamental absorption of photons, which excites an electron from the valence to the conduction band [7].

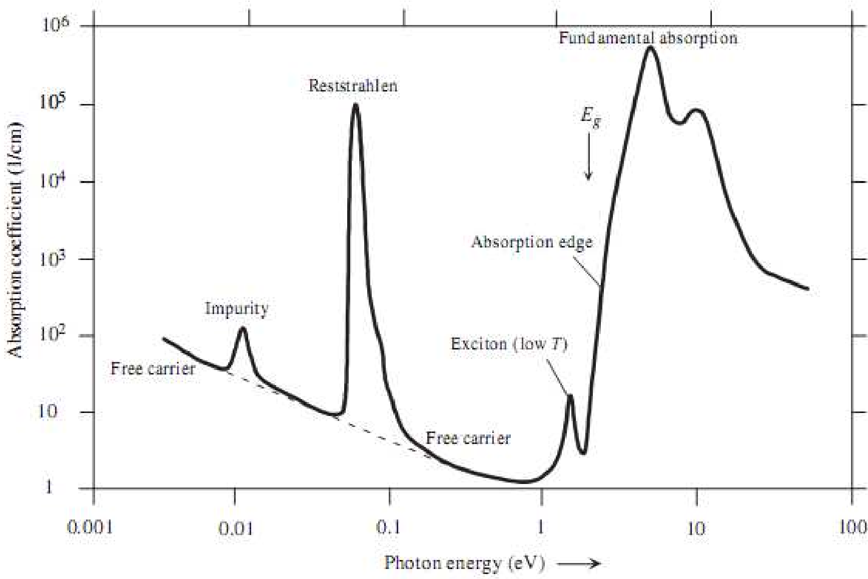

Fig. 6.2. *Absorption coefficient is plotted as a function of the photon energy in a typical semiconductor to illustrate various possible absorption processes*

6.1.1. Reststrahlen or lattice absorption

The Reststrahlen absorption takes place mostly in the infrared region giving no contribution to color. It originates from the response of optical phonons to the electromagnetic wave. For any two nearest-neighbor atoms having opposite charges, the optical phonon oscillations are then equipped with a set of dipoles. With a frequency comparable to that of

the lattice vibration, the incident electric field induces the vibration of two opposite charges in the converse direction. The vibration in the transverse optical mode generates the strongest absorption, called Reststrahlen absorption, and causes the reflection of the remaining light (mostly in the infrared region) called Reststrahlen reflection [9].

6.1.2. Free-carrier absorption

Striking a material having the partially filled valence band, the electromagnetic radiation excites the free carriers from the original ground states to unfilled higher energy states locating immediately above the Fermi energy level. Therefore, these carriers absorb light with a wide range of energy including the visible region. After being excited to the higher energy levels, no electron is infinitely stable in that state. Some may collide with the lattice vibrations and then dissipate their extra energy in form of heat. Some excited electrons return to lower energy states by dissipating their energy in the form of photons. The photons immediately leave the material surface as the observed reflected light [10].

The response of material is represented in terms of the refractive index, n, and the extinction coefficient, k. The refractive index is the ratio of light velocity in vacuum and in medium so it is not less than unity. The extinction coefficient of materials indicates the exponential damping of the light wave amplitude during the propagation in medium and it depends mainly on the conductivity of the materials. Both terms are described together as the complex refractive index, N. The response of free carriers to the electromagnetic radiation can be described by the Drude model [11-12]. This model explains the relation of the complex refractive index with the number of free electrons, N_e, an electronic charge, e, and an effective mass,

m_e as follows:

$$N = n + ik = 1 - \frac{4\pi N_e e^2}{m_e \omega^2} \quad \text{(eq.6.1)}$$

The frequency at zero complex refractive index is defined as the plasma frequency [9]:

$$\omega_e^2 = \left(\frac{4\pi N_e e^2}{m_e} \right) \quad \text{(eq.6.2)}$$

with m_e being the effective mass and N_e the number of conduction electrons per unit volume.

6.1.3. Band-to-band or fundamental absorption

Band-to-band absorption or fundamental absorption of radiation occurs due to the photo-excitation of an electron from the valence band to the conduction band. Thus, absorption of a photon creates an electron in the conduction band and a hole in the valence band and requires the energy and momentum conservation of the excited electron, hole, and photon. In crystalline solids, as the band structures depend on the electron wavevector k, there are two types of band-to-band absorptions corresponding to direct and indirect transitions. In contrast, in amorphous solids, where no long-range order exists only direct transitions are meaningful [7]. Both direct and indirect interband transitions must involve a third particle (e.g., a phonon) in addition to the electron and photon in order to account for the momentum transfer [3].

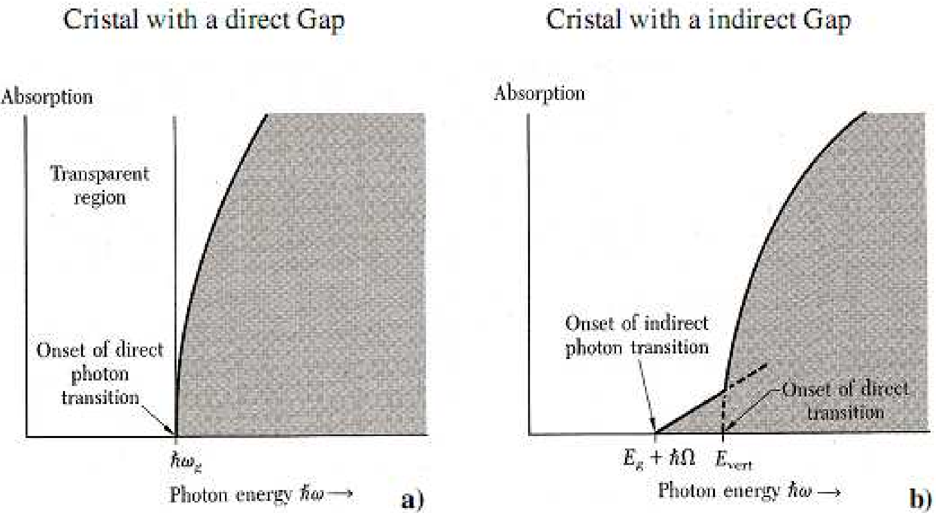

Fig. 6.3. *The absorption edge of;* ***a)*** *a direct semiconductor and* ***b)*** *indirect semiconductor*

From this picture it is clear that indirect transitions require a modification of the density of states since in the energy of the lattice vibrations (phonons) is involved in the transition process. The phonon is either created by the absorption process or, if the temperature is high enough, it is already thermally excited in the crystal.

With band gaps larger than the highest energy in the visible region (3.5 eV), the materials become transparent since there is no absorption of visible light. Materials with band gaps smaller than 1.7 eV (lower limit of visible region of the electromagnetic spectrum) are opaque and blackish due to the absorption of the whole spectrum of visible light wavelengths.

6.1.4. Impurity absorption

Impurity absorption can be registered as the peaks of absorption coefficient lying below the fundamental (band-to-band) and excitonic absorption. Mostly they can be related to the presence of ionized impurities or, simply, ions. The origin of these peaks lies in the electronic transitions either between electronic states of an ion and conduction/valence band or intra-ionic transitions (e.g., within d or f shells, or between s and d shells, etc.). In the first case the appearing features are intense and broad lines while in the latter case their appearance strongly depends on whether these transitions are allowed or not by the parity selection rules. For allowed transitions the appearing absorption peaks are quite intense and broad while the forbidden transitions produce weak and narrow peaks [7].

6.2. Characterization techniques

6.2.1. Spectrophotometry and colour space

In psychology, colour look is classified by means of visual sensation into three independent properties [13]: lightness, hue and saturation. Hue is what we usually mean when we ask “what colour is that?” It is s the classification in terms of red, blue, green, etc. Each hue corresponds to the relative spectral intensity that is very strong in particular ranges of wavelengths, saturation is related to chromaticity, saturation tells us how a colour looks under certain lighting conditions.

Spectroscopy is a technique that measures the interaction of molecules with electromagnetic radiation. Light in the near-ultraviolet (UV) and visible (vis) range of the electromagnetic spectrum has an energy of about 150–400 $kJmol^{-1}$.The energy of the light is used to promote electrons from the ground state to an excited state. A spectrum is obtained when the absorption of light is measured as a function of its frequency or wavelength. Molecules with electrons in delocalized aromatic systems often absorb light in the near-UV (150–400nm) or the visible (400–800nm) region.

Spectrophotometers are standard laboratory equipment. They usually contain two light sources: a deuterium lamp, which emits light in the UV region and a tungsten–halogen lamp for the visible region. After passing through a monochromator (or through optical filters) the light is focused into the cuvette and the amount of light that passes through the sample is detected by a photomultiplier or a photodiode. In double-beam instruments a cuvette with

buffer is placed in the reference beam, and its absorbance is subtracted from the absorbance measured for the sample.

Colourimetry is a form or better said one of the branches of spectroscopy, an analysis that measures how atoms or molecules respond when exposed to electromagnetic radiation of a certain wavelength and energy. The analysis made reveal an measurement of the absorption of visible light, the intensity of a solution’s colour (“colorimetry”) or the intensity of light reflected from the surface of materials (“reflectance colorimetry”) by using chemical tests or inexpensive apparatus. The intensity of the light exiting the sample (transmitted light) is measured on the other side of the sample. By comparing the incident intensity to the transmitted intensity, the absorbance can be determined for that wavelength of light [14-15].

The CIELAB metric transforms colors to a representation which is approximately perceptually uniform in the sense that Euclidean distances between different colors in this space correspond roughly to perceived color differences [16-17]

Colorimetry can describe the physiological colour perception by means of the L*a*b* coordinates in the CIELAB colour space.

The a* and b* represents the chromaticity coordinates and their magnitudes and signs are indicate hues and saturation [18]

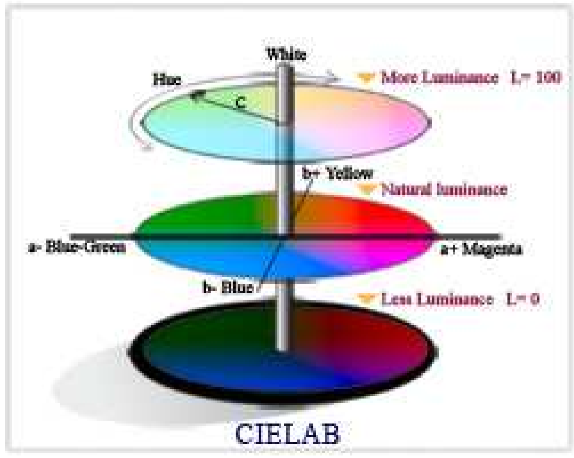

Fig. 6.4. *Schematic of the CIELAB colour space*

Regarding a* the positive values denote redness and the negative ones denote greenness, as for b* coordinate the positive value indicates yellowness and the negative blueness [19] with magnitudes that vary from zero at the center of the sphere to 100 at the surface.

As for the vertical axis this represents lightness, with scale of magnitudes between 100 that is attributed to a perfect white sample and zero to those of a perfect black (fig.6).
The equations are expressed as follows:

$$L^* = 116\sqrt[3]{\frac{Y_{10}}{Y_{10}^{0}}} - 16 \qquad \text{(eq.6.3)}$$

$$a^* = 500\left(\sqrt[3]{\frac{X_{10}}{X_{10}^{0}}} - \right) - \sqrt[3]{\frac{Y_{10}}{Y_{10}^{0}}} \qquad \text{(eq.6.4)}$$

$$b^* = 200\left(\sqrt[3]{\frac{Y_{10}}{Y_{10}^{0}}} - \right) - \sqrt[3]{\frac{Z_{10}}{Z_{10}^{0}}} \qquad \text{(eq.6.5)}$$

Where X_{10}, Y_{10} and Z_{10} are the XYZ Tristimulus values for a CIE 10º Supplementary Standard.

X_{10}^{0}, Y_{10}^{0}, Z_{10}^{0} are the XYZ tristimulus values for a perfect reflecting diffuser observed of the specimen. The value 10º reveals the filed of view of 88 mm at 500 mm view distance. Tristimulus values are the spectral sensitivity to red, green and blue light of the three different cones in the retina and are obatined from the integral equations that are presented in the visible region. The equations are presebted as follows:

$$X_{10} = K\int_{380}^{780} S(\lambda)x_{10}(\lambda)R(\lambda)d\lambda \qquad \text{(eq.6.6)}$$

$$Y_{10} = K\int_{380}^{780} S(\lambda)y_{10}(\lambda)R(\lambda)d\lambda \qquad \text{(eq.6.7)}$$

$$Z_{10} = K\int_{380}^{780} S(\lambda)z_{10}(\lambda)R(\lambda)dy \qquad \text{(eq.6.8)}$$

Where $K = \frac{100}{\int_{380}^{780} S(\lambda)y_{10}(\lambda)dy}$ (eq.6.9)

Tristimulus values are calculated from spectral reflectance factors, R(λ), covering the range 400-700 nm. In a 0-1 scale these factors express the reflectance at each wavelength as a decimal fraction of that reflected by a perfect reflecting diffuser identically illuminated. R(λ)

is multiplied by S(λ), the relative spectral power distribution of the illuminant, by each of the three colour matching functions $X_{10}(\lambda)$, $Y_{10}(\lambda)$, $Z_{10}(\lambda)$ and by the scaling factor κ [20].

The color measurement of the samples was made at room temperature by using a portable spectrophotometer Minolta CM-2600d. The measurement was performed at 8 degree viewing angle with a difuse illumination (D65 light source). The color quantization was reported using the L* a* b* color system [21].

The transmission and reflectivity was measured using a Shimadzu UV-3101 spectrophotometer.

6.2.2. Interaction between light and matter

When a light beam interacts at an interface between two semi-infinite media (air and material), several phenomena can occur. The wave generally changes direction (refraction), slows down, and it can be partially or completely absorbed (absorption), or transmitted (transmission), Fig.6.5.

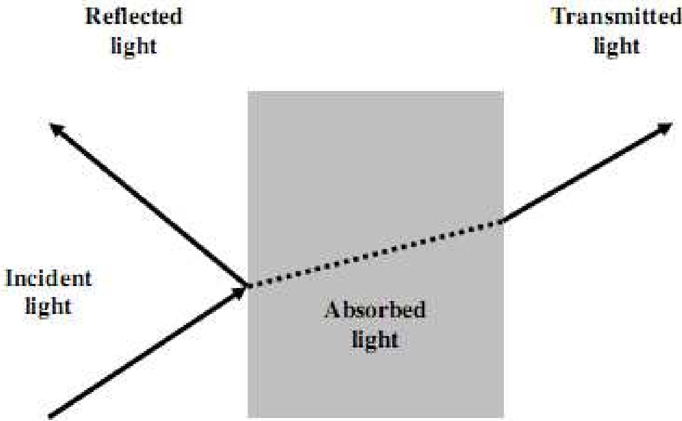

Fig. 6.5. *Phenomena occurring due to the interaction between light and matter*

When a material interacts with a such light beam, two of its most important characteristics may be unfolded: its complex index of refraction, N, which is a combination of a real number or refraction index n, and an imaginary number or extinction coefficient k. From k one can obtain the absorption coefficient, α, of the material as [18]:

$$\alpha = {4\pi k}/{\lambda} \quad \text{(eq.6.10)}$$

6.2.3. Transmission

Optical transmission or absorption measurements are used to determine optical absorption coefficients and certain impurities.

During transmission measurements light is incident on the sample and the transmitted light is measured as a function of wavelength as illustrated in Fig.6.6. The sample is characterized by reflection coefficient R, absorption coefficient α, complex refractive index ($n_1 - jk_1$), and thickness d. Light of intensity I_i is incident from the left.The absorption coefficient is related to the extinction coefficient k_1 by $\alpha = 4\pi k_1/\lambda$. The transmitted light I_t can be measured absolutely or the ratio of transmitted to incident light can be formed [1].

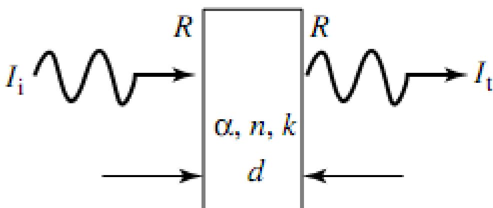

Fig. 6.6. *Schematic transmittance measurement*

The transmittance T of a sample with identical front and back reflection coefficient and light incident normal to the sample surface is:

$$T = \frac{(1-R)^2 e^{-\alpha d}}{1+R^2 e^{-\alpha d} - 2Re^{-\alpha d}\cos(\phi)} \qquad \text{(eq.6.11)}$$

where $\phi = 4\pi n_1 d/\lambda$ and the reflectance R is given by:

$$R = \frac{(n_0-n_1)^2+k_1^2}{(n_0+n_1)^2+k_1^2} \qquad \text{(eq.6.12)}$$

The semiconductor band gap can be determined by measuring the absorption coefficient as a function of the photon energy [1]. Light,with energy higher than the band gap, is absorbed. However, absorption is low to moderate for $h\nu$ near E_G. For indirect band-gap semiconductors, $\alpha^{1/2}$ is plotted against $h\nu$, the extrapolated intercept on the $h\nu$ axis yields the semiconductor band gap. Such a plot is sometimes referred to as a Tauc plot. For direct band-gap semiconductors like GaAs, for example, α^2 is plotted against $h\nu$ and the band gap is again determined from the extrapolated intercept [22].

6.2.4. Reflection

Reflection or reflectivity measurements are commonly made to determine layer thicknesses, both for insulating layers on semiconducting substrates and for epitaxial semiconductor films.

Figure 6.7. shows a reflection of linearly polarized light at the interface between two media.

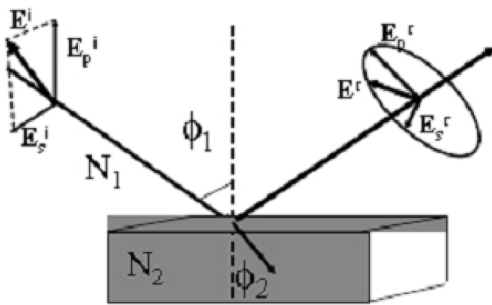

Fig. 6.7. *Linearly polarized light after reflection at the interface between two media changes to elliptically polarized light*

The reflectance for the structure, consisting of an absorbing layer of thickness d_1 on a nonabsorbing substrate, is given by:

$$R = \frac{r_1^2 e^{\alpha d_1} + r_2^2 e^{-\alpha d_1} + 2r_1 r_2 \cos(\varphi_1)}{e^{\alpha d_1} + r_1^2 r_2^2 e^{-\alpha d_1} + 2r_1 r_2 \cos(\varphi_1)} \qquad \text{(eq.6.13)}$$

Where

$$r_1 = \frac{n_0 - n_1}{n_0 + n_1};\ r_2 = \frac{n_1 - n_2}{n_1 + n_2};\ \varphi_1 = \frac{4\pi n_1 d_1 \cos(\phi^`)}{\lambda};\ \phi^` = \arcsin\left[\frac{n_0 \sin(\phi)}{n_1}\right] \qquad \text{(eq.6.14)}$$

Reflection is often dominated by surface roughness, which makes the material diffusive or specular. The cause for specular reflection is a difference in refractive indices. The fraction of reflected light, R, is determined by Fresnel's formula:

$$R = \frac{(n_2 - n_1)^2}{(n_2 + n_1)^2} \qquad \text{(eq.6.15)}$$

Instead of illuminating the sample with monochromatic light and varying the wavelength, it is possible to shine white light, containing many wavelengths, onto the sample

and analyze the reflected light by passing it through a spectrometer. Small areas can be characterized by shining the light through a microscope. Once the various wavelengths have been dispersed by the spectrometer, they can be detected by a photodiode array with the various wavelengths falling on different diodes in the array, for automatic data acquisition [7]. Reflectance measurements are also used to determine the thickness of epitaxial semiconductor layers, but it only works if there is a substantial doping density change at the epitaxial substrate interface, because there must be a measurable index of refraction change at that interface.

6.3. Results and discussion

6.3.1. Optical behaviour of chromium and aluminium oxynitride coatings

Regarding the optical behaviour of the chromium and aluminium oxynitride this is represented in the colour coordinates as a function of the reactive partial pressure N_2+O_2 represented by the CIELAB 1976 colour space in fig. 6.8 and 6.9.

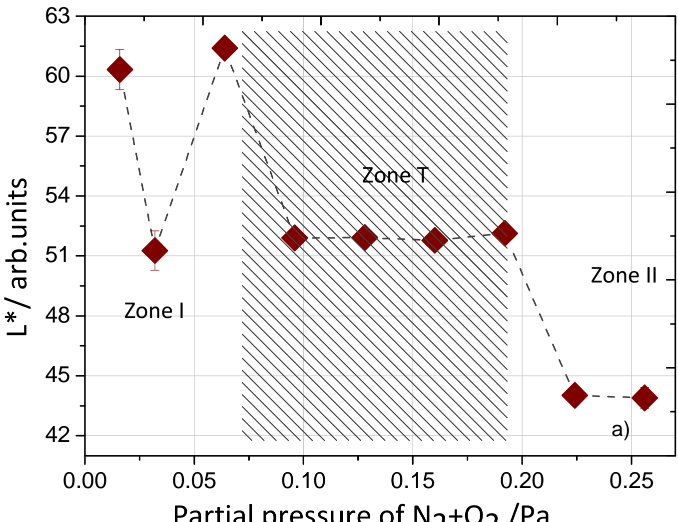

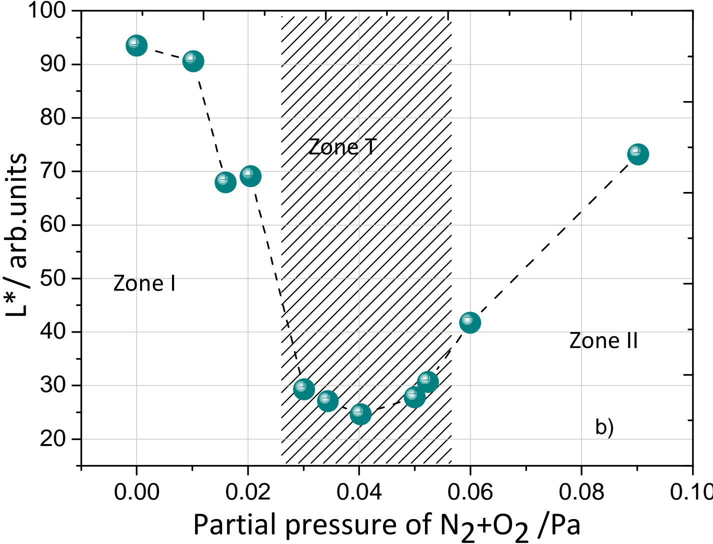

Fig. 6.8. *L* coordinate of the CIELAB 1976 colour space for a) CrN_xO_y and b) AlN_xO_y, under the standard CIE illuminant D65, for films prepared with different reactive gas flows from series 1. The error bar was determinate by maximum deviation to the average value*

Regarding the values that defined the brightness of the samples of the CrN_xO_y represented in fig. 6.8a) were the same three zones of the samples mentioned in the previous chapters are still present the same as in the case of AlN_xO_y (fig 6.8b). Discussing the samples of the chromium oxynitride the plot revealed that zone I presents the higher values of brightness L* that is characteristic of the samples prepared with low reactive gas partial pressure N_2+O_2 that have a characteristic metallic colour. This high values of L* is applied even for zone I of the aluminium oxynitride coatings that compose this zone, indicate the same metallic colour that decrease with the increase of the reactive gas.

The samples that indicates the transition zone for the chromium presents steady values of brightness to a value close to 51 that reveals the decrease of the metallic content in the samples with a dark grey colour. The brightness values regarding the aluminium oxynitride coatings that forms zone T, are almost stable with a dark grey opaque-like surface tones.

As for the second zone (zone II) the distinction between the two systems is quite clear and can be very well seen in fig 6.8 a) and b). This zone reveal samples prepared with high reactive gas partial pressure presenting lower values of brightness with a dark grey colour consistent with their semi-transparency for the case of chromium oxynitride (Fig. 6.8a). The samples of aluminium oxynitride that forms zone II reveal an increase of L* compared with the one from the transition zone that is explained by the composition of the films that reveal a

higher incorporation of the oxygen that is in accordance with the interference-like colorations, consistent with its semi-transparency (Fig 6.8b).

For a better understanding of this differences between the set of samples that compose this three different zone for chromium and also for aluminium oxynitride. The decrease of the brightness is given by the decrease of the amount of the chromium or aluminium content that arrives to the substrates and of course of the reactive gas partial pressure used for the coating deposition.

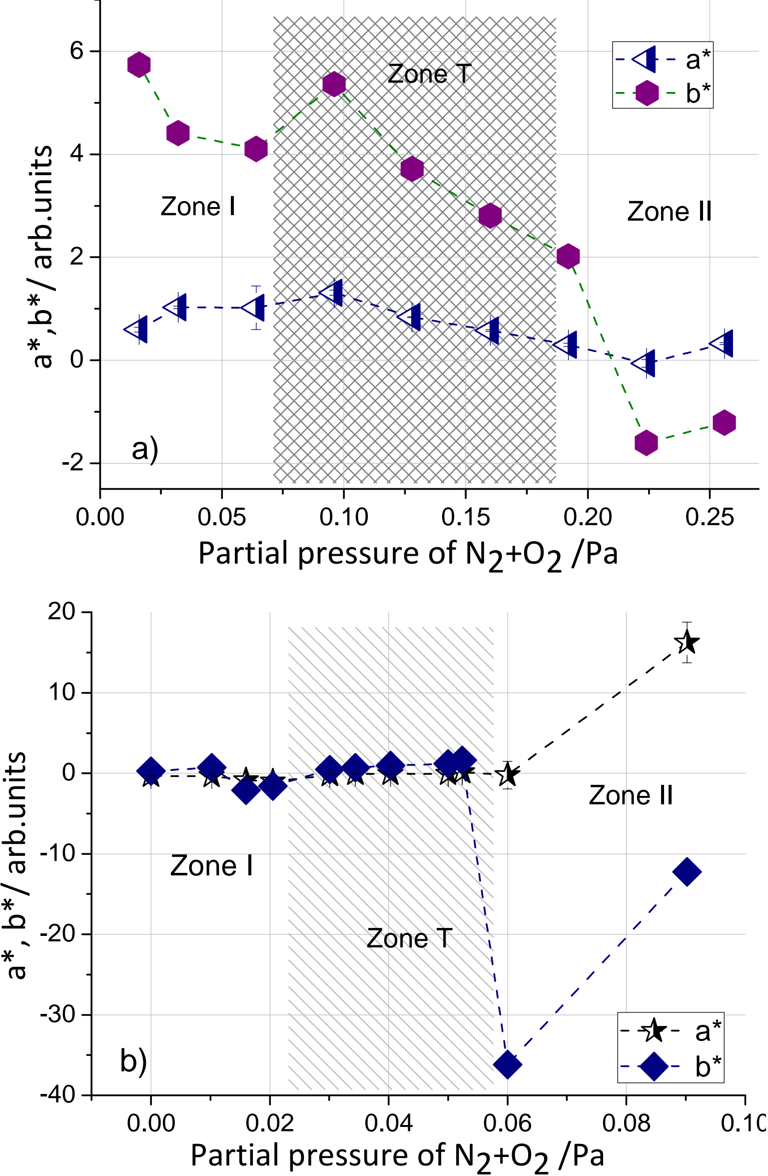

Fig. 6.9. *Chromaticity coordinates (a* and b*) of the CIELAB 1976 colour space for a) CrN_xO_y and b) AlN_xO_y, under the standard CIE illuminant D65, for films prepared with different reactive gas flows. The error bar was determinate by maximum deviation to the average value*

The chromaticity coordinates of the chromium oxynitride (Fig. 6.9a) presents for zone I when the partial pressure is low between 0.016 to 0.064 Pa, the values of a* shown no significant change but the positive b* value that represents the yellowness shows a significant decreases that continues also for the samples that compose the transition zone. Regarding the zone II where the partial pressure has the higher values ~ 0.25 Pa were the, a* value keeps the same tendency like in the other zone but b* values are decreasing sharply until a negative value of b* (blueness) is touched.

Taking in consideration the second case, namely the aluminium oxynitride it can be seen a quite clear difference between these two systems (Fig. 6.9b). The first zone of aluminium that is compose by the low values of partial pressure N_2+O_2 have an almost constant values of a* and b* at the limit between the negative and positive values of the chromaticity coordinates. The difference can been seen in zone II were chromaticity coordinates presents a significant change compared with zone I and T. In this zone the positive a* values (redness) shows a significant increase and a sharp decrease of the negative b* values (blueness) describing very well the interference colorations of the samples from this zone given by the changes in the composition presenting in the other chapters.

6.3.2. Reflectance of the coatings

Fig. 6.10 presents the reflectance spectrum in the visible range of the chromium oxynitride from the all three zones that were divided even from the first chapters. From the analysis of the reflectance spectra is visible a high values of reflectance in zone I that is to be expected because of the metallic nature of the films.

As the reactive mixture gas is increasing and the chromium concentration is decreasing the reflectance decreases slightly in the transition zone were the samples present a dark grey colour.

Taking in consideration the metallic like behaviour of the reflectance spectrum of the sample in the first zones, zone II compose from over-stoichiometric films reveal a drop of reflectance that is explained by their semi-transparency and by the phase transition (from CrN to Cr_2O_3) [23] that is described by the chemical concentration.

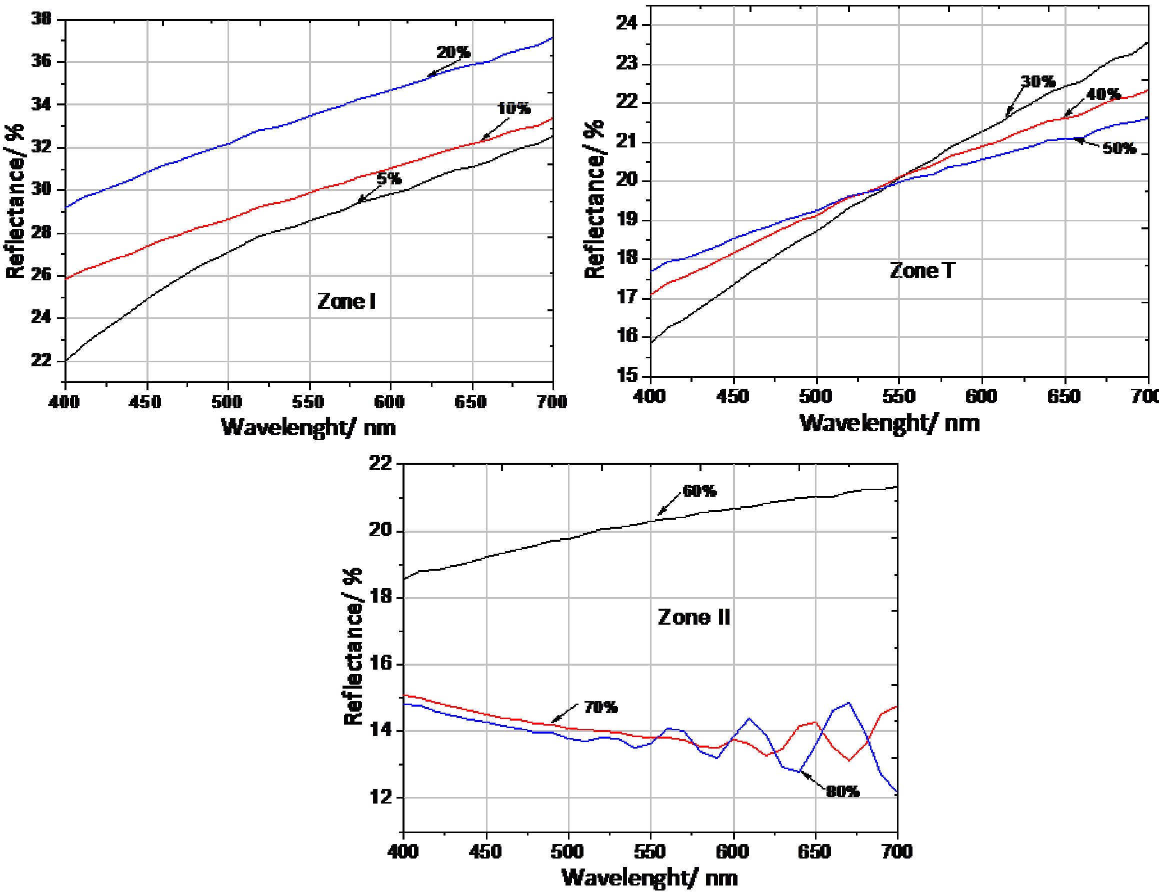

Fig. 6.10. *Reflectance spectrum in the visible range of the CrN_xO_y samples from the all three zones*

Taking under analysis the behaviour of the reflectance spectra of the AlN_xO_y samples we discover that zone I presents the metallic like behaviour of the samples with the a much higher value of reflectance then in the case of the chromium toching a value close of 90% for the sample without reactive gas (pure Al) as it can bee seen in Fig. 6.11.

In the transition zone the reflectance drops to a residual value of 4% given by the decrease of the metallic content and the dark opaque color of the samples.

In zone II given by the semi-transparency of the sample and the insulator behaviour, a increase of the reflectance spectra to a value of ~65% that may be explained by the increase of the oxygen content given by the formation of the alumina (Al_2O_3).

An application of AlON films can be as an optical coatings that`s way the presence of the transparency is an important factor [24].

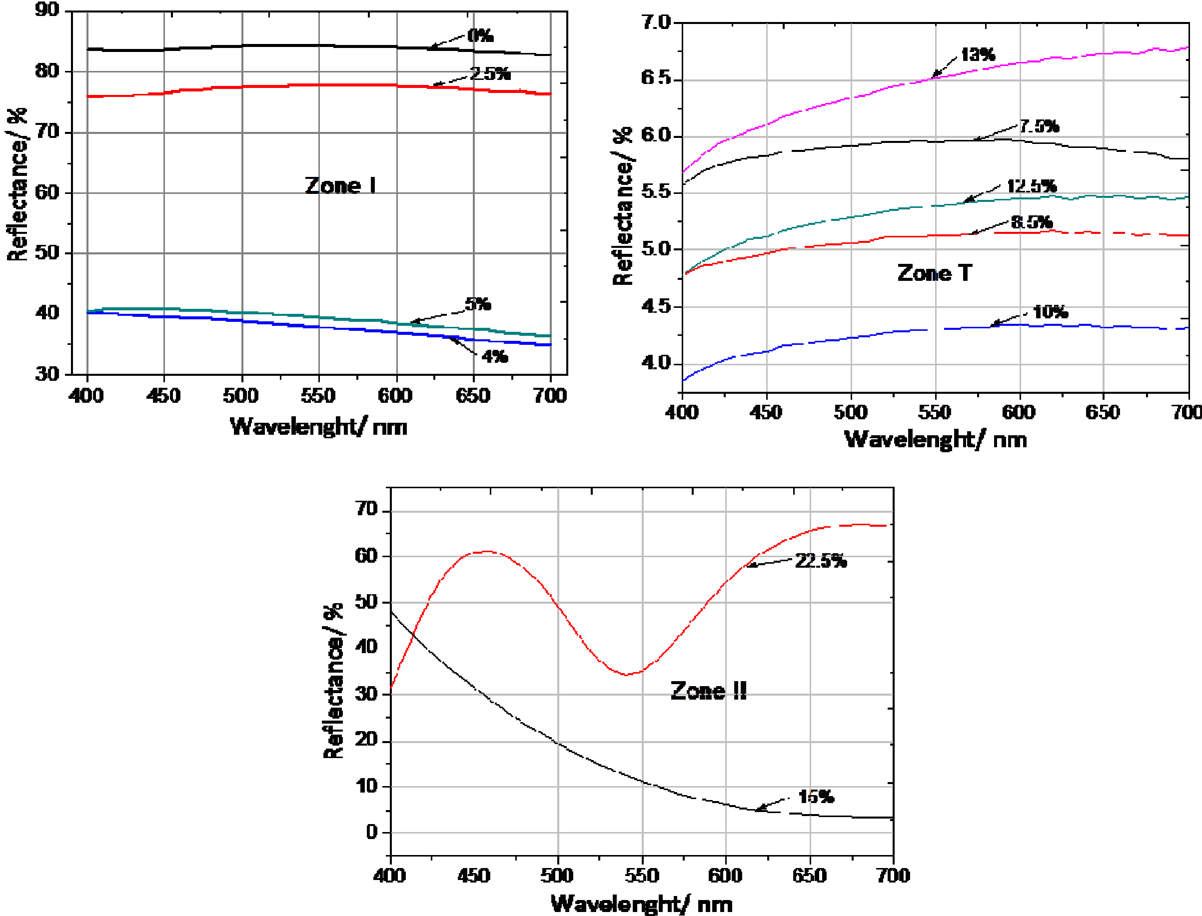

Fig. 6.11. *Reflectance spectrum in the visible range of the* AlN_xO_y *samples from the all three zones*

6.3.3. Optical transmittance of the coatings

Figure 6.12 shows the transmittance spectrums for sample that compose zone II of the two sets of coatings of chromium and aluminium oxynitride. The measurements of the optical transmittance were performed with a wavelength that starts from 200 until 2500 nm.

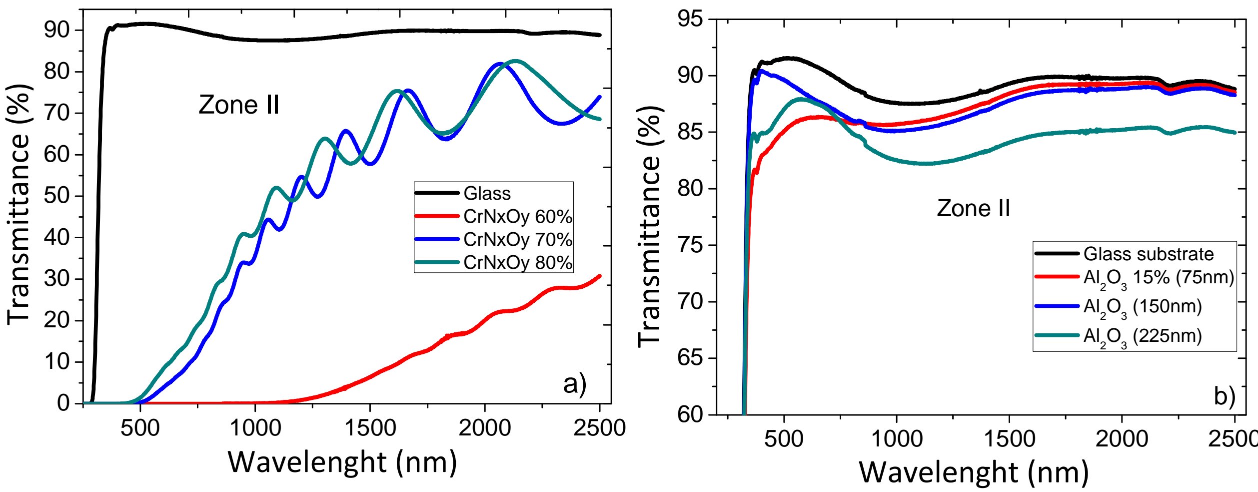

Fig. 6.12. *Transmittance spectrums for the samples from zone II* ***a)*** *samples of chromium oxynitride,* ***b)*** *samples of aluminium oxynitride*

The data of the optical transmittance reveal that the samples measured from zone II of the two systems are optically transparent in the visible and near-infrared regions.

The analysis of transmittance spectra of the chromium oxynitride reveal that in zone I the sample deposited with 30 sccm presents a transmittance of ~ 30% in the near-infrared region. With the increase of the reactive mixture gas the optical transmittance increases even in the visible range and to a value close to 80% in the near-infrared region. As for the aluminium oxynitride samples the transmittance data reveal the optically transparency in the visible and near-infrared region with values close to 90% as can be observed in fig 6.12 b).

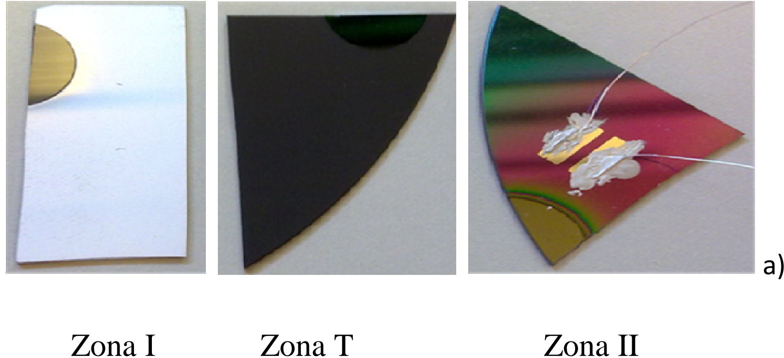

Zona I Zona T Zona II

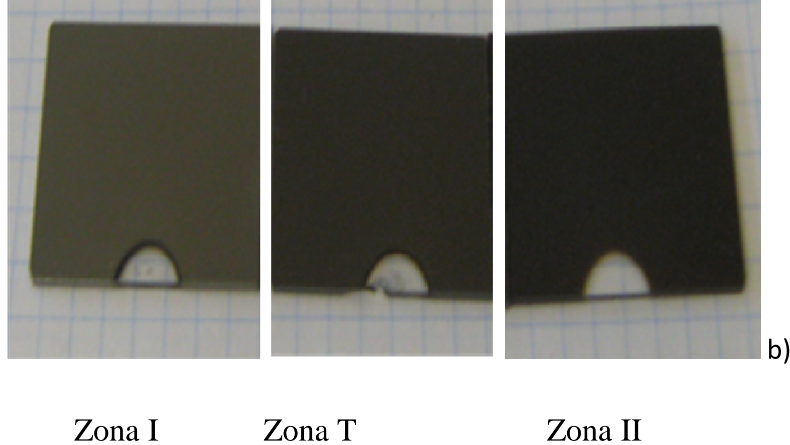

Fig. 6.13. *Pictures of the substrates after the deposition of the thin films from the all three zones that are dived:* ***a)*** *AlN_xO_y type and* ***b)*** *CrN_xO_y type*

Figure 6.13 presents pictures from the representative samples divided into the three zones in order to see their color due to reactive gas flow that was introduced during the deposition process.

6.4. Conclusions

This chapter presented the optical properties of thin films determined namely color, reflectivity and optical transmission that these films have developed after the deposition. These were determined by using a portable spectrophotometer Minolta CM-2600d trade (with which was measured the color of the samples in color space CIELAB 1976 and reflectance) and with the help of the Shimadzu UV-3101 PC spectrophotometer was determined transmission of the films.

In the case of brightness L* of the two different systems of oxynitrides, it shows a clear difference between the chromium and aluminum oxynitride. Aluminum oxynitride reveals for zone I a metallic zone area with higher values compared with samples from zone I of the chromium oxynitride. Chromatic coordinates a* and b* of the first zone presents the same difference between the two systems, the samples of AlN_xO_y shows a constant value of the two coordinates a* and b*, while the CrN_xO_y samples reveals a decrease of the positive value b* and an approximately constant value of a*. This difference persists in the case of reflectance, with values up to 85% for the AlN_xO_y and values up to 40% for the CrN_xO_y samples.

Transition zone of the two systems reveals a degree of brightness L* of the chromium oxynitride greater than that of aluminum. The AlN_xO_y chromatic coordinates have revealed a stability in zone I, as for the CrN_xO_y they show a value almost stable for a* and an continues to decrease of b* bringing darker tones of these samples revealed by the reflectance measured for this samples with values up to ~24%. Samples of AlN_xO_y have a decrease of the reflection up to 7% which means that the colours of the films have a darker tone going until black with an opaque surface.

Zone II is represented by a significant reduction in the brightness in the samples of chromium oxynitride while the aluminium system shows an increase of it. This difference is supported by the chromatic coordinates that continues to decrease for CrNO while in the aluminum system both a* and b* reveal a significant increase. The amount of the reflectance decreases in the chromium system and for aluminum, she has a significant growth that is consistent with semitransparency of these samples.

In the second zone, the optical analysis carried out revealed high values of transmittance in near infrared domain g being optically transparent in the visible one, thing that is applied to both systems (aluminum and chromium).

References

[1] D. Schroder, Semiconductor Material and Device Characterization, Published by John Wiley & Sons, Inc, (2006).

[2] M. Ohring, The Material Science of Thin Films, Academic Press, (1992).

[3] Donald M. Mattox, Handbook of physical vapor deposition (PVD) processing, Noyes publications,(1998).

[4] Rnjdar Rauff M., Ali Bakr Ali, Optical properties of thin film, University of Sulaimani (2005).

[5] S.A. Kovalenko, Semiconductor Physics, Quantum Electronics & Optoelectronics. 1999. V. 2, N 3. P. 13-20.

[6] W. Kruhler, Appl. Phys. A, 53, N 1, p.54, (1991).

[7] J. Singh, Optical Properties of Condensed Matter and Applications, John Wiley & Sons Ltd, England, (2006).

[8] D. Poelman, P. Frederic Smet, Appl. Phys. 36 (2003) 1850–1857.

[9] S. Niyomsoan, W. Grant, D.L. Olson, B. Mishra, Thin Solid Films 415 (2002) 187–194.

[10] Dick Bedeaux, Jan Vlieger, Optical properties of surfaces second edition, (2004).

[11] A. Schlegel, P. Wachter, J.J. Nickl, H. Lingg, Solid State Phys. (1977) 4889.

[12] F. Seitz, D. Turnbull, Solid State Phys Adv. Res. Appl. 6 (1958) 313.

[13] F.W. Billmeyer, M. Saltzman, Principles of Color Technology, Interscience Publishers, New York, NY, 1966.

[14] http://www.chem.ubc.ca/courseware/154/tutorials/exp3A/colorimetry/

[15] Aleksandra R. Zarubica, Milena N. Miljković, Milovan M. Purenović, Vesna B.Tomić, Physics, Chemistry and Technology Vol. 3, No 2, 2005, pp. 205 – 216.

[16] Xuemei Zhang, D. Amnon Silverstein, Joyce E. Farrell , Brian A. Wandell, COMPCON 97 Proceedings of the 42nd IEEE International Computer Conference (1997).

[17] S. Camelio, T. Girardeau, L. Pichon, A. Straboni, C. Fayoux, Ph. Gu´erin, J. Opt. A: Pure Appl. Opt. 2 (2000) 442–448.

[18] Pedro Carvalho, Development of new decorative coatings based on zirconium oxynitrides, Thesis, (2008).

[19] H.M. Beniaa, M. Guemmaza, G. Schmerber, A. Mosser, J.C. Parlebas, Applied Surface Science 211 (2003) 146–155.

[20] Aleksandra R. Zarubica, Milena N. Miljković, Milovan M. Purenović, Vesna B. Tomić, Physics, Chemistry and Technology Vol. 3, Nr 2, (2005) pp. 205 – 216.

[21] S. Niyomsoan, W. Grant, D.L. Olson, B. Mishra, Thin Solid Films 415 (2002) 187–194.
[22] W.D. Callister, Jr., Fundamentals of Materials Science and Engineering (fifth edition), (2001).
[23] R.Mientus, R.Grotschel, K.Ellmer, Surface & Coatings Technology 200 (2005) 341–345.
[24] Wende Xiao, X. Jiang, Journal of Crystal Growth 264 (2004) 165–171.